

**University of Alberta**

**Focused Ion Beam Milled Magnetic Cantilevers**

by

**Alastair Edward Fraser**

A thesis submitted to the Faculty of Graduate Studies and Research  
in partial fulfillment of the requirements for the degree of

**Master of Science**

in

**Physics**

Department of Physics

©Alastair E. Fraser  
Spring 2010  
Edmonton, Alberta

Permission is hereby granted to the University of Alberta Libraries to reproduce single copies of this thesis and to lend or sell such copies for private, scholarly or scientific research purposes only. Where the thesis is converted to, or otherwise made available in digital form, the University of Alberta will advise potential users of the thesis of these terms.

The author reserves all other publication and other rights in association with the copyright in the thesis and, except as herein before provided, neither the thesis nor any substantial portion thereof may be printed or otherwise reproduced in any material form whatsoever without the author's prior written permission.

## **Examining Committee**

Dr. Mark Freeman, Physics

Dr. Al Meldrum, Physics

Dr. Frank Hegmann, Physics

Dr. James McMullin, Electrical and Computer Engineering

*To*

*my mother Noni, and my father Stirling.*

## **Abstract**

The procedure for milling micrometre scale cantilevers of lutetium iron garnet using a focused ion beam microscope was developed. The infrastructure to study these cantilevers using rotational hysteresis loops and ferromagnetic resonance experiments was set up. The cantilevers were shown to remain magnetic after milling, and the origin of their hysteresis loops investigated with a variant of the Stoner-Wohlfarth model. Ferromagnetic resonance in the cantilevers was demonstrated as the first step towards studying magnetomechanical coupling.

## Acknowledgements

Many people have helped me throughout this work. Space and time do not permit me to thank them all, but in particular I wish to acknowledge the following.

My co-workers in our laboratory have been a constant help, and I have greatly enjoyed working with them. Thank you Robert Bryce, Jacob Burgess, Shawn Compton, John Davis, Dave Fortin, Joe Losby, and Steven Olson. Lynn Chandler in particular has been a great help and a pleasure to work with.

The electronics shop staff (Bill Burris, Shengli Liu, John Schaapman, and Len Wampler) were a constant source of friendly and useful advice. Tony Walford and Don Mullin gave me extensive assistance with setting up my experiments, while Daniel Salamon at NINT, as well as the staff at the Nanofab, provided me with excellent support.

I gratefully acknowledge Doug Vick, for in addition to all the FIB work, Doug helped me with many decisions regarding my devices and often stayed late to assist me.

Geoff Steeves at UVic gave me my first lab experience, my first job in physics, and much support and guidance over the years.

I owe a particular thanks to my parents, Noni and Stirling, for being such excellent mentors and encouraging me in all I do.

Finally, my heartfelt thanks to Mark Freeman. I have learned much from him; lessons that will be of great use to me both in and outside of physics. I am grateful to Mark for the opportunity to study under him. It would have been hard to find a better supervisor.

# Table of Contents

<b>1</b>	<b>Introduction</b>	<b>1</b>
1.1	Motivation for Studying Magnetomechanical Coupling . . . . .	1
1.2	Theoretical Background . . . . .	3
1.2.1	A Cantilever's Vibration . . . . .	3
1.2.2	Classical Model of Magnetism . . . . .	5
1.2.3	The Faraday Effect . . . . .	7
1.3	Hysteresis Loops . . . . .	8
1.3.1	Rotational Hysteresis Loops . . . . .	10
1.4	Ferromagnetic Resonance . . . . .	15
<b>2</b>	<b>Making NEMS Cantilevers</b>	<b>18</b>
2.1	Making a Cantilever Overview . . . . .	18
2.2	Lutetium Iron Garnet Properties . . . . .	20
2.3	Ion Slicing . . . . .	22
2.4	Focused Ion Beam milled Cantilevers . . . . .	25
2.4.1	Focused Ion Beam Milling Overview . . . . .	25
2.4.2	Sample Preparation . . . . .	26
2.4.3	Focused Ion Beam Milling Complications . . . . .	31
2.5	Producing a Cantilever: Procedure . . . . .	40
2.5.1	Milling a Cantilever . . . . .	42

## TABLE OF CONTENTS

2.5.2	Cantilever Thickness Measurements . . . . .	43
2.5.3	Milling a Doubly-Clamped Beam or Paddle Structure . . . . .	44
<b>3</b>	<b>Experimental Setups</b>	<b>48</b>
3.1	Hysteresis Loop Measurements . . . . .	48
3.1.1	Optical setup . . . . .	49
3.1.2	Faraday Rotation Calibration . . . . .	53
3.1.3	Hall probe . . . . .	54
3.1.4	Focusing Procedure . . . . .	54
3.1.5	Magnet And Rail System . . . . .	58
3.2	Ferromagnetic Resonance Measurements . . . . .	61
3.2.1	Pump and Probe Technique . . . . .	61
3.2.2	Dither Field . . . . .	61
3.2.3	Pulsed Laser . . . . .	63
3.2.4	RF Switch and Lock-in Technique . . . . .	63
3.2.5	Focusing Differences Through the Dither Coil . . . . .	66
<b>4</b>	<b>Modeling</b>	<b>70</b>
4.1	The Stoner-Wohlfarth Model . . . . .	70
4.2	Energy Contributions to Magnetization Direction . . . . .	71
4.3	Model Implementation . . . . .	73
4.3.1	Origin of Hysteresis . . . . .	75
4.3.2	Model in Three Dimensions . . . . .	80
4.3.3	Cubic Anisotropy . . . . .	87
<b>5</b>	<b>Hysteresis Loops</b>	<b>94</b>
5.1	Hysteresis Loop Summary . . . . .	94
5.2	Lutetium Iron Garnet Hysteresis Loops . . . . .	95
5.2.1	Differences from Sample Mounting Orientations . . . . .	95

*TABLE OF CONTENTS*

5.2.2	Hall Probe Position Effect . . . . .	99
5.2.3	Differences Due to Laser Power . . . . .	100
5.3	Evidence of Ion Damage . . . . .	106
<b>6</b>	<b>Ferromagnetic Resonance</b>	<b>112</b>
6.1	Ferromagnetic Resonance Overview . . . . .	112
6.2	Dither Field Generation . . . . .	113
6.2.1	In-plane and out-of-plane field FMR measurements . . . . .	116
6.2.2	Dither Coil Construction . . . . .	116
6.3	Ferromagnetic Resonance in bulk LuIG . . . . .	118
6.4	Fast Fourier Transforms of FMR . . . . .	119
6.5	FMR of 45° Mounted LuIG . . . . .	123
6.6	FMR in LuIG Cantilevers . . . . .	124
<b>7</b>	<b>Conclusion</b>	<b>129</b>
	<b>Bibliography</b>	<b>133</b>
<b>A</b>	<b>Appendix</b>	<b>137</b>
A.1	SEM Image Length Projections . . . . .	137
A.2	DAQ Connection Table . . . . .	141

# List of Figures

1.1	Vibration modes of a doubly clamped beam . . . . .	4
1.2	Typical hysteresis loop . . . . .	9
1.3	Linear vs. rotational hysteresis schematic . . . . .	11
1.4	Magnetization rotation schematic for high and low fields . . . . .	12
1.5	Typical rotational hysteresis loop . . . . .	13
1.6	Sample rotation schematic . . . . .	14
1.7	Projection effect of magnetization on laser beam direction . . . . .	15
1.8	Torque on a magnetic dipole . . . . .	17
1.9	Ideal ferromagnetic resonance ring down . . . . .	17
2.1	SEM image of etched implanted layer for ion slicing . . . . .	23
2.2	Schematic of bonding ion implanted LuIG to substrate . . . . .	24
2.3	Schematic of polishing sample . . . . .	27
2.4	Al polishing block and tripod polishing setup . . . . .	29
2.5	Back tilt effect in milling . . . . .	32
2.6	FIB chamber with sample stage, FIB column, and SEM column . . . . .	33
2.7	SEM images of charging problems during milling . . . . .	36
2.8	SEM image of redeposition during milling . . . . .	38
2.9	SEM images of milling steps for a cantilever . . . . .	41
2.10	Cantilever undercut schematics . . . . .	43
2.11	Schematic of rotation of sample for thickness and length measurements . . . . .	44
2.12	SEM images of milling procedure for paddle structure . . . . .	47
3.1	Hysteresis loop experiment setup picture . . . . .	50
3.2	Hysteresis loop experiment setup schematic . . . . .	51
3.3	Close up of 45° mounted samples . . . . .	52

*LIST OF FIGURES*

3.4	Expanded image of sample for structure alignment . . . . .	56
3.5	Optical raster scan image of a cantilever . . . . .	57
3.6	Pictorial representation of averaging method . . . . .	62
3.7	Schematic of dither coil alignment over flap . . . . .	65
3.8	FMR experiment schematic . . . . .	67
3.9	FMR pump-probe timing diagram . . . . .	68
3.10	FMR setup modifications image . . . . .	69
4.1	Stoner-Wohlfarth uniaxial model vectors . . . . .	72
4.2	Conventional hysteresis loop example . . . . .	74
4.3	$dE/d\theta$ solutions showing no hysteresis . . . . .	75
4.4	$dE/d\theta$ solutions showing hysteresis origin . . . . .	76
4.5	Magnetization direction vs applied field direction . . . . .	78
4.6	Uniaxial SW model with normal and tilted sample at two field strengths . . . . .	79
4.7	Spherical coordinates used for the 3D biaxial and cubic anisotropy cases. . . . .	81
4.8	Biaxial model hysteresis loop changes with applied field magnitude	85
4.9	Biaxial model hysteresis loop changes with anisotropy and applied field strength . . . . .	86
4.10	Possible biaxial model hysteresis loop shapes . . . . .	86
4.11	Comparison of biaxial and cubic anisotropy models . . . . .	88
4.12	Second magnetization transition inverting with sample rotation .	89
4.13	Second magnetization transition changes with beam rotation projection . . . . .	89
4.14	Hysteresis loop projection effect of sample tilt. . . . .	90
4.15	Hysteresis changes from sample rotation relative to applied field	91
4.16	Changes in in-plane anisotropy strength . . . . .	91
4.17	Complex hysteresis loops and numerical errors . . . . .	92
4.18	Experimentally measured complex hysteresis loop . . . . .	93
5.1	Hysteresis loops of thin film LuIG mounted at normal beam incidence	96
5.2	Hysteresis in bulk LuIG mounted at $45^\circ$ to the beam . . . . .	98
5.3	Hysteresis loops at various polarization rotations . . . . .	98
5.4	Changes in hysteresis loops with hall probe position . . . . .	99
5.5	Applied field variation with magnet rotation . . . . .	100
5.6	Hysteresis loops in bulk LuIG at a various beam powers . . . . .	101

*LIST OF FIGURES*

5.7	Hysteresis loops in 4 $\mu\text{m}$ cantilevers at a various beam powers . . .	102
5.8	Hysteresis loops in 1.7 $\mu\text{m}$ cantilevers at a various beam powers .	102
5.9	Faraday rotation as a function of beam power for the cantilevers and bulk sample . . . . .	103
5.10	Comparison of averaging of hysteresis loops . . . . .	103
5.11	Hysteresis loops as a function of applied field magnitude, high field	105
5.12	Hysteresis loops as a function of applied field magnitude, low field	105
5.13	Faraday rotation through various flaps, high field . . . . .	106
5.14	Image of cantilevers for hysteresis loops . . . . .	107
5.15	Faraday rotation through various flaps, low field . . . . .	110
5.16	Scaled hysteresis loops for all cantilevers measured . . . . .	110
5.17	Maximum scaled Faraday rotation for flaps as a function of their thickness . . . . .	111
5.18	Faraday rotation per thickness as a function of inverse cantilever thickness . . . . .	111
6.1	FMR pulse generator comparison at 151 gauss . . . . .	114
6.2	FMR pulse generator comparison at 2000 gauss . . . . .	115
6.3	Image of two dither coils . . . . .	117
6.4	FMR differences between dither coils . . . . .	118
6.5	Changes in FMR in bulk LuIG at normal incidence with sample rotation . . . . .	119
6.6	Typical FFT with inset FMR ring down . . . . .	120
6.7	The FMR of thin film LuIG mounted normal to beam at 30, 151, and 380 gauss . . . . .	121
6.8	FFT's of thin film LuIG mounted normal to beam at 30, 151, and 380 gauss . . . . .	121
6.9	FMR frequency vs. field strength in thin film LuIG, calibrated field	122
6.10	FMR frequency vs. field strength in thin film LuIG, measured field	122
6.11	FMR in the bulk sample at normal incidence and $45^\circ$ . . . . .	123
6.12	FFT's of bulk LuIG at normal beam incidence and $45^\circ$ . . . . .	124
6.13	FMR repeatable after refocusing in a 1.7 $\mu\text{m}$ thick cantilever . . .	125
6.14	FMR in a 1.7 $\mu\text{m}$ thick cantilever at in-plane and out-of-plane 30 gauss bias field . . . . .	125
6.15	FMR in a 4 $\mu\text{m}$ thick cantilever at a 151 gauss bias field . . . . .	126
6.16	FMR in various cantilevers at 30 gauss bias field . . . . .	127

*LIST OF FIGURES*

6.17 FMR in various cantilevers at 151 gauss bias field . . . . .	127
6.18 FFT's of FMR in various cantilevers, 30 gauss bias field . . . . .	128
6.19 FFT's of FMR in various cantilevers, 151 gauss bias field . . . . .	128
7.1 Proposed reflection measurements schematic . . . . .	132
A.1 SEM images of wedge shaped cantilever prior to thinning . . . . .	140
A.1 SEM image of thinned cantilever . . . . .	140
A.1 SEM image of thin flexing cantilevers . . . . .	141

## List of symbols

$A$	Area
AI	Analogue input
$Al$	Aluminum
$B$	Magnetic flux density from applied field and magnetization
$Bi$	Bismuth
CW	Continuous wave
DAQ	Data acquisition
DIO	Digital input-output
$E$	Young's modulus
$E_a$	Anisotropy energy
$f$	Frequency
$Fe$	Iron
FIB	Focused ion beam (also abbreviation for focused ion beam microscope)
FMR	Ferromagnetic resonance
$g$	Gyromagnetic ratio
$Ga$	Gallium
GGG	Gadolinium gallium garnet
$h$	Applied field $H$ divided by the field $H_o$ which fully magnetizes the sample
$H$	Applied magnetic field from permanent magnet
$He^+$	Helium ion
HeNe	Helium-neon laser
$k_n$	Constant depending on the cantilever mode of vibration
KV	Kilovolts
$l$	length of cantilever
$I_y$	bending moment
IPA	Isopropyl alcohol
$K$	Anisotropy constant
LuIG	Lutetium iron garnet
$Lu$	Lutetium
$M$	Magnetization in material
$M_s$	Saturation magnetization
MEMS	Microelectromechanical systems
MeV	Megaelectron volt
MO	Magneto-optical effects, eg Faraday effect
$n$	Vibration mode number
nA	Nanoamps
NA	Numerical aperture
NEMS	Nanoelectromechanical systems
$nm$	Nanometres

$O$	Oxygen
pA	Picoamps
RF	Radio frequency
SEM	Scanning electron microscope
$Si$	Silicon
SNR	Signal to noise ratio
SW	Stoner-Wohlfarth
$t$	Cantilever thickness
TTL	Transistor logic
$U$	Potential energy of the dipole, Zeeman energy
XPS	X-ray photoelectron spectroscopy
$\mu m$	Micrometres
$\rho$	Density
$\beta_n$	Constant per unit length dependent on a cantilevers vibration mode
$\mu_o$	Permeability of free space
$\tau$	Torque on magnetic dipole
$\mu$	Magnetic moment
$\theta$	Angle of rotation, generally the tilt of the sample relative to the beam direction
$\phi$	Angle of rotation, generally the rotation of the sample around the beam axis
$\mu_B$	Bohr magneton
$\hbar$	Planck's constant

# Chapter 1

## Introduction

*This chapter will cover the motivations for studying magnetomechanical coupling. The basic theory of both the magnetic and mechanical aspects of magnetomechanical coupling will be discussed. What affects a cantilever's vibration resonance frequency, the fundamentals of a magnetic hysteresis loop, and ferromagnetic resonance are all outlined.*

### 1.1 Motivation for Studying Magnetomechanical Coupling

Magnetism has been a phenomenon of great interest and practical utility since its discovery. Its fundamental connection with electricity has made it extremely useful, while a new field of applications opened up as the size of magnetic devices shrank, such as modern data storage technology like hard drives and credit cards, and knowledge of their microscopic magnetic properties grew. [1,2] Nanoelectromechanical systems (NEMS) and the larger microelectromechanical sys-

tems (MEMS) are a broad class of structures on micrometre and sub-micrometre scales that combine mechanical and electrical aspects. Their small size can be engineered to make them sensitive to extremely small forces and/or to yield high mechanical resonance frequencies in the radio frequency range. [3] They are used in a wide variety of devices like telecommunication switches and respiratory flow sensors. [4,5]

For both NEMS and nanoscale magnetism, shrinking the system has brought advantages in improved speed. Combining these two systems opens another field of possible applications and ways to study fundamental problems in physics, and unique to the nanoscale is the possibility of overlapping ferromagnetic resonance (FMR) and mechanical resonance frequencies. Attempts towards combining these two systems have been demonstrated like the successful detection of a single electron spin by magnetic resonance force microscopy. [6]

Previous theoretical work has discussed the possibility of coupling the strain in the flexing crystal lattice of a mechanical NEMS device to the magnetization of a ferromagnet. [7,8] Such a coupling would open up a variety of experiments like using mechanical torques to detect spin currents. [7] The proposed method of studying such magnetomechanical coupling is to examine the effects of ferromagnetic resonance on mechanical motion of the ferromagnet, and vice versa. This coupling is expected to be strongest where the FMR and mechanical resonance frequencies overlap, and achieving an overlap is a main consideration of this thesis.

This thesis will set up one possible method of studying magnetomechanical interactions in magnetic cantilevers produced from lutetium iron garnet (LuIG) with a focused ion beam microscope (FIB). This material was found to have a large Faraday effect, reasonable mechanical properties, and a low FMR frequency compared to other magnetic materials like permalloy and is a promising material

for studying magnetomechanical interactions. The experimental infrastructure for making LuIG cantilevers, measuring their magnetic properties via hysteresis loops, and demonstrating ferromagnetic resonance in them was developed and taken to a level required for investigating magnetomechanical interactions.

## **1.2 Theoretical Background**

As the name suggests, magnetomechanical interactions requires understanding and control of the mechanical and magnetic properties of a cantilever. The theories describing a cantilever's flexing and the magnetism of small structures are described in detail in many other sources. [9–15] Their basics will be covered here to give the reader a brief understanding and a source for more information.

### **1.2.1 A Cantilever's Vibration**

The dynamics of flexing beams have been extensively studied and modeled by engineers and physicists. [10, 15] Despite our cantilever's small size, its flexing may be treated as if the cantilever still has bulk material properties. Results will diverge as the dimensions approach atomic scales but do not for the device sizes studied in this thesis.

How a material deforms elastically, that is in a non-permanent manner, in various ways in response to a force on it is governed by several elastic moduli and ratios. With these and a materials density the resonant frequencies of various structures can be calculated analytically, approximated analytically, or modeled numerically. Of the torsional and flexural vibrations of beams, cantilevers, and paddle structures, only the torsional motion of a doubly clamped cylindrical beam with a uniform cross section can be derived easily, and the rest require some level of approximation. [10] The torsional resonant frequencies for different modes  $n$

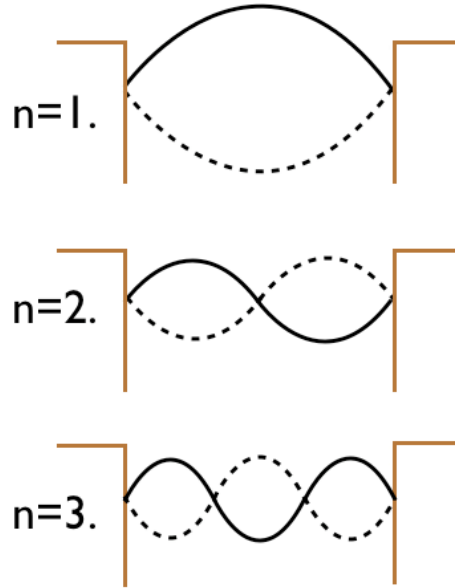


Figure 1.1: The first 3 flexural vibration modes of a doubly clamped beam of length  $l$

$n = 1, 2, 3, \dots$  of a cylindrical beam of length  $l$  are approximated by

$$f = \frac{n}{2l} \sqrt{\frac{E}{\rho}} \quad (1.1)$$

where  $E$  is Young's modulus and  $\rho$  the density. This formula loses accuracy for a more complicated structure such as a beam with a rectangular profile, and the resonant frequencies are better found from a finite element numerical model.

For flexural vibrations the resonant frequencies are approximated by

$$f = \frac{1}{2\pi} \sqrt{\frac{EI_y}{\rho A}} \beta_n^2 \quad (1.2)$$

Here  $I_y$  is the bending moment in the displacement direction,  $A$  the cross sectional area, and  $\beta_n = k_n/l$  a constant which depends on the mode and is found from boundary conditions of the beam. Young's modulus,  $E$ , is the ratio of stress over strain along an axis and gives how much a material stretches along the axis of a

force applied to it. For the first mode of a singly clamped beam (cantilever) of thickness  $t$  and length  $l$ ,  $k_1 = 1.875$ ,

$$f = \frac{1}{2\pi\sqrt{12}} \frac{t}{l^2} \sqrt{\frac{E}{\rho}} k_1^2 \quad (1.3)$$

This assumes that the beam is long relative to its width and thickness. The formula is more complicated for beams where this does not hold, or for a beam with a paddle geometry. Numerical simulations can give quite accurate results and are required to get accurate frequencies for paddle structures.

Obtaining an overlapping ferromagnetic resonance and mechanical resonance frequency requires a high mechanical frequency, and relatively low FMR frequency. From the formulas we see that a short beam of low density and high Young's modulus gives high torsional resonant frequencies. Similarly a short, stiff beam of low density is desired for high flexural vibration frequencies. Since our group has experience with the actuation and detection of mechanical vibrations in similar cantilevers, this mechanical component of magnetomechanical coupling is not studied in this thesis. [16, 17]

### 1.2.2 Classical Model of Magnetism

The magnetization behaviour which gives rise to hysteresis loops and ferromagnetic resonance has been studied and discussed in depth in other sources. [11, 12] A comprehensive overview will not be given. Instead, a reminder of the principles that should be kept in mind when considering the goal of studying magnetomechanical interactions will be presented.

All electrons in a material have a magnetic moment arising from their orbital and spin angular momentum. In most materials these individual electron magnetic moments are oriented randomly, and the material is called non-magnetic. In

some materials the individual dipoles align in a way such that their net magnetic moment is non-zero. Such a material is magnetic, and how the dipoles align such as spontaneously or in the presence of an applied field to produce a net effect, produces the type of magnetism, such as ferromagnetism or paramagnetism. The magnetization is the net effect of dipoles within a region.

The alignment of dipoles to minimize the energy of the system is complicated by many effects. Magnetic moments try to align or anti-align, depending on their magnetic moment, with an applied field. Magnetic moments within a sample may align in particular directions to produce domains, regions of a uniform magnetization, rather than align uniformly throughout a sample. A material's crystal structure may make it energetically favourable for moments to align in particular directions giving a crystalline anisotropy, the shape of a material or structure introduces shape anisotropies, and temperature can affect the ability of domains to align. The interplay of these contributions gives rise to macroscopic effects which are visible in this thesis' experiments.

To avoid confusion,  $H$  will be used to refer to the auxiliary magnetic field applied by the permanent magnet to the sample, and  $B$  refers to the magnetic flux density such that  $B = \mu_o H + M$  with  $M$  the sample magnetization and  $\mu_o$  the permeability of free space.

Of primary importance is the torque  $\tau$  on a magnetic moment  $\mu$  from a magnetic field  $B$ ,

$$\tau = \mu \times B \tag{1.4}$$

and potential energy of the dipole from the applied field,

$$U = -\mu \cdot B \tag{1.5}$$

These formulae underly the two experimental techniques of this thesis. If we vary

an external magnetic field slowly relative to the time scale on which the magnetization can change, we measure the equilibrium response of the magnetization to the applied field  $H$  and obtain a hysteresis loop. If we probe the magnetization state on time scales shorter than its response to an applied field we are measuring its non-equilibrium dynamics, which is done with ferromagnetic resonance.

### 1.2.3 The Faraday Effect

The Faraday effect is a magneto-optical (MO) effect describing the changes in polarization of light in a medium in response to a magnetic field applied in the direction of propagation of light within the medium. [14] The magneto-optical Kerr effect is an analogous effect from light reflected off a medium rather than transmitted through it. Both arise when the refractive index of a medium is not independent of polarization. In this case a beam propagating through it will experience circular birefringence and dichroism where right and left circular polarized beams propagate with different speeds and attenuations. The result is that a polarized beam propagating through the medium will have its polarization rotated and/or some ellipticity introduced. The resulting change in light polarization due to an applied magnetic field is the Faraday (or Kerr) effect. For linearly polarized light the angle of rotation is proportional to the magnetization within the material and the distance of propagation through it by the beam. With this, the changes in polarization of a beam propagating through a sample can be used to measure the component of the magnetization in the beams direction, both statically for a hysteresis loop and dynamically in ferromagnetic resonance. It also allows changes in thickness of the sample to be taken into account as the rotation is proportional to the propagation length.

### 1.3 Hysteresis Loops

Ion implantation of magnetic materials is known to change their magnetism. [18–20] As the FIB mills, it leaves some ions implanted in the unmilled material. [21] If this damages the magnetization it is expected to be detectable through changes in the magnetic properties of different thickness cantilevers.

Hysteresis loops are the primary way of analyzing a material’s magnetic properties. A hysteresis loop is a plot of the history of magnetism induced in a material from an applied magnetic field. Some materials have magnetization responses to applied fields that are determined in part by the history of magnetization within it in addition to the currently applied field. This is a result of energy barriers to magnetization changes and can be caused by anisotropy in the material, domain walls, or other effects. Typically the applied field is varied from  $H$  to  $-H$  and back to  $H$ , and the resulting magnetization in the material measured. Hysteresis loops are commonly shown as both  $B$  vs  $H$  and  $M$  vs  $H$  plots as  $B$  varies linearly with  $M$ . Figure 1.2 shows a typical hysteresis loop. An un-magnetized sample will start out at  $M = 0$  for  $H = 0$ . As  $H$  increases the magnetization increases until saturation. As  $H$  is reduced back to zero, the magnetization stays at some finite level, called the remanence, at  $H = 0$ . Increasing the field strength towards  $-H$  causes the domains to begin changing orientation and the magnetization reverses at a point called the coercivity until it saturates at  $-M$ . The shape of a hysteresis curve can vary extensively, from a nearly linear line to a plot with vertical transitions between saturation at  $M$  and  $-M$  where all the domains flip at once. Comparing this shape under different conditions like a thin film sample vs cantilever, different applied field strength, or ion implantation conditions can give knowledge of the magnetization within the sample. In this way hysteresis loops are used to analyze samples, with the primary goal of looking for ion damage effects resulting from producing the LuIG cantilevers.

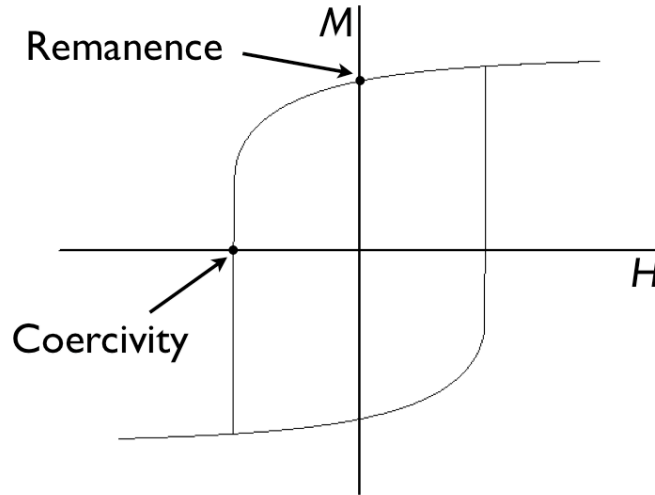


Figure 1.2: A standard hysteresis loop of a material with uniaxial anisotropy, produced with a Stoner-Wohlfarth model where the applied field strength, but not direction, is varied. The magnetization is saturated when  $M$  reaches it's maximum, which occurs for some high field  $H$  and  $-H$ . The remanence is the remaining magnetization in a material with no applied field. Coercivity is the applied strength necessary to change the magnetization direction in the material.

The standard method of obtaining a hysteresis loop involves varying the magnetic field strength from one polarity to another and back in a constant direction through the sample. This has the advantage that the magneto-optical effects being measured depend only on the applied field strength, not direction, and allows effects that vary with particular axes in the sample to be easily separated. Varying the applied field strength either requires an electromagnet or a moveable permanent magnet. Electromagnets are bulky and reasonably priced ones have relatively small pole separations in which to mount a sample. The large currents required for strong fields, especially in a magnet with a large pole separation, necessitate a relatively slow ramping of the field strength. In addition, the high currents in an electromagnet cause heating which can physically shift the sample. [11] A moveable magnet to vary the field in only one direction is a similarly slow method. The magnet must be physically moved away from the sample, ro-

tated to change the polarity, and brought close to the sample again. Stability and repeatability of the Faraday signal is a problem during these measurements. It is probable that the relatively long times required for the measurement allow the various optical and mechanical components to randomly drift slightly, preventing averaging from significantly improving the SNR. Excellent stability is needed to measure the thin cantilevers with their small signal.

An alternative method is to rotate a permanent magnet near the sample, varying the field direction, as in Figure 1.3. [22] This is more complicated due to the changing direction of the field which will bring in MO effects from a variety of sample axes. In this method the field strength varies slightly but does not go through zero. MO effects are explored by changing the direction of magnetization in the sample which may give rise to more complicated hysteresis loops due to multiple magnetization switches within the sample. These multiple switches may occur if there are multiple directions within the sample along which it is energetically favourable for the magnetization to lie along. A big advantage to this method is that the magnet may be rotated quickly, allowing many hysteresis loops to be recorded in a short period of time. After averaging, such loops can show small signals that would be otherwise swamped by drift in a conventional hysteresis measurement. After trying conventional hysteresis loops, both with an electromagnet and linear movement permanent magnet, the rotational hysteresis loop method was used in this thesis.

### 1.3.1 Rotational Hysteresis Loops

As a record of the magnetization in a sample in response to an applied magnetic field, recording a hysteresis loop requires a way of measuring the  $B$  field resulting from the applied  $H$  field. Measuring  $H$  is easy, and is done with a Hall probe placed near the sample.  $H$  is varied by moving a permanent magnet, either ver-

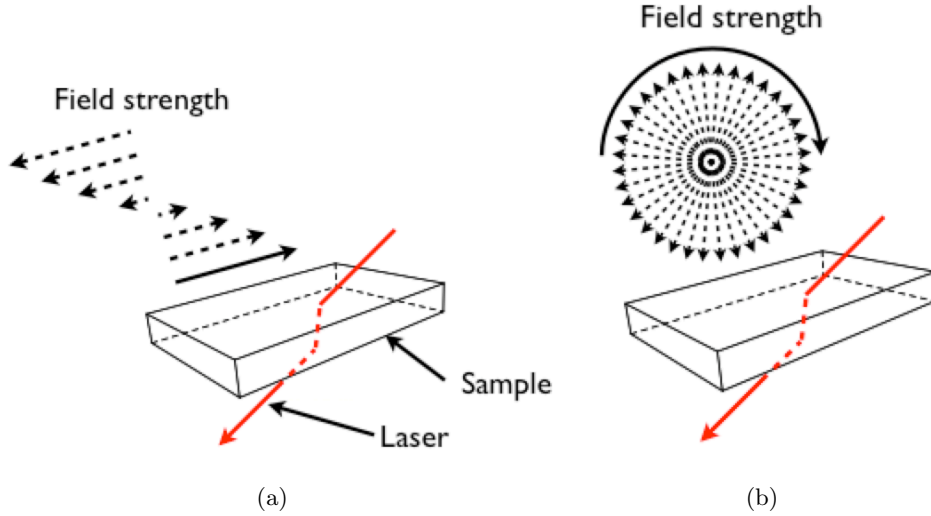


Figure 1.3: Typical hysteresis measurements involve varying the applied field in a fixed direction, from  $H_0$  to  $-H_0$  and back, as in (a). The field is generally applied along the sample surface, with the laser picking up Faraday effect through the component of the beam in this direction. In our setup a magnet is rotated such that the field strength stays constant but changes direction, as in (b).

tically to change the field strength at the sample, or by rotating it to change the direction and obtain a hysteresis loop. Most of the complexity in the experiment comes from measuring the  $B$  field.  $B$  is measured within the sample by using a polarized laser passing through the sample and the Faraday effect which rotates the polarization depending on the  $B$  field within the material. As the  $B$  field arises from the magnetization, measuring  $B$  directly gives us information about the magnetization. With a rotating magnetic field,  $B$  may reach saturation but the plot will still not look like a conventional hysteresis loop, instead being a generally circular shaped plot with sudden jumps in the data. These jumps correspond to sudden magnetization switches, which would be the hysteresis of a conventional hysteresis loop experiment.

Sudden magnetization switches result from the interplay between the competing energies of the applied field and the anisotropy on the direction of the magnetization, and is discussed in more detail in the Modeling section. There

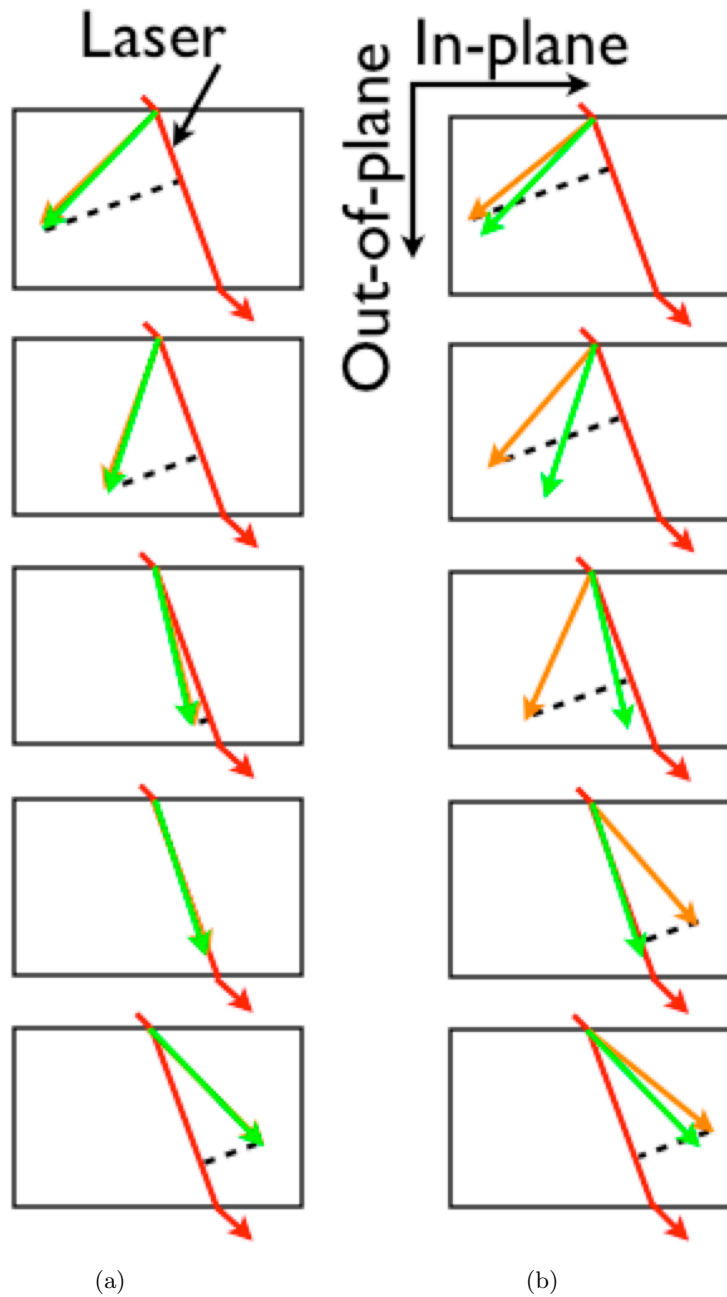


Figure 1.4: LuIG's in-plane anisotropy strongly resists the magnetization (orange vector) pointing into the sample, here represented by the black square. (a) With a strong enough applied field (green vector) the magnetization (orange vector) will closely follow it, resulting in a smooth hysteresis plot with no sudden transitions in magnetization. (b) Weaker applied fields are not strong enough to force the magnetization directly down into the sample. As the applied field continues to rotate the magnetization is left behind. The applied field tries to magnetize the sample in the opposite direction from which it is pinned, and beyond a certain point it is energetically favourable for the magnetization to suddenly switch to the new orientation. This switch combined with the projection effect on the beam direction produces a sudden change in the measured Faraday signal.

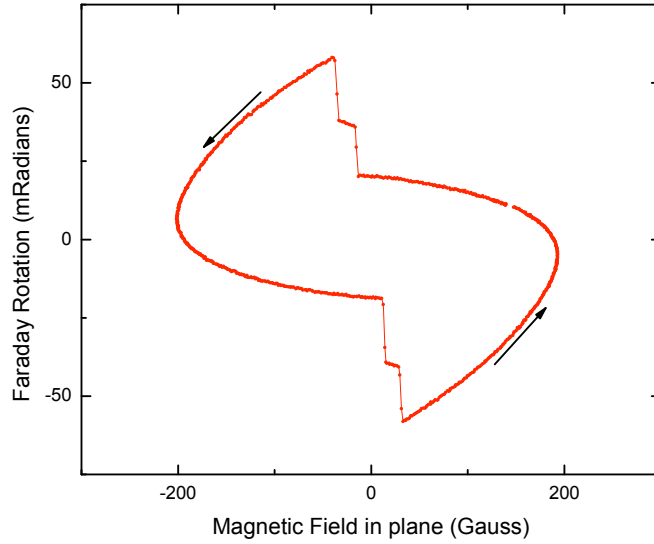


Figure 1.5: A typical rotational hysteresis loop measured in lutetium iron garnet. The field strength is fixed at 200 gauss, and the direction varied. The measured Faraday rotation of the polarized beam is shown in milliradians as a function of the measured magnetic field in the plane of the sample. The double transition in magnetization is visible in the two sudden steps in rotation amplitude. This is characteristic of transitions in the cubic anisotropy of LuIG. The arrows show the direction in which the magnetization moves.

are preferred directions, the anisotropy, within the sample that the magnetization tries to lie along such as in the plane of the sample surface, and directions it resists pointing along such as into the sample. Against this the rotating magnetic field tries to force the magnetization to align in its direction. Sudden magnetization switches result when the applied field moves some small amount, triggering the magnetization vector to leave one equilibrium direction and point in a significantly different other direction. For example, a magnetization switch can occur when the applied field tries to force the magnetization into the plane of the sample, but is not strong enough to fully do so, see Figure 1.4. The hysteresis loop shape, an example of which is shown in Figure 1.5, is dependent on other factors besides the anisotropy and applied field strength and direction. This is discussed in detail in the Modeling and Results chapters, but the shape depends mainly on the sample orientation and beam projection effects. The typical orientation of

the sample is shown in Figure 1.6. The polarized beam passes through the sample at some angle  $\theta$ . The sample may be rotated in  $\phi$ , and the magnet rotated to vary the direction of the applied field  $H$ . The measured Faraday rotation is proportional to the component of magnetization in the direction of the beam. This is important, as changing the direction of the beam can significantly affect the signal amplitude measured. For example Figure 1.7 shows how two magnetization directions (orange lines) can give the same or significantly different Faraday rotation amplitudes depending on the beam direction through the sample.

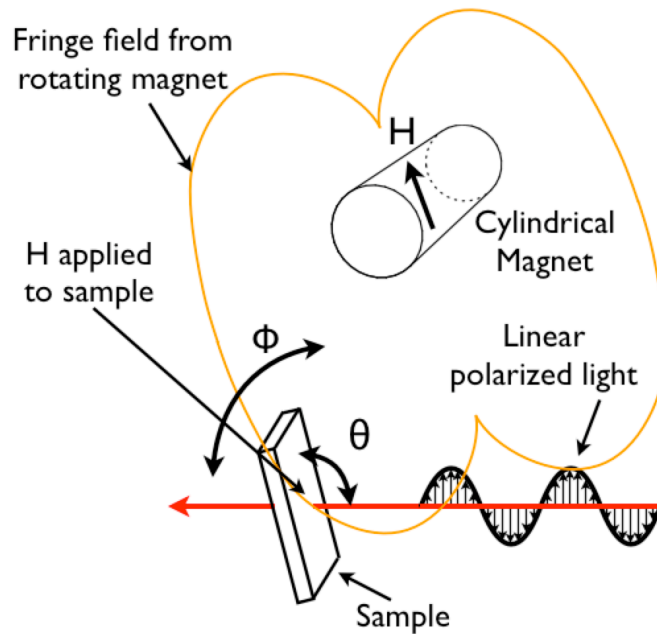


Figure 1.6: A schematic of the sample interactions.  $\theta$  determines the sample tilt angle ( $90^\circ$  is the beam normal to sample surface) and  $\phi$  the rotation of the sample around the beam (red line). The magnetic field can be independently varied in  $\theta$  but not in  $\phi$ , and interacts at some point where the fringe field crosses through the sample. The laser linear polarization direction can be independently varied in  $\phi$ .

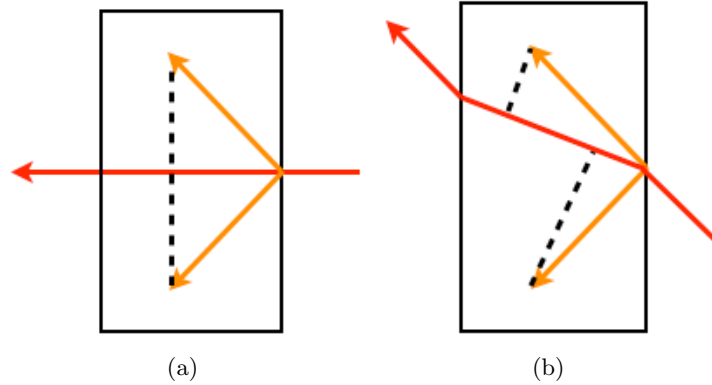


Figure 1.7: Different beam directions can produce significantly different hysteresis plots for the same magnetization changes. In (a) if the magnetization switches between the two directions (orange vectors) the projection of magnetization onto the beam will be the same and no change in Faraday rotation is seen. In (b) the beam passes through the sample on an angle, and so changes in the magnetization direction can have a large effect on the Faraday rotation as it is proportional to the component of magnetization in the direction of the beam.

## 1.4 Ferromagnetic Resonance

Ferromagnetic resonance is an effect occurring when the magnetization within a sample is not in equilibrium with an applied field and tries to align with it due to the dipole torque of equation 1.4. Conservation of total angular momentum results in the magnetic moments and thus magnetization direction precessing around the applied static field direction as it tries to align with it. This is similar to a top precessing under the torque from gravity. This precession is ferromagnetic resonance, and can be imagined pictorially in Figure 1.8. In a completely magnetized isotropic thin film and an in-plane applied field  $H$  the FMR precession frequency is given by the Kittel FMR formula, [23,24]

$$w = \frac{g\mu_B}{\hbar} \sqrt{(H + 4\pi M_s)(H)} \quad (1.6)$$

where  $w$  is the angular precession frequency and  $M_s$  the saturation magnetization of the film.  $\mu_B$  and  $\hbar$  are the Bohr magneton and Planck's constant. Ferromag-

netic resonance in materials is complicated by shape and crystalline anisotropies, and this formula may have to be modified to some degree. [13] In some garnets, such as yttrium iron garnet, this formula does hold accurately and it is not clear why it does not in LuIG. [24] FMR in lutetium iron garnet is complicated by its different in-plane and out-of-plane anisotropies, and in cantilevers the strong shape anisotropies must be taken into account in any eventual form of the Kittel FMR formula.

Measuring a component of FMR normal to the precession axis in a material with no anisotropy gives a typical FMR ring down curve, shown in Figure 1.9. By varying the applied static field, the FMR frequency can be varied to overlap with a sufficiently high mechanical resonance frequency. At or near overlap we may see a variety of effects as the FMR and mechanical motion energetically couple together, such as a decrease in the FMR ring down time as an additional damping channel of the FMR is opened up through coupling to the mechanical motion of the cantilever.

This thesis will demonstrate FMR in cantilever structures, setting the initial experimental framework for measuring magnetomechanical interactions. In this work we measured LuIG FMR frequencies in the 300MHz range, which with equation 1.3 would require a cantilever of dimensions  $1\mu m$  long and  $0.5\mu m$  thick to achieve a frequency overlap for magnetomechanical coupling.

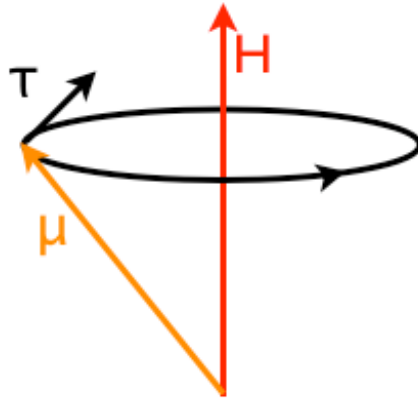


Figure 1.8: The static applied field  $H$  applies a torque to a dipole moment  $\mu$ . As  $\mu$  returns to alignment with  $H$ , it precess around  $H$  shown by the black circle.

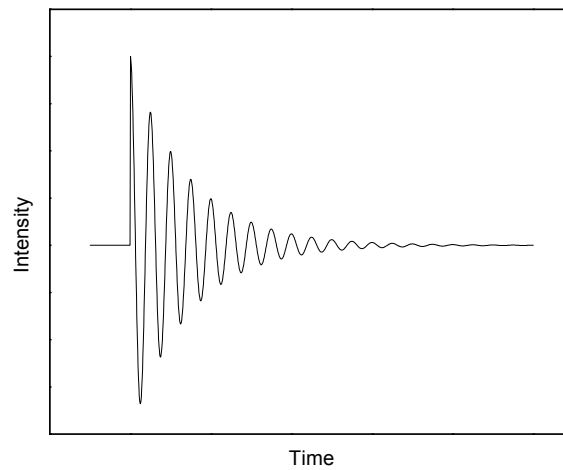


Figure 1.9: A schematic showing an ideal FMR ring down curve for a uniform material. The initial peak is the  $t = 0$  time of excitation, after which precession gives the oscillations which damp down with time.

## Chapter 2

# Making NEMS Cantilevers

*Magnetomechanical coupling should be detectable in a ferro or ferrimagnetic cantilever. [7, 8] This chapter discusses the merits and disadvantages of some of the different approaches towards making a suitable cantilever and the reasons for choosing lutetium iron garnet. How to mill a LuIG cantilever with a focused ion beam microscope is discussed in depth. This includes sample preparation, milling challenges with the FIB such as charging and re-deposition, and the milling procedure to produce cantilevers, doubly-clamped beams, and torsion paddle structures. How to measure the beam thickness from scanning electron microscope (SEM) images is also discussed.*

### 2.1 Making a Cantilever Overview

The magnetomechanical interaction is expected to arise from a coupling between the strain within the magnetic material and its ferromagnetic resonance [7, 8]. A variety of magnetic materials should exhibit this coupling, and which one is

best for study will be based partly on manufacturing considerations and partly on material properties. The primary consideration is to obtain an overlap of the FMR and mechanical frequencies. An overlap may not be necessary to detect the coupling, but coupling is expected to be much larger on resonance.

Our group has been pursuing three different magnetic cantilevers for studying magnetomechanical interactions. These are conventional silicon cantilevers with a permalloy region deposited on the cantilever, cantilevers made entirely from permalloy, and cantilevers made from lutetium iron garnet. Si cantilevers with a permalloy magnetic layer have the advantage of being manufactured using well established nanofabrication methods, Si and permalloy both being commonly deposited and etched. The magnetic layer will flex with the underlying Si substrate, producing a strain field just as if it made up the bulk of the cantilever and creating the expected magnetomechanical interaction. However, our group has had difficulty depositing permalloy onto the cantilever and getting it to remain there during etching of the Si substrate. In addition, their small magnetic volume will give a smaller magnetomechanical coupling, smaller FMR, and smaller mechanical response to magnetic actuation. Because of this our group switched to pursuing cantilevers made entirely of permalloy.

Cantilevers produced from permalloy generally curl immediately after release from the substrate due to the uncontrolled thin film stress. A group under Dave Mitlin at the National Institute of Nanotechnology at the UofA specializes in controlling the stress of deposited thin films, and our group is collaborating with them. With controlled stress permalloy cantilevers can be made using conventional lithography. The entire cantilever is magnetic giving a large magnetic volume for the magnetomechanical coupling.

Lutetium iron garnet has promising material properties. With equation 1.3 we can compare the mechanical frequencies of materials by comparing  $\sqrt{E/\rho}$ .

For silicon this is  $\sim 8,000$  m/s, and our group has measured  $\sqrt{E/\rho}$  for permalloy and LuIG to be  $4.8 \cdot 10^3$  m/s and  $3.8 \cdot 10^3$  m/s respectively. Silicon has better mechanical properties, while permalloy and LuIG are similar. The main benefit of LuIG over permalloy is that we have measured its FMR frequencies to be around 7.5X lower than permalloy, making achieving an FMR and mechanical frequency overlap easier. [11]

## 2.2 Lutetium Iron Garnet Properties

Magnetic garnets are a class of materials with extensively studied properties. [13] Garnets are a naturally occurring mineral with the general formula  $X_3^{2+}Y_2^{3+}(SiO_4)_3$ , where X and Y are arbitrary ions. Magnetic garnets are a related structure and generally have Fe in place of Si. Rare-earth iron garnets such as yttrium iron garnet are the most common, with a formula  $R_3Fe_5O_{12}$  where  $R$  is an element like yttrium, gadolinium, or lutetium. Their magnetic properties are strongly dependent on additional atoms substituted for some of the rare-earth atoms, with bismuth being among the most common.

The material studied in this thesis is expected to have the composition  $(BiLu)_3(FeGa)_5O_{12}$  from the data sheet supplied with it. [25] This would make it a bismuth substituted lutetium iron garnet, and has been referred to as LuIG throughout this thesis. X-ray photoelectron spectroscopy (XPS) measurements of LuIG gave us confusing results. The LuIG film thickness and gadolinium gallium garnet (GGG) substrate are as expected, while the LuIG composition is not. Bismuth and iron are detected in atomic concentrations of a few percent, while gallium and lutetium were not detected. The XPS data is dominated by carbon and oxygen, despite cleaning of the surface. Phosphorus, nitrogen, and aluminum are all present in similar contributions to lutetium and iron and it is possible that the XPS is not able to distinguish gallium and lutetium from the

contributions of other elements. XPS data of a bismuth substituted yttrium iron garnet sample showed no bismuth, but did detect moderate amounts of yttrium and iron in a ratio differing by a few percent from the expected one. The exact ratio depends on the bismuth substitution which is only approximately known. There was approximately 2.5 times more oxygen than expected from the amounts of iron and yttrium. From this comparison we do not think the XPS data is reliable.

Not knowing the exact composition makes it difficult to compare results to the literature, although there is not much research in the literature as LuIG is not a well studied garnet. Future cantilevers may be made from a different magnetic garnet with a more accurately known composition and magnetic properties. Regardless of the exact composition our results are consistent with the material being a magnetic garnet with desirable properties, and the procedures and results in this thesis should apply to a variety of other magnetic garnets suitable for studying magnetomechanical coupling.

It is difficult to make cantilever structures from LuIG. LuIG must be grown as a single crystal via liquid phase epitaxy on a lattice matched substrate, and so cannot be deposited on a sacrificial layer for the liftoff or release steps of fabrication. Our samples consist of a  $\sim 500 \mu\text{m}$  thick gadolinium gallium garnet (GGG) substrate and a  $3 \mu\text{m}$  thick LuIG thin film capped with a  $\sim 100 \text{ nm}$  thick Al protective layer. They are made by Joy Systems in West Lafayette, Indiana. The GGG substrate on which LuIG is grown could in theory be used as a sacrificial layer, but it is etched by the same etchant as LuIG, preventing this. Ion slicing and focused ion beam milling were proposed and subsequently investigated as solutions to this manufacturing problem.

## 2.3 Ion Slicing

Ion slicing is a method used to create thin layers from a variety of single crystal materials suffering from the same manufacturing issues as LuIG; that is they cannot be deposited on a sacrificial layer. [26–28]. In ion slicing, a high energy ion beam implants ions, usually  $\text{He}^+$ , into a material. Ions stop at a depth in the crystal given by their energy, and by implanting with ions from a narrow energy distribution the ions implant at a known depth. At a 3.8 MeV implantation energy the ions implant at about 10  $\mu\text{m}$  in LuIG in a 2  $\mu\text{m}$  thick layer. If the material has a crystal structure, the ions damage the crystal lattice where they penetrate through, and especially where they come to rest within the material. A short high temperature anneal can repair the damaged lattice where ions have passed through while being unable to remove the buried layer of implanted ions and associated damaged lattice [26–28]. The buried damaged lattice layer etches up to 1000X faster than the bulk crystal, and so acts as a sacrificial layer and allows layers of LuIG to be separated into thin films, Figure 2.1 Implantation changes the magnetization by reducing the anisotropy field, although this is fully recovered with the anneal and detachment of the thin film. [27, 29]

It may be possible to create the sacrificial layer through ion implantation, and then etch the material to both create the structures using a mask and release them at the same time. This is unlikely to work well because of the significantly different rates at which the sacrificial layer and bulk material etch, ( $\sim 1000\text{X}$ ) although this could be taken into account in the structure’s designed dimensions such that they etch to the correct size.

Previous groups have shown that the crystal layer may be detached from the bulk sample by etching through the sacrificial layer and bonding the crystal layer to a new substrate to create thin fracture free films. [28] This ion slicing method was tried in LuIG; however, a number of problems led to this approach

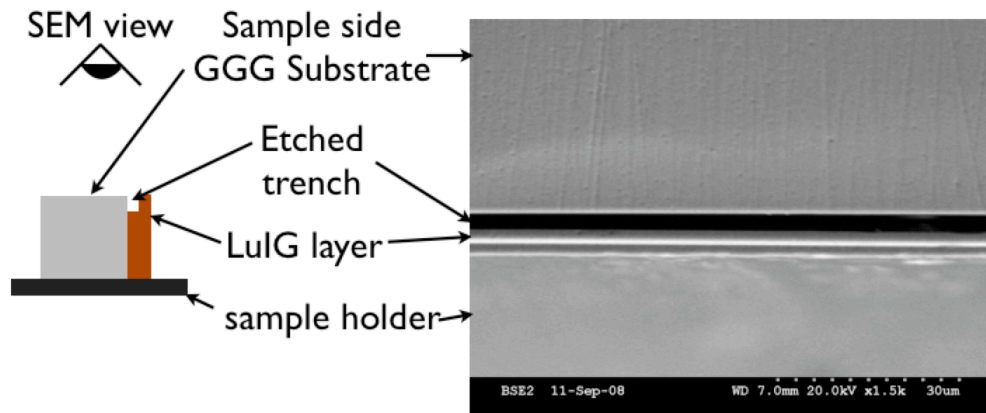


Figure 2.1: This is an SEM crosssection of the sample, with a schematic of the SEM view of the sample. The thick GGG substrate is at the top of the image, with the thin LuIG layer seen in profile part way down. The bottom of the image is the out of focus holder below the sample. The sample was implanted through the top LuIG surface, which is hidden from view except for the edge of the LuIG layer. Implantation was with a 3.8MeV He<sup>+</sup> ions in a 0.1 microamp beam, for a total fluence of 5X10<sup>16</sup> ions/cm<sup>2</sup>. Following ion implantation a rapid thermal anneal was done at 700C in 5% hydrogen and 95%nitrogen for 20 seconds. The sample was etched for several minutes, creating the etched trench visible in the image.

being abandoned in favour of milling cantilever structures using the FIB. Bonding the bulk LuIG to a new substrate and etching through the ion implanted layer was completed, but left a very rough thin film that wasn't suitable for creating structures.

If the crystal layer is to be detached completely, a sacrificial layer must be deposited on top of the LuIG which is then bonded to a substrate (Figure 2.2), which was done successfully. Attempts were made to deposit a protective layer on the side walls of the sample to prevent etching of the sacrificial layer (which is only exposed at the sample edges) until the desired structure profile had etched down from a lithographic pattern on the top surface. At this point, the undercut would form, releasing cantilevers. This did not work, with etchant still finding its way through the protective side layer into the sacrificial layer. The much faster sacrificial layer etch rates mean that any etchant in that ion implanted layer will etch through before significant etching of the undamaged LuIG is accomplished.

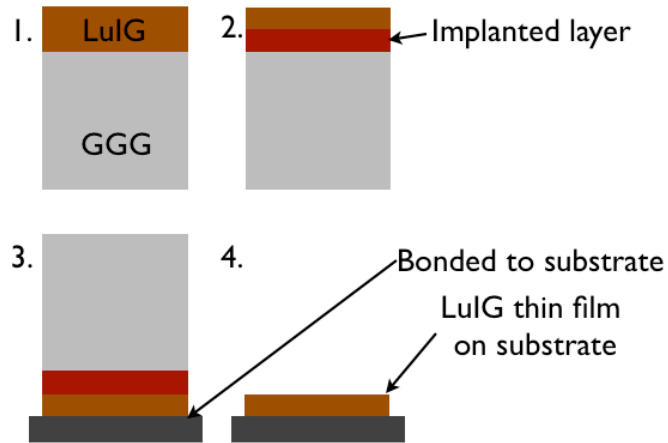


Figure 2.2: To create a thin film of LuIG for conventional lithography, a sample of LuIG (1) is implanted to create a buried sacrificial layer (2). The LuIG layer is bonded to a substrate (3). After bonding the LuIG buried layer is etched through, releasing the GGG substrate and leaving a LuIG thin film on a new substrate.

It is possible that with polishing of the sample side walls and a thick deposition the sacrificial layer could still be protected.

Recent work has been done to produce ion sliced films of sub micrometer thicknesses. [30] These films show a smooth surface and various studies confirm the film retains the bulk material properties. This method is not easy, especially requiring precise control over the annealing of the film. This equipment was not available at the University of Alberta and so implantation and annealing were performed at the University de Montreal by Dr. Sjoerd Roorda. Magneto Optical Kerr Effect measurements of the ion implanted and/or annealed samples indicated that the implantation was unexpectedly destroying the magnetism of the sample and it was not being recovered by the anneal. Troubleshooting the above problems in Montreal is difficult. After increasing successes in FIB milled cantilevers, this ion slicing attempt of making cantilevers was abandoned.

## 2.4 Focused Ion Beam milled Cantilevers

### 2.4.1 Focused Ion Beam Milling Overview

Focused Ion Beam (FIB) milling is an established technique which allows precise machining of 3D structures in a variety of materials on the micrometre and nanometre lengths scales. A FIB is similar to a scanning electron microscope in that a variety of electromagnetic fields are used to accelerate and focus a beam of charged particles, but use ions, usually Gallium, instead of electrons. The large momentum of these ions causes sputtering of the sample surface that they collide with, and with precise control of the beam the sample can be milled in a controlled manner. Milling rates depend principally on the sample properties and the amount of charge incident on a region if the beam energy is fixed, and a 30 kV beam was used throughout this project. The amount of charge deposited depends on the beam current, dwell time, and beam spot size, although the instrument fixes the spot size for a given beam current. The FIB software has various material properties programmed in so that for a given desired mill volume and beam current the dwell time is calculated automatically. The milling properties of LuIG were found to be similar to that of silicon and so it's settings were used. Milling is then simplified in that only the desired shape and depth of the milled region needs to be entered, and then a milling current chosen (referred to as the probe) after which the FIB software completes the calculations and performs the milling automatically. By rotating the sample so that it may be milled from different directions a large variety of 3D shapes may be milled from a material, such as the cantilevers of this thesis. Practical milling is complicated by a variety of other issues, discussed in the subsequent sections. The goal is to produce cantilevers of a sufficient size to study FMR and a magnetomechanical coupling, while if possible minimizing ion damage from the FIB milling in case

this damages the LuIG magnetization.

### 2.4.2 Sample Preparation

Achieving a clean sample surface is crucial for milling precise structures. Milling removes material in a nearly uniform manner so that the profile of a rough sample surface before milling including contaminants is transferred down to the bottom of the milled area. Contaminants may scatter the FIB beam if they mill or charge at different rates than the sample or reduce the quality of the optical beam transmitted through the sample which is used during eventual magnetic and mechanical measurements. It is difficult to clean surfaces with the FIB beam itself, and cleaning may also introduce additional ion damage.

The milling recipe for our cantilevers requires them to be milled from two orthogonal directions, which is easiest at the edge of our sample. Accurate milling of our structures requires two smooth surfaces at  $90^\circ$  to each other. LuIG cannot be cleaved, and so our samples are cut from a wafer with a Diamond Touch dicing saw at the UofA Nanofab. The saw blade leaves rough score marks making the side surface where it is cut unsuitable for milling despite the top surface being smooth, so the sample side is polished in the following steps:

1. Start with clean LuIG sample with the Al protective layer left on.
2. Cover the sample with a photoresist layer. (Optional.)
3. Mount the sample on an aluminum mounting block with wax.
4. Polish sample.
5. Remove sample from block with acetone and IPA.
6. Etch off Al protective layers.

These steps will be discussed in detail because milling of cantilevers cannot be accomplished without a clean sample surface and the polishing procedure was not straightforward. A schematic of the polishing is shown in Figure 2.3 and

pictures of polishing setup in Figure 2.4.

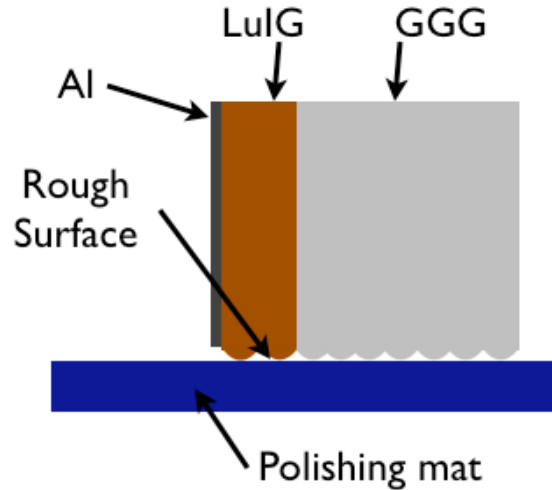


Figure 2.3: After cutting individual samples from a wafer, the dicing saw leaves score marks, shown here by the rough surface. The side of the sample is pressed onto a spinning polishing mat to create a smooth surface.

1. The sample should first be cleaned with Acetone, IPA, and then blown dry. The aluminum protective layer is left on.

2. HPR504 photoresist was used to cover the sample prior to mounting. This was done by placing drops of photoresist onto the sample with a cleanroom Q-tip, and baking it at 115° C for 90 seconds. Generally the sample can be placed on a piece of Si while covering it with the photoresist and baking. While mounting with hot wax this photoresist has melted off, perhaps from overheating of the wax. Multiple layers of photoresist were tried, etch baked before the next layer was deposited, with final results worse than the single photoresist layer. Several samples were covered in a single layer of photoresist which remained on the sample until after polishing. These were the cleanest samples prepared so far although whether this is due to the photoresist isn't known.

3. The polishing setup consists of a 3 legged polishing block holder, a small aluminum polishing block inset into the holder, and the polishing mat on a

rotating table, see Figure 2.4. The LuIG sample is mounted on the aluminum polishing block with hot wax that melts at  $\sim 100^\circ$  C. This is done by heating the aluminum polishing block to  $\sim 200^\circ$  C (hot plate scale, not actual temperature) on a hot plate, and dropping a small kernel of wax onto the center of the block along the polishing edge. After the wax kernel fully melts the LuIG sample is pressed gently into place in the wax. Additional wax may be added to completely cover the sample which helps protect it during polishing. Surface tension of the wax usually pulls the LuIG into the middle of the wax bead, preventing the sample from overhanging the edge of the Al block as is required for polishing. This problem is fixed by taking the polishing block with sample off the hotplate to cool on a small metal plate. The sample position is adjusted with tweezers while the wax solidifies, insuring that it remains overhanging the Al block edge after the wax hardens. It is necessary to push the sample down gently with tweezers so that it is flush with the aluminum block and not suspended at an angle by wax underneath, as well as insuring that it is approximately straight off the block edge. This makes eventual milling easier by insuring the edges are at right angles to each other. It's worth keeping two pairs of tweezers handy as the sample frequently will stick to the tweezers handling it, so the second pair can be used to keep the sample on the block when the first pair is removed. Best results were with the Al layer facing away (down on the mounting block) from the polishing direction. This helps to ensure that any particulate on the polishing mat is swept away from the Al layer, not towards it. Enough wax is used to cover the entire sample which also helps protect the surfaces during polishing.

4. Polishing is done by mounting the polishing block with overhanging sample in the tripod holder and withdrawing the legs with micrometers until the sample touches the polishing mat. The third leg is then withdrawn allowing the weight of the holder to be supported by the two remaining polishing legs and the over-

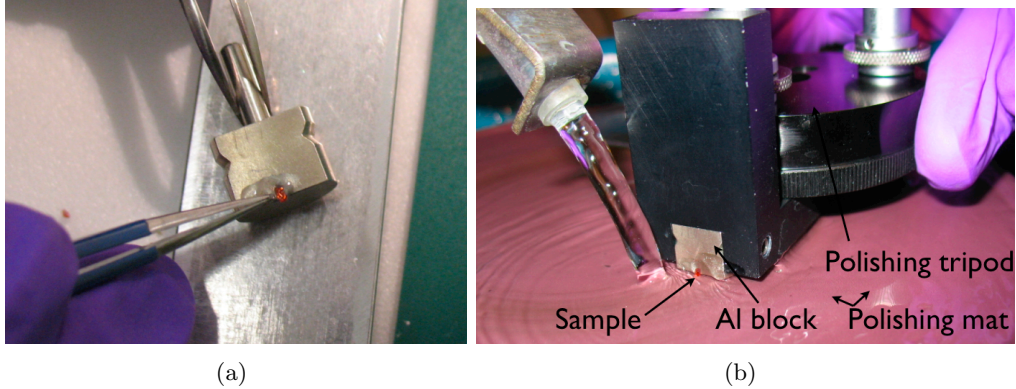


Figure 2.4: (a) The LuIG sample is held at the edge of the Al block as the wax dries, after removing the block from the hot plate (b) The polishing setup being held on the spinning polishing mat.

hanging sample. With the polishing block removed the holder can be calibrated to be parallel to the polishing mat by resting it on a flat surface with all three legs withdrawn, and then extending them down until they make contact with the flat surface and begin to raise the holder. Using these three micrometer positions the holder can be raised and lowered parallel to the polishing mat, helping ensure the sample can be milled from orthogonal directions. It is important not to place any extra force down on the polishing holder beyond its own weight as this will break the sample off the aluminum block. In practice leveling the polishing tripod and sample by eye was sufficient to obtain close to  $90^\circ$  corners on the sample. The wax beneath the sample leaves it at some unknown but small angle and prevents a more precise corner being polished even with a completely level tripod.

Coarse polishing is done with a  $3\ \mu\text{m}$  polishing mat rotating at  $\sim 3\ \text{Hz}$ . This mat is used to polish the sample side to a flat face with a smooth edge without chips in it. The sample can be inspected under an optical microscope to see the polishing progress. The polished region is obvious from its flatness, and polishing was generally continued until the entire polished face was transparent with no chips along the top face edge. Water is left flowing over the mat during polishing

to remove polishing debris, and should be a high enough rate that the entire mat stays wet while spinning. It helps to direct the flow as close as possible to the sample during polishing to remove polished material. A 0.5  $\mu\text{m}$  mat is used to finish polishing the surface to an optically flat surface such that the GGG substrate appears completely transparent.

When the polishing is stopped, water remains on the sample from its surface tension. It can be observed evaporating through an optical microscope, and eventually leaving a white residue on the surface which may be a combination of polished sample material and wax. SEM images of it show scattered particulate. This debris does not come off easily in an acetone/IPA clean, and appears strongly bonded to the surface. It caused considerable difficulties during milling, and was difficult to remove completely once in place. The samples come covered in an Al protective layer and etching this off does not completely remove the contaminants; instead they appear to fall onto the surface after Al etching and remain there. The contamination is usually bad enough that clean regions large enough for a cantilever structure are hard to find. If the Al is left on the sample during milling to be etched off afterwards the FIB beam, even only on the imaging currents, causes changes in the Al which prevent its complete removal. The Al must be removed before milling, but can be left on during polishing. To reduce the contamination a large water flow rate is used to sweep contaminants away during polishing, and residue is reduced after polishing finishes by lifting the polishing setup off the mat such that the sample is held there for  $\sim 1$  minute in the stream of running water to remove the contaminants remaining on the sample.

5. After polishing, the Al mounting block with sample is removed and soaked in acetone to remove the wax. The procedure here that produces the best samples is still unclear. It appears that multiple soaks and rinses with fresh acetone helps the final surface quality, as does rinsing with fresh acetone and IPA before the

sample is allowed to dry. Once the wax and photoresist has been completely dissolved it should be rinsed again with an acetone spray bottle, then several times with IPA, and carefully blown dry with compressed air. This can leave a well polished side surface and a clean top face with the Al protective layer still on. It may help to heat the acetone during cleaning, or use an ultrasound bath although this will require a holding jig for the sample.

6. The sample is cleaned again with acetone and IPA prior to Al etching. The sample is held with tweezers and gently swept back and forth through the aluminum etchant to keep the surface clean. The  $\sim 300$  nm Al layer etches off in approximately 2 minutes, though this time varies widely with etching details. Following etching several water rinses are quickly performed to remove all of the remaining etchant. The sample is gently blow dried. This process can give a polished clean LuIG sample with very little contamination.

The amount of contamination on polished samples is reduced by these steps, but still varies enough that not all samples are clean enough for milling.

### **2.4.3 Focused Ion Beam Milling Complications**

#### **FIB Beam Shape**

The Focused Ion Beam microscope suffers from the same aberrations as an optical microscope, like astigmatism and spherical aberration. These can be mostly corrected in the FIB alignment and are small enough when aligned correctly that they do not matter for any of the structures we milled. The FIB beam has a gaussian profile that results in material under the center of the beam being exposed to the full beam dose, while the beam tail still mills material slightly out of the expected region. A schematic of this is shown in Figure 2.5. True vertical milled edges cannot be produced, although the tapering can be reduced somewhat by milling at a small back tilt angle, typically around one degree,

to the expected wall profile. Straighter edges can also be produced by coarsely milling a structure and then fine polishing with a smaller probe which also helps reduce re-deposition effects.

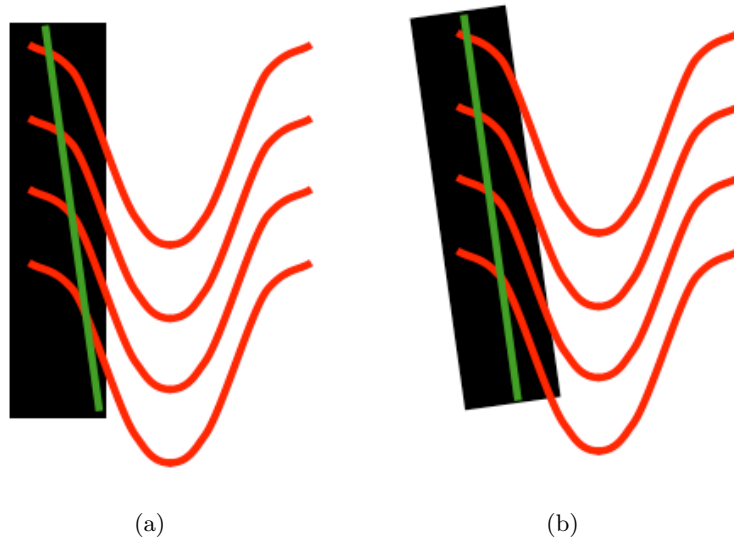


Figure 2.5: The gaussian profile of the FIB beam results in the beam tails milling the sample edge. This schematic exaggerates the effect and back tilt. (a) The tail milling accumulates on the sample side wall, producing a slope in it shown by the green line. (b) A more vertical side wall can be milled by using a small back tilt to the sample. This back tilt causes the beam to mill the base of a structure more than the top, counteracting the effect of the tails milling the top more than the bottom, and producing a straighter side wall.

## Sample Mounting

Focused Ion Beam milling of LuIG cantilevers is complicated by the need to mill from two angles  $90^\circ$  apart. To do this the LuIG sample is mounted on a SEM stub at  $45^\circ$  from the horizontal which allows both the SEM and FIB columns clear access to the sample face to be milled without extreme or impossible stage tilts (see Figure 2.6.) Similar stubs can also be used for mounting samples during optical measurements, although the stubs are currently too tall for mounting on the translation stage for optical measurements, and the high NA objectives used



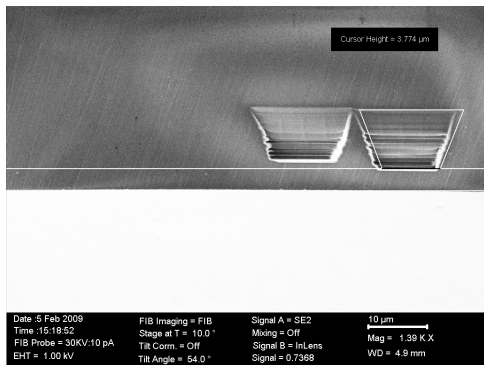
the paint off the milled surface and off the bottom of the sample so that a clear section through the sample bulk is available for MO measurements. Ultimately, only silver paint is being used to mount samples.

### **Charging**

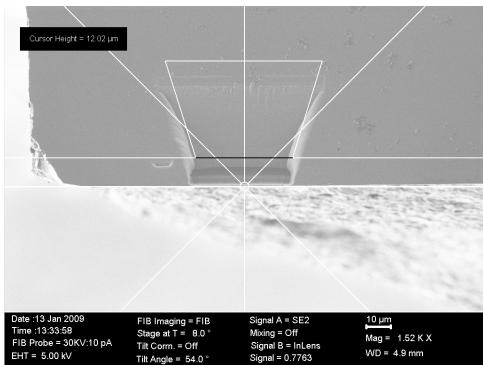
Charging was a problem in milling which has been solved with proper grounding. Charging can cause drifting of the sample during milling or during a SEM scan (Figure 2.7(a)), sudden shifts in the sample position from the designed mill position (Figure 2.7(b) and Figure 2.7(c)), or crack type erosion of the sample near milled areas possibly caused by the sudden release of built up charge (Figure 2.7(d).) This erosion only happened while using the 13 nA probe, so currents larger than 6.5 nA are no longer used on LuIG. We have also observed contaminants and even a cracked sample corner suddenly disappearing from the sample as they charged. Grounding an edge of the top face of a bare LuIG sample isnt sufficient, since the charge cannot escape from a milled area to the grounded region unless they are close together. The Al layer left on the LuIG surface or a 5 nm deposited carbon layer are enough grounding to prevent charging problems during milling though the Al layer is usually removed. Even though only the top face is grounded and the edge face is not, we have not milled more than approximately 30  $\mu\text{m}$  away from the grounded top face and have not seen milling problems with this method. No change in the magnetic or optical properties was found from the 5 nm carbon layer.

### **Redeposition**

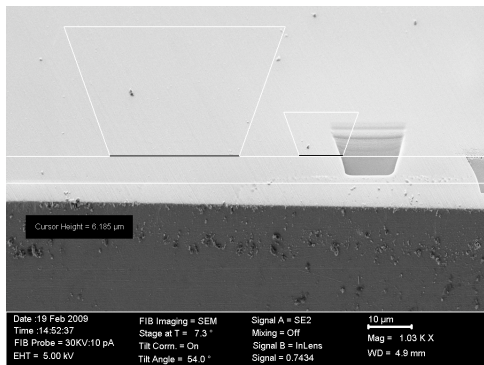
Redeposition is a significant challenge during milling. Material ejected from the sample during sputtering by Ga ions emerge with a variety of trajectories and energies. Not all of these allow the material to escape the region of the sample



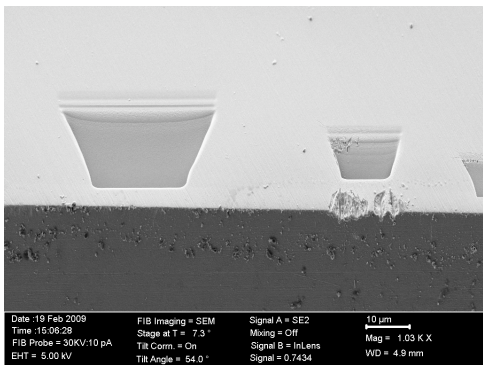
(a)



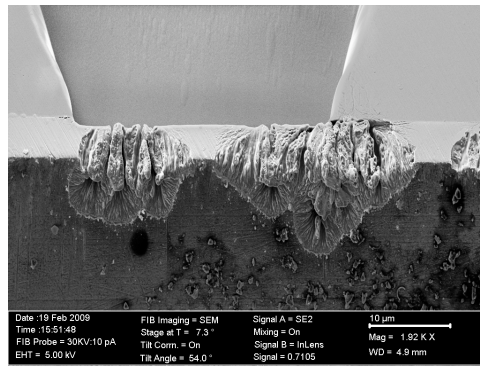
(b)



(c)



(d)



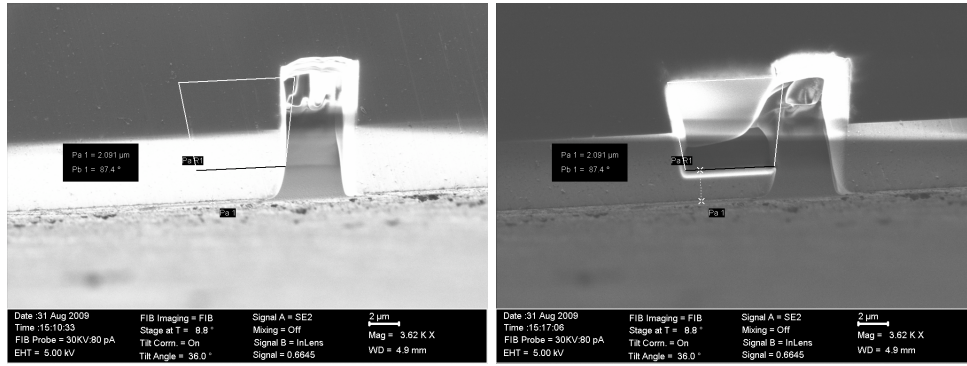
(e)

Figure 2.7: Possible problems during milling. (a) Drifting of the sample during milling, likely from charging. This is visible in the series of lines in the milled trench rather than the expected smooth surface. (b) A sudden shift in the sample position occurred between placing the designed pattern outline (white trapezoid) and the start of milling. The sample shifted approximately  $8 \mu\text{m}$  so that a  $4 \mu\text{m}$  thick cantilever was milled instead of the designed  $12 \mu\text{m}$ . (c) A sudden single shift after the start of milling, visible in the discontinuous face of the milled trapezoid. (d) Severe etching of some kind of the sample edge that occurred during milling. We speculate this is caused by a buildup of charge suddenly releasing, most likely leaving the area of milling and taking material with it. A similar process has been observed occasionally when small bits of contaminants on the surface suddenly disappear, although in that case the surface itself is not damaged. (e) Close up of the damage during milling. All the above milling problems stopped when proper grounding of the sample to the stage was used along with with a  $5 \text{ nm}$  thick carbon layer sputtered on the surface.

into the chamber. Geometrical effects from structures like the side walls cause many of the sputtered atoms to redeposit in the region surrounding the milled area. [31] Different milling methods, for example a series of repeated fast mills compared to one slower mill with the same total ion flux would in theory give similar milled structures, but can be vastly different in practice. Redeposition means that structures must be milled from repeated patterns with successive mills required to produce flat surfaces. Figure 2.8 (a) shows a sample and the region to be milled outlined. There is an unseen undercut beneath the visible surface which we are trying to mill through to. Figure 2.8 (b) shows the same surface after milling. There is a mound of material along the top of the outlined region, which tapers off to the right by the previously milled trench where sputtered material was able to escape reducing redeposition here. Figure 2.8 (c) is after a few more mills over this redeposited mound and around the edges of the cantilever to remove a small amount of redeposited material there.

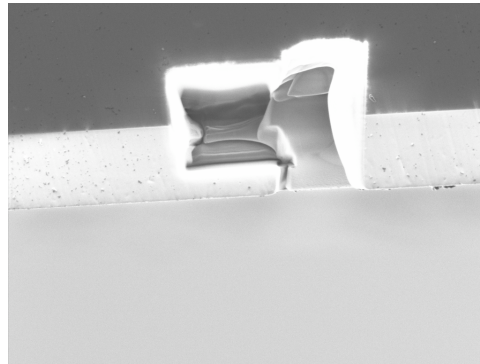
### **Milling Alignment**

The FIB must be aligned in several steps before milling to ensure the beam is the correct shape, has the expected current, and is in the expected position. These calibration procedures are similar to that for an SEM, and are performed by the FIB operator. In most milling, imaging with the FIB is used to align the milled pattern with the desired location on the surface, the advantage being the SEM column can be left slightly miss-aligned from the FIB column and used only for taking images and inspection, shortening the alignment procedure. The disadvantage of this is that there is Ga ion damage from the FIB imaging that occurs over the entire imaged area, not just in the area that is to be milled. This ion damage is small, but implantation may affect the final structure's magnetism and the slight milling occurring may be noticeable on small enough devices. The



(a)

(b)



(c)

Figure 2.8: (a) The expected area to be milled of the side of the sample is outlined. The sample has been previously milled from the top to produce a back trench (b) shows the same surface after milling. Material that is unable to escape redeposits producing the bright mound, which tapers off to the right where material can escape into the side trench (c) After milling several rectangles over the redeposited material and polishing the under side of the cantilever. We can now see through to the undercut region below, although this isn't obvious from image.

FIB imaging is enough to prevent etching of the Al layer where it has been imaged.

Inaccuracies in the mounting stubs and silver paint frequently leave the samples at some other angle other than the expected  $45^\circ$ . While the mechanical polishing leaves the side face flat, it is usually a few degrees off from the expected  $90^\circ$  corner to the top face. This misalignment can be significant, such as when we attempt to mill a rectangular cantilever from the edge and end up with a wedge. The samples faces are aligned to the FIB beam by imaging looking down the edge of a face that is  $\sim 90^\circ$  to the imaging column. The face is rotated until it just disappears from view, at which point the imaging beam is parallel to it. A quick mill line can be made extending along the top and off the edge. It should barely be visible, or not at all, on a properly aligned sample face.

### **Beam Currents**

A variety of beam currents are used during milling. Larger beam currents mill faster with lower resolution and leave steep side walls. A 6.5 nA or 3 nA beam was used for most rough milling, with small probes, usually 700 pA and then 80 pA, used for small structures or fine milling. Probes larger than 6.5 nA caused charging problems even with grounding and shouldn't be used.

### **Milling Flat faces**

In theory milling over a surface should act like an isotropic etch where the surface profile is carried down into the sample by milling. Several effects prevent this from happening. The largest effect, redeposition of material, has already been discussed. Redeposition changes the milling rates across a surface as in some areas the ion beam must mill through more redeposited material than others in order to mill into new material. Contaminants on the surface change the initial surface

profile and thus the final milled profile in the sample. If the contaminants are of a different material than the sample, their different mill rates also affect the final sample profile. Additional effects are sometimes seen where a small point appears to shield or redirect material below from the beam, producing cone structures in the milled region. Once a cone structure is produced the slanted slides may further encourage its growth by redirecting some of the milling ions, reducing the sputtering rate. Despite these effects, shallow flat faces may be milled from a flat initial face provided they have a shallow aspect ratio allowing most of the milled material to escape, and do not have contaminants on their surface to influence milling.

All of these effects mean that milling can not be used to produce a flat face normal to the mill direction; they can only be produced through by milling a sidewall. This is a major constraint on designing structures.

## **2.5 Producing a Cantilever: Procedure**

The procedures for creating a cantilever, bridge, or paddle structure are similar and differ mainly in the milling order. Two types of cantilevers were milled; one type pointing off the sample edge, one type lying parallel to the sample edge. Those pointing off the edge are the easiest to mill, but cannot be created with the flat surface beneath them needed to produce an interferometric cavity for measuring mechanical motion. Cantilevers lying parallel to the edge are more time consuming to mill but allow mechanical measurements. A doubly-clamped beam and paddle structure are variants of the parallel cantilever milling procedure.

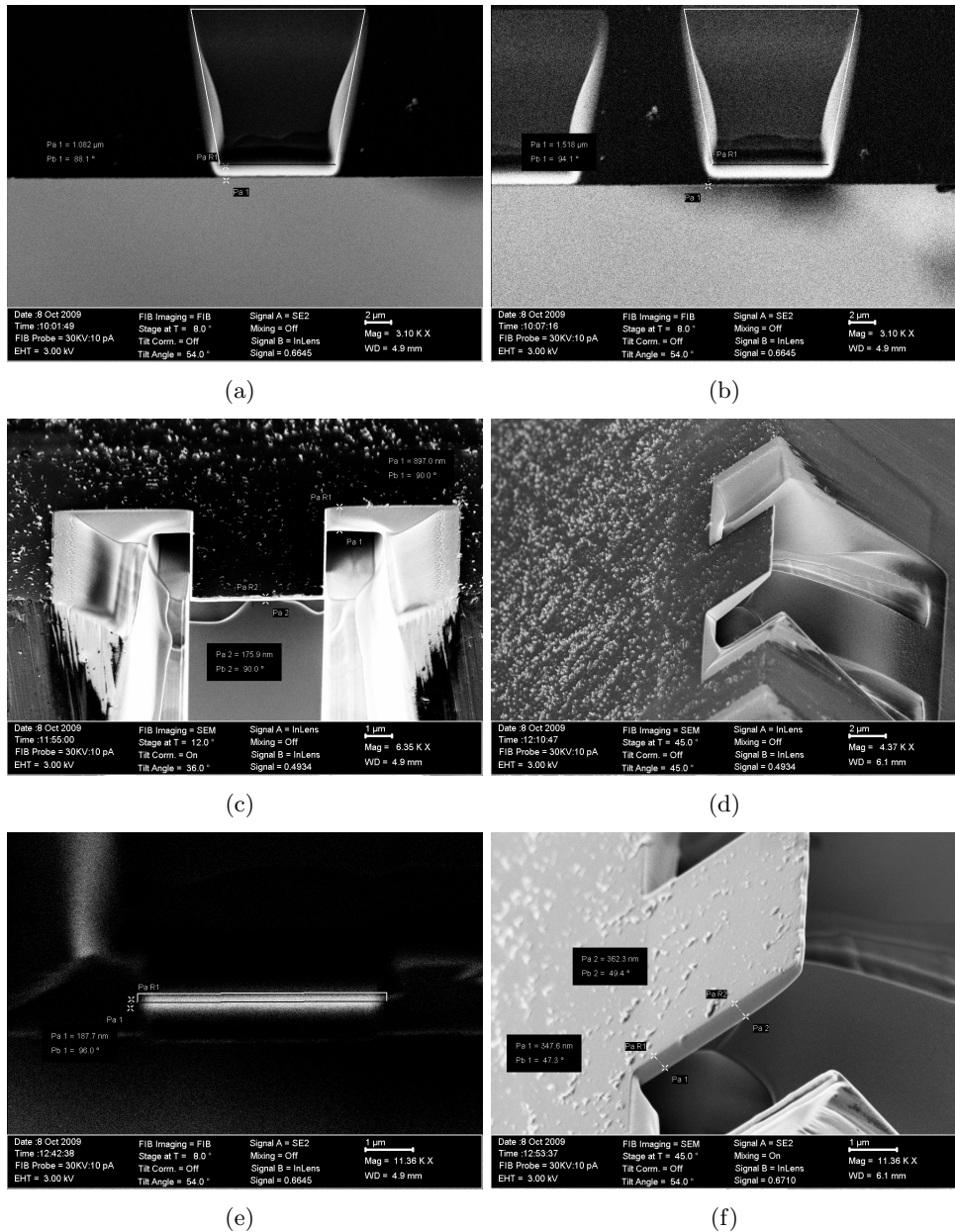


Figure 2.9: The main steps in milling a cantilever. (a) An undercut is milled from the side with a 3 nA probe. It is 4  $\mu\text{m}$  deep, 7  $\mu\text{m}$  long, and 9  $\mu\text{m}$  wide, giving a 30° clearance angle for the beam. A 1  $\mu\text{m}$  thick layer is left for fine milling of the cantilever. (b) Successive undercuts for separate cantilevers are made one after another to save time. (c) The sample is rotated to allow milling from directly above the top face. This SEM image shows the cantilever after the trapezoidal side mills are completed which allow viewing access to the cantilever profile. (d) shows how the initial 3 nA mill left a wedge shaped cantilever that requires thinning. (e) The sample is rotated again to allow the FIB access to the sample side face. This shows a fib image of the cantilever thickness between thinning mills and the difficulty in measuring the cantilever thickness from this view. The tails of the beam round the face such that it's hard to tell where the cantilever begins and ends. (f) shows the successfully thinned cantilever.

### 2.5.1 Milling a Cantilever

A cantilever that is end on to the sample edge is the simplest structure to mill. An undercut is first made in the sample edge face (See Figure 2.9.) This is usually a sloped trapezoid that is deep and long enough to allow the laser to clear the sample edge during optical measurements. Trapezoids allow material to easily escape the milled area, while taking half the time of a rectangle. As well, milling a rectangle in one pass frequently results in a similar shape to a trapezoid due to the heavy redeposition against the vertical wall being first milled. Too small an undercut and the laser beam will not be able to pass through the cantilever without hitting the sample underneath (Figure 2.10 (a).) A trapezoid or rectangular milled area both allow the beam to pass through (Figures 2.10 (b) and (c).) Typically a 3 nA probe will be used for the initial rough mill. Cantilevers thinner than a micron are not cut on this initial mill, instead being left to be thinned with smaller probes. The relatively large beam tail of the 3 nA probe rounds the edges of the milled areas, and for cantilevers thinner than a micron this can obscure the actual cantilever thickness. Cantilever thinning continues in several mill steps to reduce redeposition, each step shaving off a few 100 nm of material. 700 pA probes are used to thin the cantilever to around 300 nm, after which an 80 pA probe has been used to thin cantilevers to a minimum of approximately 150 nm. Any thinner and the cantilever begins to warp, and a new milling method would be needed. As the cantilever thins below a micron the aspect ratio of the cantilever and accurate back tilt of the sample become increasingly important. For thick cantilevers, a 100 nm variation in thickness across a 5  $\mu\text{m}$  cantilever length is not as significant as for a 400 nm thick cantilever. After the main undercut and some polishing has been completed, the sample is rotated and milled from the top surface in two parallel trapezoids to give the cantilever its sides. The trapezoid shaped side cut also allows viewing

of the edge of the cantilever which is necessary for thickness measurements and fine polishing.

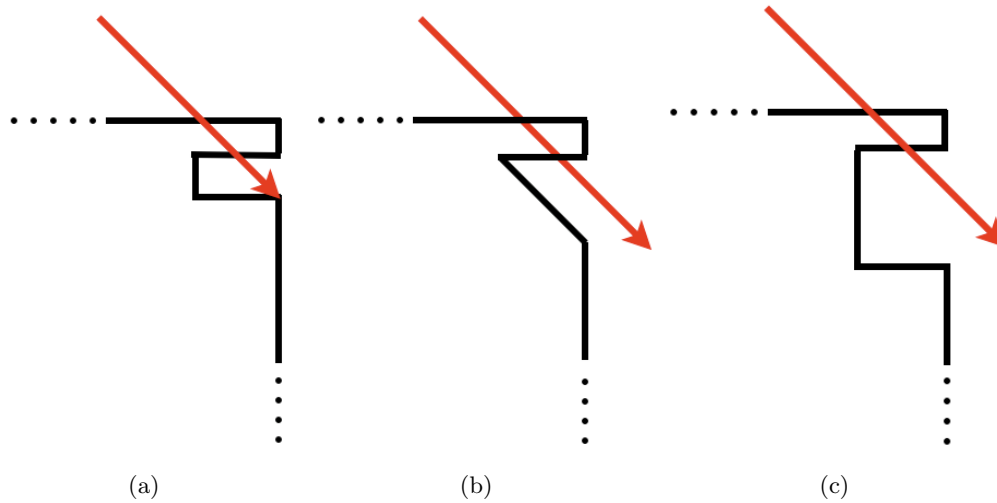


Figure 2.10: Too small an undercut as in (a) prevents optical access through the cantilever. (b) A trapezoidal undercut is simplest, providing optical access and low redeposition on the cantilever because the mill finishes flush with the bottom of the trapezoid. It also requires few polishing mills since redeposition on the sloped surface is unimportant. (c) Takes the longest to mill, requiring repeated trapezoidal mills back to back to reduce redeposition and give cantilever faces on both the cantilever and face below. This geometry allows optical access on an angle, or from directly above when a second reflecting face is needed to make a interferometric cavity for displacement measurements.

## 2.5.2 Cantilever Thickness Measurements

Measurements of the thickness variation along the cantilever length can be used to calculate the necessary back tilt required to thin the cantilever. Because the sample tilts in two directions in some SEM images, the measured lengths and thicknesses do not correspond to the actual sample lengths and thicknesses. The method of finding the correct device lengths from SEM images is described in Appendix A.1

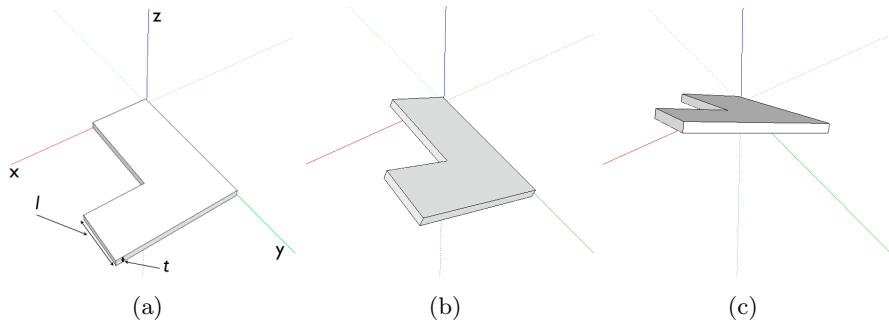
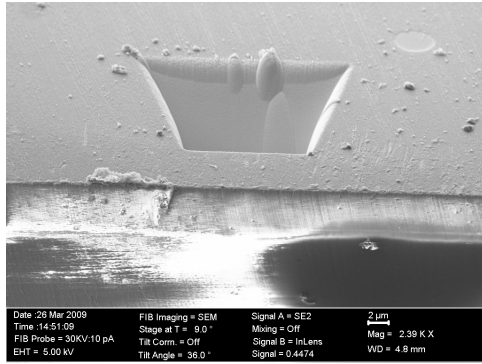


Figure 2.11: (a) shows an unrotated mock cantilever structure, with thickness  $t$  in the  $\hat{z}$  (blue axis) direction and length  $l$  in the  $\hat{y}$  (green axis) direction. The cantilever in (b) is rotated around the  $\hat{y}$  axis, corresponding to  $R_y$ . (c) Shows the rotation around the x axis (red axis), corresponding to  $R_x$  applied after  $R_y$ .

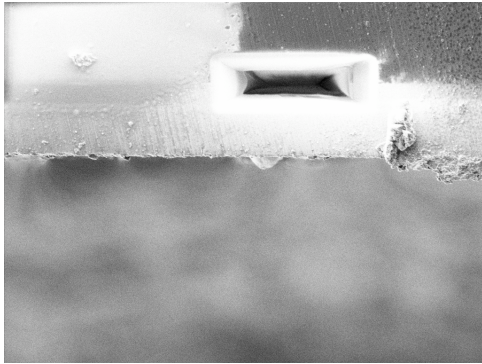
### 2.5.3 Milling a Doubly-Clamped Beam or Paddle Structure

The procedure for these structures is similar to that of straight cantilever, but requires a back trench milled from the LuIG top surface before any side milling. For paddle or cantilever parallel to the sample edge a back trench is milled from the top face of the sample with a 3nA probe, as in Figure 2.12(a). This back cut allows redeposited material to escape when the structure is later undercut from the side, as in Figure 2.12(b). Figure 2.12(b) shows the first cut from the side of the sample. This rectangle is produced by milling with four overlapping rectangles, each set to finish at a different edge and to mill for 1/4 of the final depth required. Redeposition effects can be seen in this image in the pillowy indistinct shapes billowing out from the edges of the rectangle. This same redeposition will require the depth the FIB is set to mill to be greater than the milled depth obtained. 2.12(c) shows the same rectangle after additional milling of the sides within it to reduce the redeposition. The end result of this is shown in Figure 2.12(d). The ion beam has passed through the undercut and continued to mill on the far edge of the original backup, which can be seen by contrasting this image with 2.12(a). Figure 2.12(e) shows score marks across the top of the

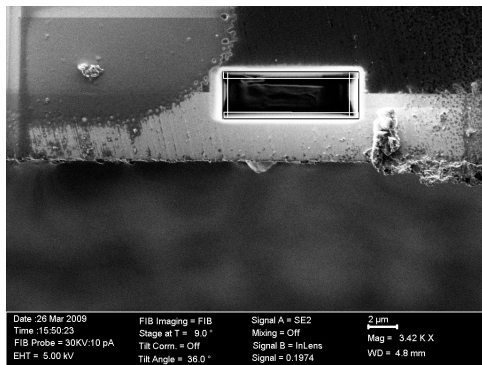
cantilever left from when brief lines were milled as markers from the side face. A slight misalignment of the sample with respect to the beam meant that some of the beam touched the sample edge as it passed by. These lines were milled from a perspective like that in 2.12(c). These markers are used to set up the 4 rectangles that were milled in Figure 2.12(f) to create the paddle structure. 2.12(g) shows the completed paddle structure along with a flat undercut face to act as the mirror for interferometric measurements required for the paddle's displacement.



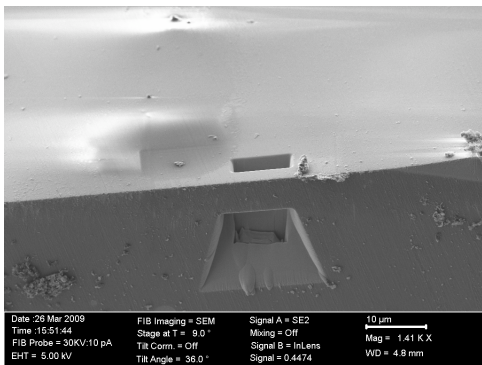
(a)



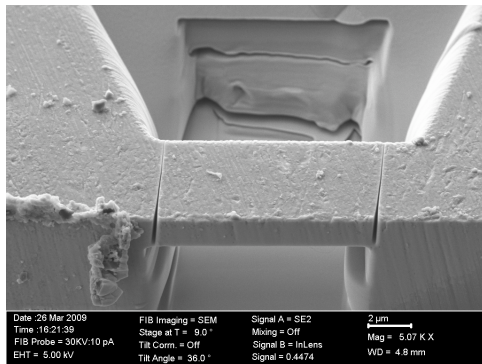
(b)



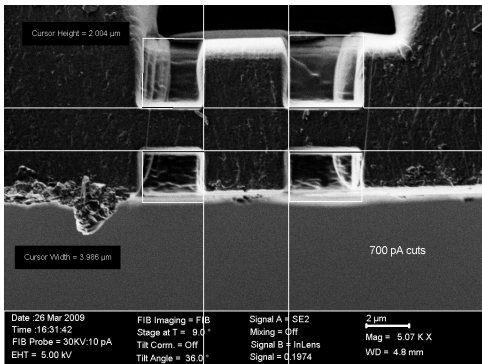
(c)



(d)



(e)



(f)

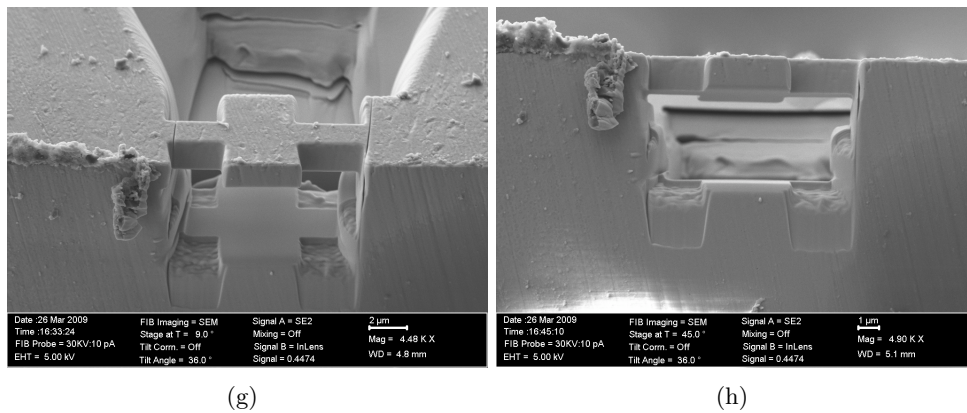


Figure 2.12: (a) Back trench milled from top sample surface with a 3 nA probe. This allows milled material to escape during undercutting. (b) The undercut is milled with 4 overlapping rectangles, each set to finish at a different edge and to mill for 1/4 of the final depth required. Milling may have to be done for much longer than the expected depth as significant redeposition slows milling. The mill time rises exponentially as the undercut region becomes smaller. The pillowy edges are redeposited material. (c) The same undercut after extensive polishing of the side faces to remove this redeposited material. (d) The undercut and back trench. (e) The completed doubly-clamped beam. (f) 4 squares cut out by the visible outlines using a 3 nA probe to create a paddle structure. (g) The completed torsion paddle beam. (f) The paddle structure showing the parallel faces creating an interferometric cavity.

## Chapter 3

# Experimental Setups

*This chapter discusses the experimental setups in detail and the method of taking hysteresis loops and FMR plots.*

### 3.1 Hysteresis Loop Measurements

The experiment for acquiring hysteresis loops and ferromagnetic resonance measurements has 4 main components, shown in Figure 3.1 and Figure 3.2: the optical setup, mechanical stage, moveable magnet assembly, and Hall probe, while the FMR measurements add a fifth, the dither field. The optical setup consists of the laser and associated optics to bring polarized light to and from the sample, and two photodiodes with a differential amplifier to measure the Faraday signal. The mechanical stage is a piezoelectric controlled stage on which the focusing optical objective is mounted and which allows precise alignment of the laser beam onto a structure. The motorized rail allows the permanent magnet to be moved, varying the applied magnetic field strength and direction. The dither field is a small coil that allows a fast electrical pulse to generate a transient magnetic field over a particular structure in the sample. The torque on the magnetization from this field causes it to precess out of alignment with the applied field. The

experiment was designed so that eventual hysteresis loops, FMR measurements, and mechanical actuation of a cantilever may all be studied together without alteration of a setup or movement of the sample.

### 3.1.1 Optical setup

A 632.8 nm wavelength HeNe laser (05-LHP-141 by Melles Griot) was used to take hysteresis loops. This wavelength was chosen because LuIG is quite transparent at that wavelength, while still giving a fairly strong Faraday effect, and for the ease of using the HeNe laser. The HeNe output is close to linearly polarized light at an arbitrary angle. A half-wave plate is used to rotate the HeNe polarization into the desired orientation, after which a Glan-Thompson polarizer accurately selects only one polarization state from the partially mixed laser output polarization, with the second component being absorbed. The Glan-Thompson polarizer can be used to set the polarization orientation and the half-wave plate varied to set the power out of the Glan-Thompson. The beam is expanded 5X, and then passed through an aspheric lens (C240TME from Thor Labs, 0.5 NA f=8.00 mm) for focusing through the sample. This lens was chosen as it had a fairly large aperture and a reasonable numerical aperture (NA). A larger NA would be useful especially for resolving smaller cantilevers however their short focal lengths cause problems with the sample mounting. Ideally a long working distance objective with a high NA should be used.

A second aspheric lens collects and re-collimates the transmitted beam, passing it through a quarter-wave plate to a second Glan-Thompson prism. The beam is polarized linearly with some ellipticity after emerging from the sample. The Glan-Thompson splits the beam into orthogonal polarization components with intensities that result from the angle of the incoming polarization and the Glan-Thompson's easy axis. Each component is measured by a photodiode (UDT-PIN

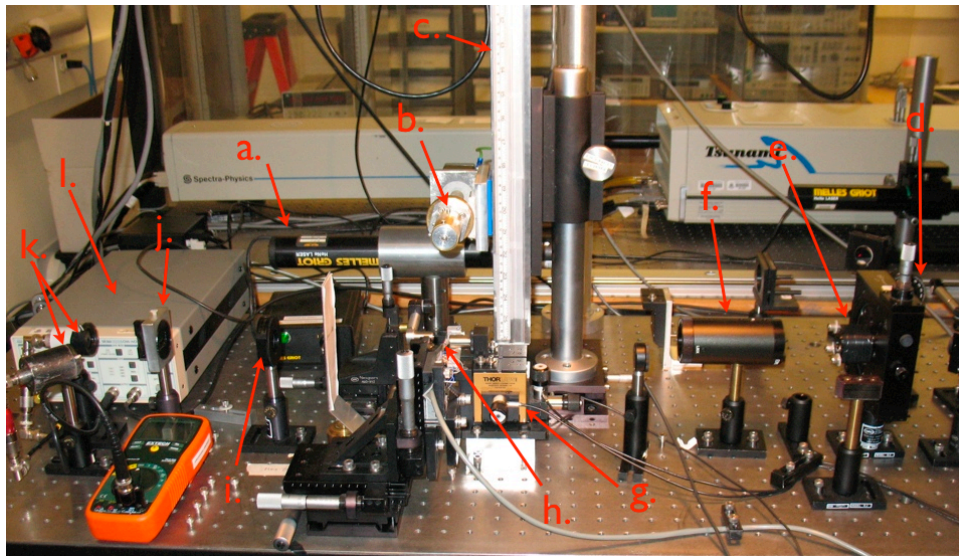


Figure 3.1: The experimental setup for measuring a hysteresis loop. (a) HeNe. (b) Rotating magnet attached to motor on the rail. (c) The rail for moving the rotating magnet. The drive motor is unseen above this picture. (d) half-wave plate (almost hidden). (e) Glan-Thompson polarizer. (f) Beam expander. (g) Piezoelectric stage. (h) Focusing objective, sample, Hall probe, and collimating objective. (i) quarter-wave plate. (j) Glan-Thompson prism. (k) Photodiodes. (l) Pre-amplifier. The corresponding schematic is in Figure 3.2.

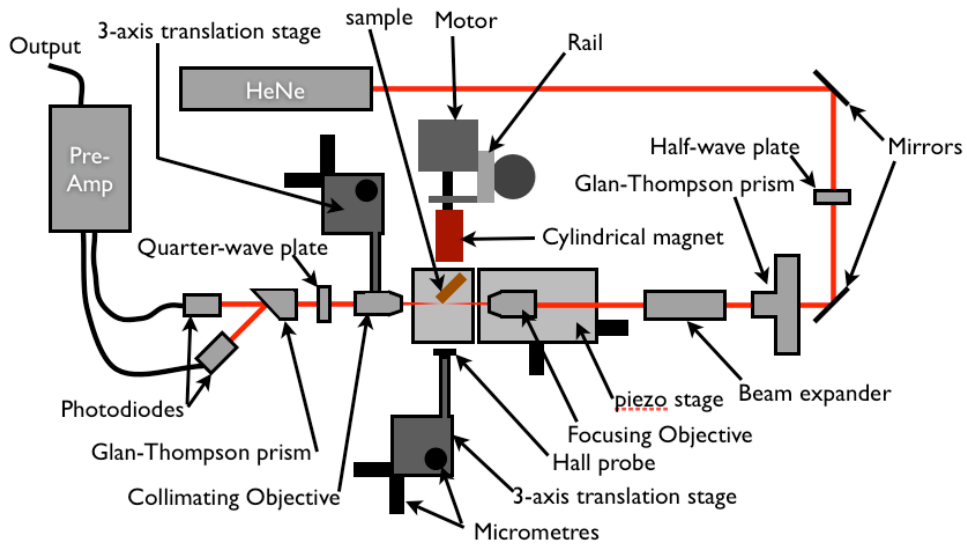


Figure 3.2: The schematic for the hysteresis loop experiment and Image 3.1 is shown. The cylindrical magnet and hall probe are shown out of their usual positions for schematic clarity. The cylindrical magnet which produces the applied field is usually located directly above the sample, while the hall probe is moved forward towards the sample, and next to the beam, for field measurements. The sample is shown here with the beam passing through one sample corner, with the sample mounted parallel to the 3-axis stage. In a more common orientation the sample is mounted vertically, passing through an corner at the top rather than side as shown here. The Pre-Amp output is the difference in intensity between the two orthogonal polarization components of the laser in the two photodiodes.

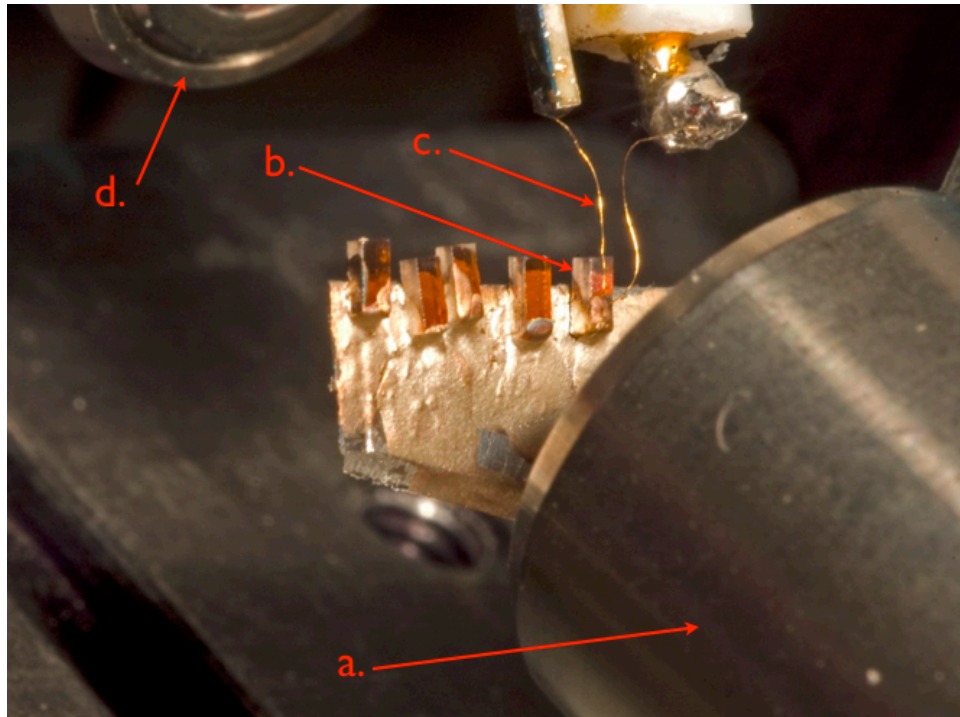


Figure 3.3: Close up of samples mounted at  $45^\circ$  for FMR measurements. This is the same setup as would be used for hysteresis measurements, but without the dither coil. (a) Focusing objective. (b) Sample mounted with silver paint on a holder which is mounted out of sight behind the focusing objective. (c) Dither coil. This coil is closer to the camera than the sample and so appears larger than it is. (d) The collimating objective.

10DP 274-1). Their outputs are passed into a pre-amp and subtracted, giving a difference signal that is proportional to rotations of the beams polarization. The setup is most sensitive when the power to the photodiodes is balanced. At this point a small change in polarization through the Glan-Thompson produces the largest change in power in a photodiode, and a large gain can be used on the pre-amp.

Ideally the quarter-wave plate would not be used, and the Glan-Thompson rotated so that each output beam is of equal intensities and giving maximum sensitivity to polarization changes. This is difficult since one of the two output beams may have to be directed upwards at an angle where it is difficult to place a photodiode, and the photodiode position would have to be frequently adjusted. The quarter-wave plate is used to introduce some ellipticity into the beam, balancing the two orthogonal output beams without need to rotate the Glan-Thompson.

The photodiodes used generate a current, and saturate at approximately 300 mV measured across a load resistor. The sensitivity of the photodiode depends on the load resistor, with larger resistances generating a larger voltage response for a smaller incident power on the photodiode. The load resistors were generally around 1 to 5 k $\Omega$ 's. The differential amplifier had a typical gain of 20.

### **3.1.2 Faraday Rotation Calibration**

The intensity change measured by the differential amplifier and photodiodes results from the actual Faraday rotation of the beam as well as the amplifier gain, magnetic field, sample, and Glan-Thompson prism and quarter-wave plate position. The intensity measured to an angle can be calibrated by rotating the initial Glan-Thompson polarizer by a few degrees to vary the incoming polarization through the sample. Typically a total rotation of  $\pm 4^\circ$  was used, and the

corresponding intensity changes measured which was found to be always linear for the small angles used. A fit to the measured power as a function of incoming polarization relation gives a linear radians per volt formula that is used to calibrate the measured faraday rotation intensity to an angle.

### **3.1.3 Hall probe**

The Hall probe used was a 2SA-10G-SO 2 axis linear IC from GMW associates. It operated linearly from about -600 to 600 gauss, saturating in stronger fields. This Hall probe output a voltage proportional to the field which was measured by the DAQ card and Labview program. Its output was calibrated using a previously calibrated 3 axis Hall probe. The Hall probe was mounted on a 3 axis translation stage so that it could be easily moved in and out when the sample was changed.

### **3.1.4 Focusing Procedure**

The complete procedure for aligning and then focusing the beam onto the sample is lengthy, and rarely needs to be done. Instead, once the beam and stage are aligned new samples can be quickly mounted and aligned without moving any of the optics save for the collimating objective which is on a 3 axis translation stage. The sample itself is held fixed relative to the optics table, with the objective lens moved on the piezoelectric stage.

Aligning the setup starts with aligning all optics up to the piezoelectric stage. The beam emerging from the first Glan-Thompson polarizer should be aligned to pass level with and in line with the piezoelectric stage top plate. This can be done by removing the sample, objective lenses, and beam expander, and checking that the beam remains level across the table with a moveable beam stop. It helps to place the focusing objective in backwards to make sure the beam hits the center of the lens. This ensures that when the focusing objective is placed in position

correctly, the beam will pass through cleanly. The second Glan-Thompson prism after the piezoelectric stage should be placed such that the beam enters it cleanly with no objective lenses, beam expander, or sample in place. Once the beam is passing level over the piezoelectric stage and into the focusing objective, the beam expander can be placed in line and adjusted so that it does not change the beam direction, but only the spot size. This should be checked with and without the focusing objective in place. With the sample still removed, the collimating lens can be adjusted to re-collimate the beam into the second Glan-Thompson, which if the alignment has been done right will not need to be adjusted. At this point the sample can be placed at the focal point between the focusing and collimating objectives. This is easiest to see by backing the focusing objective away from the sample with the coarse approach actuator on the piezoelectric stage, and moving the collimating objective out of the beam line with its 3 axis stage. A card can be placed near where the collimating lens was, and an expanded image of the sample is visible, Figure 3.4. It is easy to see the transparent regions of the sample, and the diffraction patterns formed when the beam hits a milled sample region along the sample edge. The diffraction pattern is best seen on an only moderately expanded image. When the diffraction patterns are found, the beam is focused with the objective lens into a spot on the diffraction pattern. The ideal focus is reached near when the interference patterns invert as the focal point moves past the structures. At this point the collimating lens is reinserted into the beam line.

A Labview program has been written which records the changes in intensity from the pre-amp as the focus spot is raster scanned over the sample surface with the piezoelectric stage. The best image is obtained by setting the preamp to measure one photodiode's power, not subtract it. This gives an image of the surface with a few hundred nanometers resolution which is used to align the

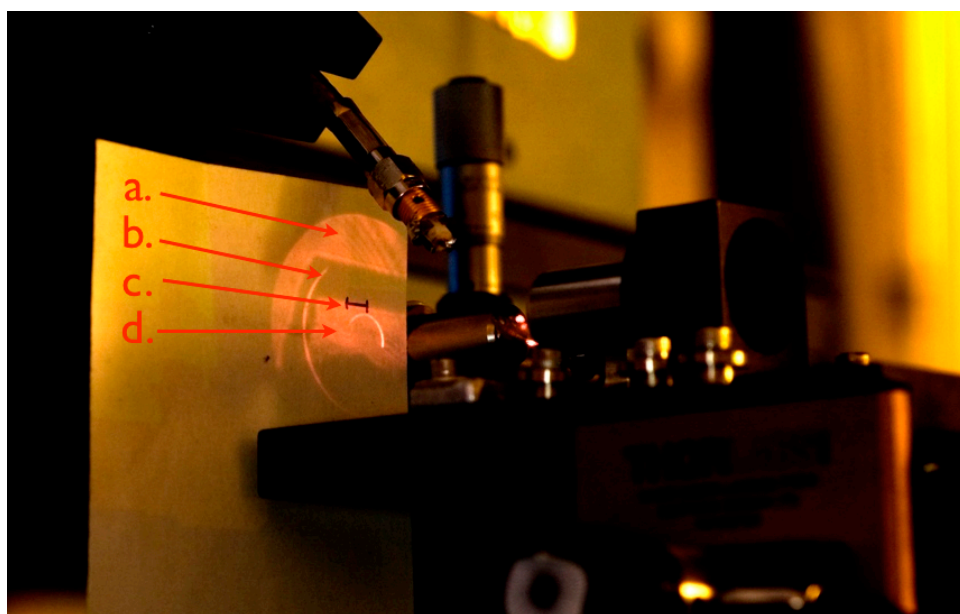


Figure 3.4: The expand image is visible on the white card. (a) the beam passing above the sample onto the card. (b) Dark region at the edge of the sample where the prism effect of the side wall prevents light from passing through. (c) Transparent bulk region of the sample. (d) Alignment mark, 5 mm wide.

beam spot to an individual structure. A typical raster scan image of a cantilever is shown in Figure 3.5.

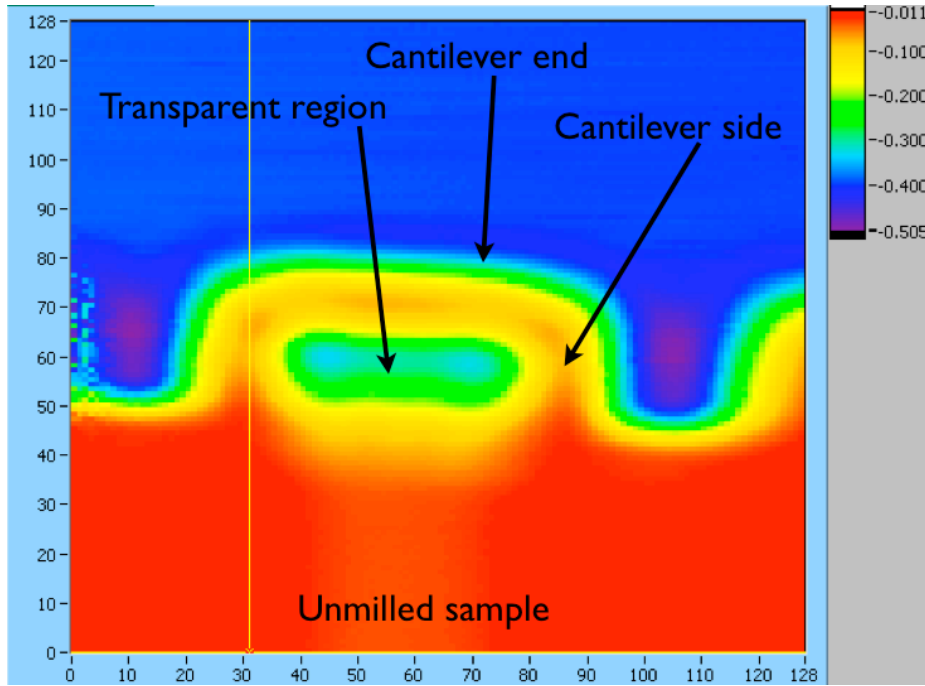


Figure 3.5: A raster scan image of a  $5\ \mu\text{m}$  by  $5\ \mu\text{m}$  cantilever mounted at  $45^\circ$ . The cantilever has a region around the edge of it that is opaque, with a transparent region in the centre. In the center of the cantilever the beam passes through two parallel faces. On the cantilever side edges the beam is clipped by the edge and does not transmit cleanly. At the top edge the beam passes into the cantilever, but then encounters the front face of the cantilever not the bottom, where the effect of a prism redirects the beam. The cantilever is foreshortened from it being slanted away from the viewer. The pixelation on the left side middle of the image is caused by an insufficient delay between the last data point on a line and the first data point on the next raster scan line. If this delay is too short the program begins ramping the piezoelectric voltages and taking a new line of data points before the stage has had time to physically move to the start position of the new line. The pixelation can be removed by increasing the delay between taking raster scan lines.

The piezoelectric stage has some creep, so it can only approximately be assumed that a given location in the image corresponds to the position given by applying offset voltages to the piezoelectric actuators to move the beam to the expected position in the image. Instead, the raw power through a cantilever (not the difference between photodiodes) is watched while the offset voltages of

the amplifier supplying the piezoelectric actuators are varied. The power can be seen to go through a local maximum in the cantilever, and this is the point used to obtain hysteresis loops. Comparisons of hysteresis loops through cantilevers confirm that this position gives the largest signal.

### 3.1.5 Magnet And Rail System

The magnet rail system is mounted vertically next to the sample stage on a 2 axis stage. The stage allows the magnet attached to the rail to be positioned precisely over the sample. The magnet movement is controlled with two stepper motors; one controlling the height above the sample, and the other motor rotating the magnet on the rail at a given height. This allows the magnitude and direction of the applied field to be controlled. Both motors and controllers were number CSK264-AT from Orientalmotor. A Power-One model HN24-3.6-AG linear power supply runs the controllers and motors.

TTL levels (0V/low or 5V/high) into the controller from a NI-USB-6229 DAQ card control the motor. This includes: step direction, (CCW or CW,) whether current is supplied to the motor windings or not, and cause the motor to advance a step in the given direction. Each step is a single TTL pulse. The TTL levels and pulses are easily generated from the digital logic outputs and controlled via software. While easy, software control through digital logic outputs is limited in pulse speed to one pulse every couple of ms which slows the motors significantly. As high rotation speeds are desirable to reduce noise and improve the number of averaged cycles in a reasonable period of time, we have used counter outputs rather than digital logic outputs and software to generate the motor pulses. This significantly complicated the Labview programming.

Using the DAQ counters to generate pulse trains to quickly advance the stepper motor a number of steps is complex. The DAQ card has a fixed clock which

is used to synchronize all output and input write/reads, and two counters which can generate high frequency pulses. These counters run continuously, and so to generate the finite pulse train needed to move the stepper motor a fixed number of steps one counter internally gates the second one to produce a finite pulse train. A problem is that the first gating counter outputs a pulse while stopping and starting the second counter, so that the two counters cannot be operated independently with each producing finite pulse trains.

Trying to control two motors, one from each counter, results in extra pulses being sent to the motor that is not being activated with the finite pulse train. The solution was to use a demultiplexing chip (MUX 4051BE) so that two motors can be controlled from one counter without unwanted steps. The DAQ counter output is input into the demultiplexer, and a TTL level from a DAQ DIO is used to control which motor the pulses are delivered to. While not a requirement to date, this does prevent using both motors simultaneously.

The counters are used by setting up their properties (pulse duration, number of pulses, etc) in a Labview task, and then starting that task. A task is the set of commands that will be executed by the DAQ card, such as output a pulse train of 400 pulses at 500 Hz. This would rotate the motor shaft  $360^\circ$ . Control of the counter is then passed to the DAQ card, which executes the entire task, before returning control to the Labview program. Read operations can be set up at the same time by preparing a buffer and syncing AI read operations to the pulse output clock. This allows a fixed number of AI data points for each pulse output (motor step.) This can be imagined as the clock ticking over, and for each tick a data point is read from the AI inputs, and an output sent to counter output. The number of data points input or output can be varied for each 'tick' of the clock.

There are a number of subtleties to using the buffered read/write to take

and average data. The commands to start the read and write tasks must be separate and sent from the Labview software. This introduces a slight delay between starting the write and read tasks, a delay that can vary and which probably depends on the CPU load when the Labview tasks are executed. If the pulse output tasks is started first, no data is recorded into the buffer for the first few pulse outputs. If the AI read task is first, the first data points will not correspond to movement of the motor. If multiple data runs are to be averaged, say for repeated revolutions of the motor, the varying offset between the start of data recording and of pulse outputs prevents a straightforward averaging by aligning successive data runs to the data point position. This is equivalent to having rows of data, but the data points in each column not necessarily being correlated to each other but with, for example, the data point in the fifth column of the first row should correspond to fourth column of the second row, and so forth. As the pulse outputs move the motor, not properly aligning the data for averaging results in averaging signals from different magnetic field strengths. Simply using the recorded magnetic field is also not accurate, especially for low fields, as the magnetic field noise can be greater than the difference in magnetic field between motor steps, and using the magnetic field requires a method of binning the data into magnetic field ranges such that it can be averaged.

To avoid this problem the DAQ card buffer size is calculated from the expected number of data points per counter pulse and the number of counter pulses to be output, and an additional constant number of data points added to account for the initial unknown delay between the start of counter pulses and AI data. A wire is placed from the counter output which runs to the stepper motor controller, into an AI. This channel is read along with magnetic field, photodiode intensity, etc. In this way a record of where in the recorded data a motor step took place is taken. The averaging in the Labview software then checks this record for the

first motor step in a given cycle and uses this to align successive average cycles. This is pictorially represented in Figure 3.6.

## 3.2 Ferromagnetic Resonance Measurements

### 3.2.1 Pump and Probe Technique

Ferromagnetic resonance is too fast for a single ring down to be directly measured. Instead we use a stroboscopic technique called pump-probe that uses a variable time difference between two stimuli to measure phenomena too fast for a continuous measurement. A stimulus pulse called the pump starts the system to be measured at some time  $t_o$ . A measurement pulse, called the probe, is made at some time later after some time delay  $\Delta t$ . By varying  $\Delta t$  the state of the system is sampled at various times, and with a reproducible response from the pump these individual measurements can be combined to give the response in time. The time resolution of the experiment is principally dependent on the time resolution of the delay between the pump and probe and the duration of the probe.

### 3.2.2 Dither Field

In our FMR measurements the pump is a small loop of wire (the dither coil) held close to the sample surface which generates a magnetic field into the surface, called the dither field. Several dither coils were made and discussed in the results section. Typically they are made with 30 gauge or smaller wire, a  $50 \Omega$  surface mount resistor mounted in series with the loop and a SMA connector soldered to it. Two pulse generators were used, their differences described in the Results section. These generate either a 10 V (Picosecond Pulse Labs model 4050) or 50 V (Picosecond Pulse Labs model 2000 turbo option) pulse creating a current

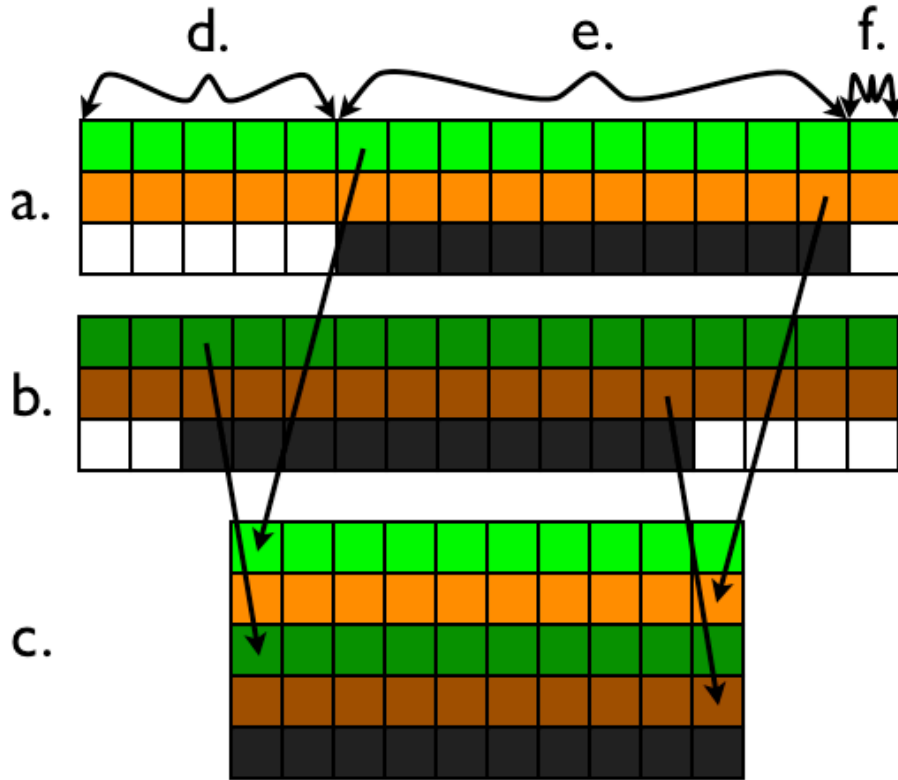


Figure 3.6: A pictorial representation of how the Labview program averages hysteresis loops. Each row is a DAQ AI recording a series of data points. Green squares are Faraday rotation measurements, orange Hall probe measurements, and white/black the motor rotation pulses output to the stepper motor. The AI and motor pulse outputs are synchronized together with the DAQ clock so that each column of data is correlated with each other. The motor takes exactly 400 steps to complete a revolution, and this was found to be completely repeatable and more reliable than the magnetic field in determining the magnets position. The 400 steps required for a rotation are used to correlate different rotations. In the motor rotation pulse row white represents the motor being stationary, and black corresponds to a pulse sent to the motor to advance it one step and recorded by the AI. (a) is the first hysteresis loop data run, (b) the second run, and (c) the properly aligned data arrays from which the data can be averaged in columns. To record data the Labview tasks are initialized to record an array of length given by the number of steps the motor will move (black, usually 400) plus some fixed extra buffer size (white). These tasks start recording the AI inputs for some length of time before the motor moves, (d) in (a). The motor then runs for a fixed length of steps ((e) in (a)) after which the remaining buffer records data with the motor stopped ((f) in (a)). This repeats for the second and subsequent data set (b) but with different initial and final buffer lengths. The Labview software detects the start of the motor rotation (start of black squares) and uses this and the number of steps the motor will move to truncate the data not corresponding to motor movement (white) to align the correct segments of each data for averaging (c.)

pulse across the  $50 \Omega$  resistor. This current pulse can be measured by a Tektronix CT6 current probe in line between the coil and pulse generator.

This brief current pulse creates a magnetic field normal to the sample surface, while the static field from the permanent magnet, held fixed, magnetizes the sample in-plane. As the magnetization precesses around the in-plane bias field, a component of the magnetization swings in and out of the sample surface plane and therefore along the laser propagation direction. This change in magnetization is measured via the Faraday effect in the same way as with the hysteresis loops.

### 3.2.3 Pulsed Laser

Instead of the CW HeNe laser used for hysteresis measurements, a mode locked Ti:sapphire laser is used. (Tsunami, by Spectra-Physics) This generates 790 nm optical pulses at a 80 MHz rep rate. The beam is passed through a Spectra-Physics model 3980 pulse picker which picks out pulses to split the beam into two of different rep rates, one a lower intensity 800kHz beam which is used for the FMR measurements.

### 3.2.4 RF Switch and Lock-in Technique

This method allows for lock-in measurements of the FMR signal at various pump-probe delays. An optical pulse traveling down the beam line from the pulse picker passes through a beam splitter which directs some of the power to a fast photodiode (DET210, ThorLabs). Voltage pulses generated by this photodiode are connected to an RF switch with two outputs (Minicircuits ZYSWA-2-50DR) that is toggled by a TTL input signal. A function generator produces TTL pulses with a 2.5 kHz rep rate which are directed into the RF switch and the trigger of a lock-in amplifier. When the TTL signal is low the RF switch passes the pulses through an attenuator and directly into an RF power combiner (Minicircuits

ZYRSC-2-5.) When the TTL signal is high the pulses pass through spools of coaxial cable which significantly delay the pulse's arrival at the RF power combiner which combines both pulse trains. The attenuator is used to attenuate the first pulse train amplitude by the same amount as the spools of coaxial cable. The combined pulse train from the power combiner goes into the trigger of a Stanford Research Systems model DG645 delay generator. This delay generator is controlled with Labview to delay the pulses between 0 and approximately 200 ns before passing the signal on to the pulse generator. The pulse from the delay box triggers the pulse generator, generating the current pulse in the dither coil and thus the transverse magnetic field required to produce an FMR signal. This is the pump.

The other half of the beam not directed to the fast photodiode is directed through the same setup as the hysteresis loop measurements. This is the probe. A half-wave plate is used to rotate the incoming polarization as a way of controlling the beam power, a Glan-Thompson prism selects for only one polarization component, and a beam expander expands the beam before an objective focuses it down onto the sample. A collecting objective re-collimates and directs the beam through a quarter-wave plate and through a second Glan-Thompson to split the polarization components into two photodiodes. A preamp collects the subtracted signal between the photodiodes, but instead of passing it directly into the DAQ card as in the hysteresis loop setup, directs it to the lock-in amplifier. More details can be found in the Hysteresis Loop section.

To understand how this measures the FMR signal consider what happens in the system as optical pulses travel down the beam line towards the beam splitter. From the beam splitter the optical pulses take some fixed time to reach the sample. The optical pulses traveling to the photodiode generate signals which create the transverse field at the sample. The times vary depending on the lengths

of cable, delay box delay, electronics speed, and other variables. The optical pulses (probe) and transverse field (pump) are therefore arriving at different times, with the difference being  $\Delta t$ . The probe optical pulses arrive a constant time delay relative to the time of arrival at the beam splitter. As the laser rep rate is much faster than the 2.5 kHz RF switch rep rate, large numbers of photodiode generated electrical pulses pass through the RF switch before it switches between outputs. On the short time delay attenuator output, the total time delay  $\Delta t$  between the pump and probe is small relative to the delay available in the digital delay box (200 ns). The pump generates an FMR signal when it arrives while the optical probe arrives some time before or after this FMR signal is generated. The Faraday effect measured corresponds to the position of the FMR magnetization vector at the time the optical pulse arrives.

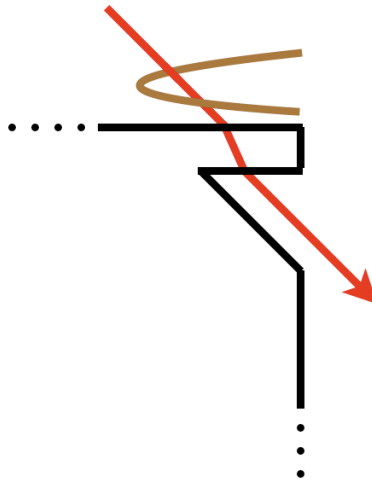


Figure 3.7: Schematic showing how the coil is brought in from the edge of the sample such that the beam can pass through the coil center, through the cantilever, and out of the sample.

When the RF switch directs the electrical pulses into the coaxial cable spool, the delay is large and the pump and probe arrive at the sample at times so far apart that the FMR signal generated by the pump has dissipated away and the probe cannot detect a Faraday effect. Thus as the RF switch toggles, the lock-

in amplifier alternately gets a signal corresponding to TTL low (which may be measuring an FMR signal) and TTL high (which corresponds to no FMR signal.) At this point the digital delay has not been varied. The TTL square wave from the function generator is the frequency the lock-in amplifier is locked in to, and so the lock-in measurement is the difference in magnitude of the Faraday effect between TTL high and low, or no FMR signal and an FMR signal.

The digital delay can now be changed. It changes  $\Delta t$  of both the TTL high and low pump times. This does not matter for the TTL high output however, due to the already large delay between pump and probe. It does matter for the TTL low output as the delay is small. Varying the digital delay now allows us to sample the FMR signal at different times by varying  $\Delta t$ . As we are varying the pump time, not probe time, care must be made to make sure the pump is arriving before the probe at zero digital delay. This ensures that as the pump is delayed, it will eventually arrive at the same time as the probe. This is equivalent to scanning backwards in time to sample the FMR signal. The individual samples at various  $\Delta t$  are plotted together to produce the complete FMR ring down.

### **3.2.5 Focusing Differences Through the Dither Coil**

To measure an FMR signal the beam must pass through both the cantilever and dither loop in a similar procedure to that for Hysteresis Loops. The beam is first focused and aligned through the cantilever as done for hysteresis loops. The objective lens is then defocused and the coil brought in above the cantilever such that its profile is visible in the expanded image view with no collimating lens. The coil is brought close to the surface, and the objective lens refocused slowly while the coil is adjusted to keep the beam in the center. The coil position can be improved by moving the coil to increase the FMR signal amplitude at a fixed time delay.

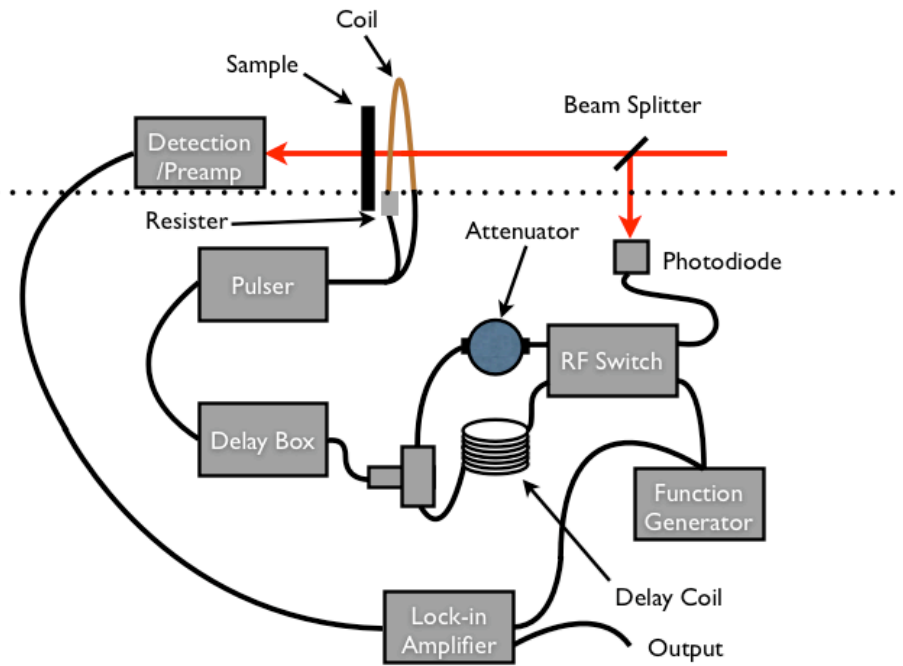


Figure 3.8: Schematic of the FMR experiment. The setup below the dotted line creates the variable delay pump, while the laser and detection above the dotted line are the probe. Half the incoming laser beam generates an electrical pulse at the photodiode for each optical pulse. The function generator provides a reference TTL square wave frequency to the lock-in and the RF switch. The TTL frequency is independent of the laser frequency, but affects the maximum delay the delay box can output. 2.3kHz was chosen to allow multiple measurements to be detected by the lock-in while still allowing a long enough maximum delay. The RF switch alternates the output between the attenuator and delay coil depending on the high/low TTL state. The pulses are combined in a power combiner, then enter the delay box for a digitally controlled delay. This box then outputs a signal to the pulse generator, which generates a large voltage pulse to the coil and surface mount terminating resistor. The second half of the beam passes through the coil and sample to the detection setup. The Faraday rotation signal is read from the lock-in amplifier.

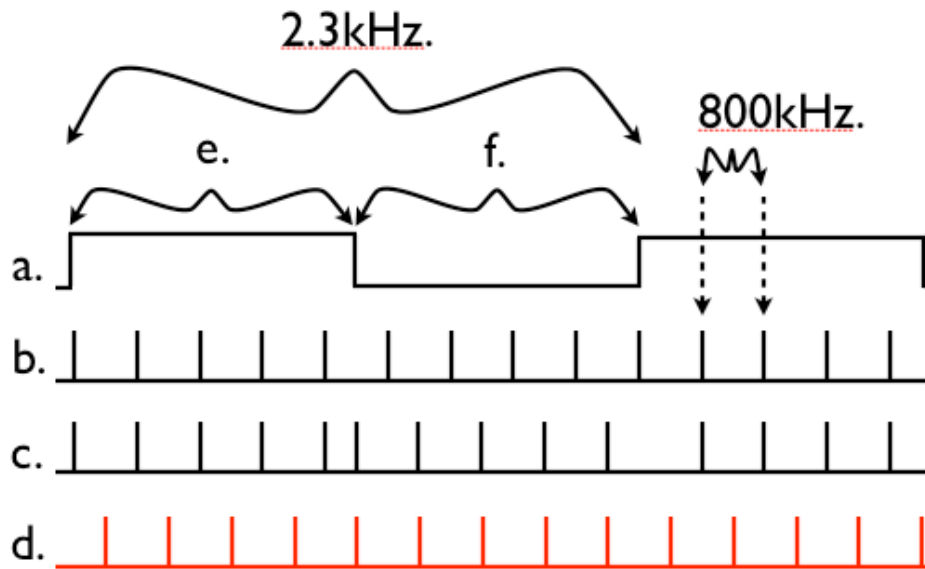


Figure 3.9: Timing diagram, not to scale, for the FMR experiment. (a) shows the TTL signal from the function generator. (b) is a series of pulses generated by the fast photodiode. After these pulses pass through the RF switch and attenuator/delay coil they are recombined into (c), the pump. Here a series of the pulses is shifted at the change in TTL signal. (d) is the incoming optical laser pulses which form the probe. (d) has been shifted relative to (b) from the the extra propagation delay of the laser and electrical setup. Comparing (c) and (d) we see that for the TTL high the pulses do not occur at the same time, and in this case the FMR caused by the pump (black) has dissipated by the time the probe (red) has arrived. When the TTL switches to low, the large shift in pump delay (black) aligns the pulses with the probe (red.) The digital delay  $\Delta t$  is too small to see in this diagram, but would be represented by a small shifting of the (c) back and forth such that the overlap between the black and red pulses in (f) varied.

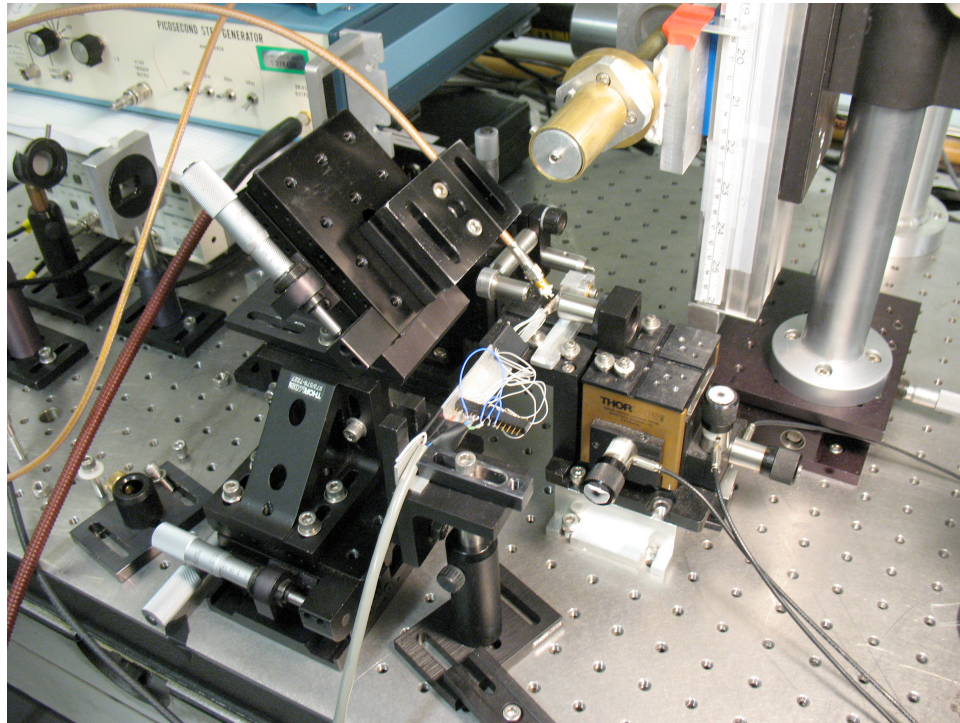


Figure 3.10: The setup modified for FMR. The dither coil is brought in with the 3 axis translation setup on the left. The Hall probe is visible approaching the sample from the bottom of the image.

# Chapter 4

## Modeling

*A simple numerical model of magnetic hysteresis loops similar to the Stoner-Wohlfarth model of magnetism is constructed. Hysteresis loops showing the same qualitative shape as measured experimentally are shown, and the procedure for programming the model in Matlab is outlined.*

### 4.1 The Stoner-Wohlfarth Model

The hysteresis loops observed in LuIG have a quite complex shape which varies depending on the sample orientation, applied field, and other variables. Possible reasons for this were mentioned previously, and the experimental effects of varying the sample orientation shown. In Chapter 1 it was discussed how the magnetization within a material results from the net orientation of magnetic dipoles within the material, and how this magnetization direction is determined from the various energy contributions of the material anisotropy and applied field. As this orientation varies to minimize the potential energy, the magnetization can be modeled by considering the energy contributions to it that depend on

orientation and field strength. The Stoner-Wohlfarth model (SW model) is the simplest model of magnetization that captures the general properties of a hysteresis loop. [32, 33] The SW model assumes that the sample behaves as a single magnetic dipole, which is reasonable as a relatively low field is required for the domains to align and rotate coherently together. The moment  $M$ , or magnetization, direction is determined from two energy contributions; the Zeeman energy from the externally applied field and anisotropy energy which is sample dependent. The various sample anisotropies such as crystalline and shape anisotropy are combined into a single anisotropy energy term. The equilibrium magnetization direction is stable when pointing in a direction that is a minimum of the energy. The model provides a way for finding the equilibrium position where the first derivatives of the total potential energy with respect to direction are zero, i.e. there is no net force on the magnetization vector. Three variants of the SW model were made for uniaxial, biaxial, and cubic anisotropy.

## 4.2 Energy Contributions to Magnetization Direction

The two relevant energy terms in the SW model are the Zeeman energy and the anisotropy energy. Other energy terms that do not depend on orientation are not relevant as their derivatives with respect to orientation are zero. The Zeeman energy,  $U$ , is the energy between the applied field and magnetic moment,

$$U_z = -\vec{M} \cdot \vec{H} \quad (4.1)$$

with  $\vec{M}$  the magnetic moment and  $\vec{H}$  the applied field. The combined anisotropy energy  $E_a$  of the magnetization at a direction  $\theta$  from the anisotropy easy axis is modeled by

$$E_a = K \sin^2(\theta) \quad (4.2)$$

This is an approximation, giving the general qualitative behaviour. The easy axis is that orientation which minimizes the energy, while that direction which maximizes the energy is the hard axis.  $K$  is the effective anisotropy energy. Equations 4.1 and 4.2 compete to try and align the magnetization both along the easy axis and with the field direction, with the resulting magnetization direction being that which minimizes both.

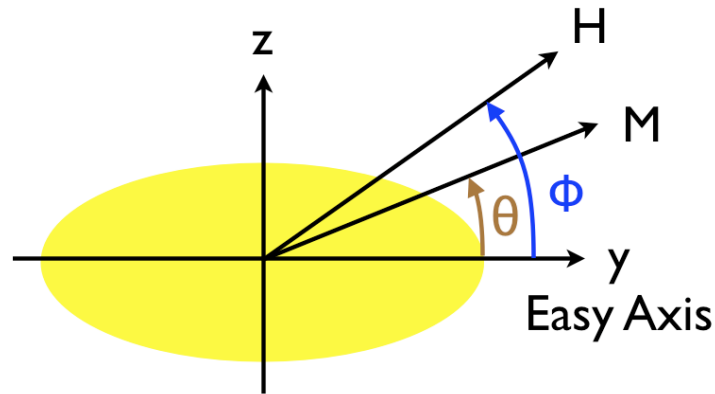


Figure 4.1: Uniaxial SW model vector definitions.  $H$  is the applied field an angle  $\phi$  from the easy axis ( $y$  axis), and  $M$  the magnetization direction an angle  $\theta$  from the easy axis.

The SM model is simplest when considering the problem in two dimensions with uniaxial anisotropy. This commonly arises in thin films where the shape anisotropy forces the magnetization to vary in the film plane, or in thick samples with strong out-of-plane anisotropies. In either case the energy is minimized when the magnetization varies only within a plane, usually the sample surface. Further energy minimization depends on the strength and direction of the applied field in this plane. Most implementations of the SW model are for this case; however, in our experiment we rotate the magnetic field down into the sample plane instead of varying the field strength.

Consider a field  $H$  applied in a plane, the  $YZ$  plane, at some angle  $\phi$  from the easy axis which lies along the  $y$  axis in Figure 4.1 We'll assume the field

and magnetization are along the in-plane easy axis, and so the system can be considered 2D with a uniaxial anisotropy. Defining the magnetization to be an angle  $\phi$  from the  $y$  axis, the total energy is then

$$E = K \sin^2(\theta) - M_s H \cos(\phi - \theta) \quad (4.3)$$

and the derivative  $dE/d\theta$ ,

$$dE/d\theta = 2K \cos(\theta) \sin(\theta) - M_s H \sin(\phi - \theta) = 0 \quad (4.4)$$

Solving  $dE/d\theta = 0$  with  $d^2E/d\theta^2 > 0$  for  $\theta$  under various applied field strengths and/or directions gives the equilibrium angle of the magnetization. The second derivative must be  $> 0$  to ensure that an energy minimum has been reached, not an unstable maximum.

### 4.3 Model Implementation

A variety of implementations of this basic equation were made in Matlab to model the magnetization behaviour. All implementations define  $h = H/H_o$ , with  $H_o$  the field which saturates the magnetization. In the conventional hysteresis plot  $H$  is varied at a constant  $\phi$  (orientation) from  $-H_o$  to  $H_o$ , and the derivatives of the energy with respect to  $\theta$  solved to find  $\theta$ .

Equation 4.4 can be divided by  $M_s * H_o$  and given an new effective  $K_{eff} = K/[M_s K_s]$  to simplify the equation to

$$dE/d\theta = 2K_{eff} \cos(\theta) \sin(\theta) - h * \sin(\phi - \theta) = 0 \quad (4.5)$$

This results in the standard hysteresis plot showing saturation, remanence, and coercivity. (Figure 4.2) In the SW model implemented here the magnetic

field is held at a fixed strength  $h$  while the direction is varied and the equilibrium positions of  $\theta$  found.

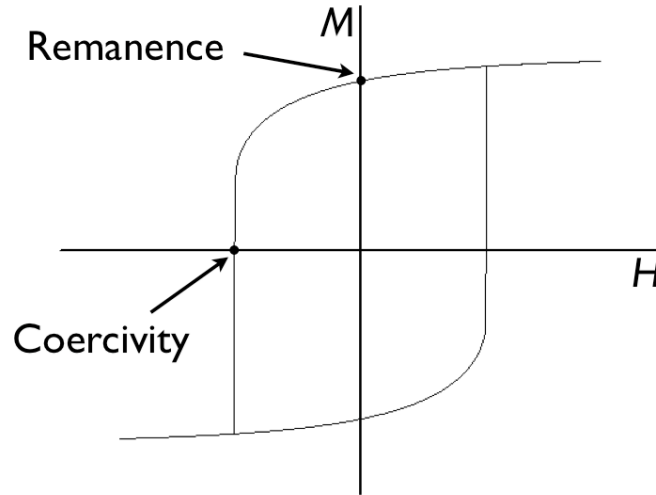


Figure 4.2: A conventional hysteresis loop modeled by varying the applied field strength ( $H$ ) in-plane, but not its direction, and recording the resulting magnetization. The Remanence is the remaining magnetization when the applied field has been reduced to zero, and the coercivity the applied field required to reduce the magnetization in the sample to zero. In a material with sudden magnetization flips the coercivity field strength will also be that which causes a magnetization transition.

To program the model in Matlab, all conditions such as constants, rotation of the sample, an array of rotation positions of the magnet, etc, are set. For each rotation position of the magnet the applied field strength and direction is found and used to find the solution to  $dE/d\theta = 0$ , giving a stable magnetization orientation. How to find this varies depending on the model complexity, and is discussed later. With the magnetization direction known, the projection onto the beam direction is found. The experimentally measured Faraday rotation is proportional to the magnetization in the beam direction. Plotting this vs. the applied field strength in a given direction gives the measured hysteresis loops.

### 4.3.1 Origin of Hysteresis

Solving for the solutions of  $dE/d\theta = 0$  is complicated by how this function changes with applied field direction,  $\phi$ . This, and the source of the hysteresis effect, can be seen by plotting  $dE/d\theta$  for various  $\phi$  in Figures 4.3 and 4.4. In the first, the field strength is set equal to that required for saturating the magnetization along the hard axis direction;  $h = 1 = H/H_0$ . As  $\phi$  varies we can see that each curve has only one solution to  $dE/d\theta = 0$ , and at  $\phi = 90^\circ$  corresponding to alignment along the hard axis;  $\theta = 90^\circ$ . As the applied field is strong enough to push the magnetization directly through the hard axis, there is only one solution for each  $\phi$ , and no hysteresis results.

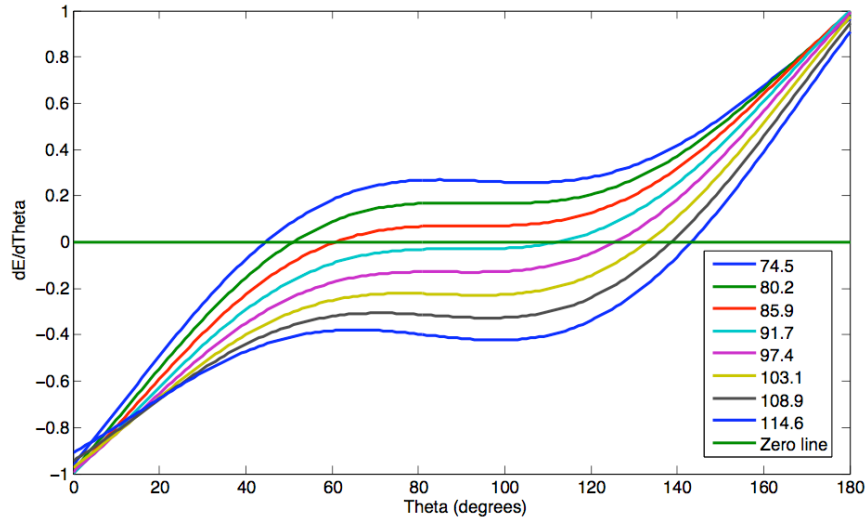


Figure 4.3:  $dE/d\theta$  plotted for the given values of  $\phi$  in the legend. The applied field is strong enough to force the magnetization through the hard axis, and the equilibrium direction is where each curve crosses  $dE/d\theta = 0$ . There is only one solution for each  $\phi$ . It can be seen that the applied field direction is closer to the hard axis direction ( $\theta = 90^\circ$ ) than the magnetization. This is expected as the applied field is trying to align the magnetization with it, while the anisotropy pushes the magnetization direction away from it.

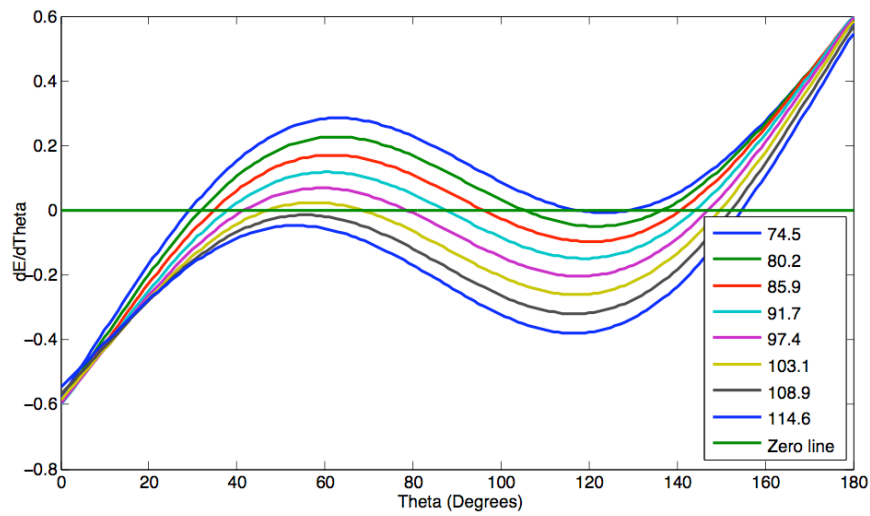


Figure 4.4: Here the applied field  $H = 0.6H_o$ . When the applied field is close to aligned with the hard axis the magnetization has two stable positions, one on either side. As the applied field direction reaches and begins to cross over the hard axis direction ( $\phi$  increasing past  $90^\circ$ ), the magnetization remains at the first stable set of solutions near  $\theta = 45^\circ$ . This remains the stable solution until  $\phi$  moves from  $103.1$  to  $108.9^\circ$ . At this point the curve drops below the  $dE/d\theta = 0$  line, indicating there is no stable direction for the magnetization here. The magnetization switches to the next stable solution near  $\theta = 140^\circ$ . The delayed switch in magnetization direction after  $\phi$  has passed the hard axis direction gives rise to hysteresis.

In Figure 4.4, the field strength is 60% of that required for complete magnetization along the hard axis. Many of the plots of  $dE/d\theta$  have two solutions to  $dE/d\theta = 0$  for a given  $\phi$ . How this gives rise to a hysteresis effect and the difficulty of modeling can be seen from following what happens to the solution  $\theta$  as  $\phi$  varies. When  $\phi$  starts at  $74.5^\circ$ ,  $\theta$  is  $\sim 30^\circ$ . The magnetization direction is pinned at this location and cannot switch to the next zero ( $\theta \sim 120^\circ$ ) because of the energy barrier between the two solutions.  $\theta$  increases as  $\phi$  does, and even as  $\phi$  goes past  $90^\circ$  to around  $103^\circ$ ,  $\theta$  remains less than  $90^\circ$ . At this point the applied field is trying to force the magnetization through the hard axis, but is unable to do so. When  $\phi$  goes from  $103.1$  to  $108.9^\circ$  we see that the first solution to  $dE/d\theta = 0$  disappears, as is shown by the curve dropping below 0. At this point the energy contribution from the applied field is stronger than that of the anisotropy, the magnetization suddenly flips through the hard axis to align closer with the applied field, and  $\theta$  increases to  $\sim 150^\circ$ .

The difficulty arises in that care must be taken to ensure that Matlab solves  $dE/d\theta = 0$  for the correct solution  $\theta$ . Matlab solves an equation equal to zero for the correct solution by starting with a user supplied initial guess answer, and then iterating to reduce the difference from zero of  $dE/d\theta$  below some value at which point it provides the solution  $\theta$ . In a simple model like this it is done by giving an initial guess to the solving method (fsolve in Matlab) that is close to the initial equilibrium location, for example with both the applied field and  $\theta$  along an easy axis. The location in  $\theta$  and  $\phi$  where the first and second energy derivatives are zero is the location at which the magnetization switches and where a new initial guess to  $dE/d\theta = 0$  is appropriate. In Figure 4.4 this is the location where the maximum or minimum of a curve passes through the  $dE/d\theta = 0$  line. A full hysteresis loop is produced by first determining the location of these magnetization switches in  $\phi$ , then solving  $dE/d\theta = 0$  using the correct initial

guesses for a given range of  $\phi$ .

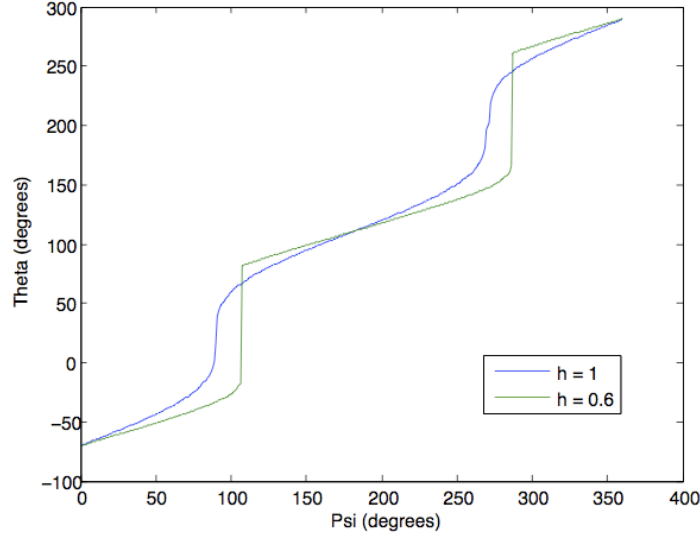


Figure 4.5: The equilibrium position  $\theta$  giving the magnetization direction as a function of applied field direction  $\phi$ . For  $h = 1$  the magnetization direction changes smoothly. Hysteresis and the sudden magnetization direction changes occur for  $h = 0.6$ .

Plotting how the equilibrium position  $\theta$  varies for the values of  $h$  used in Figures 4.3 and 4.4 we can see the sudden magnetization direction transition occurs only for  $h$  less than that required to fully magnetize the sample along the hard axis direction ( $h < 1$ , Figure 4.5.) From this the corresponding hysteresis loops can be produced. Given that LuIG has an index of refraction of approximately 2, rotating the sample by  $45^\circ$  corresponds to the beam passing through the sample at  $20^\circ$  off normal incidence. The applied field in the sample plane is found from the projection of  $h$  in that direction.

Figure 4.6 shows the projection effect and the effect of different field strengths. At high field,  $h \geq 1$ , there is no abrupt transition in magnetization. At 0 in-plane field,  $h$  is pointing out-of-plane along the hard axis of the sample.  $m$  reaches a maximum as the magnetization passes through the hard axis, and at normal incidence the plot is symmetrical around  $h = 0$ . At  $45^\circ$  rotation,

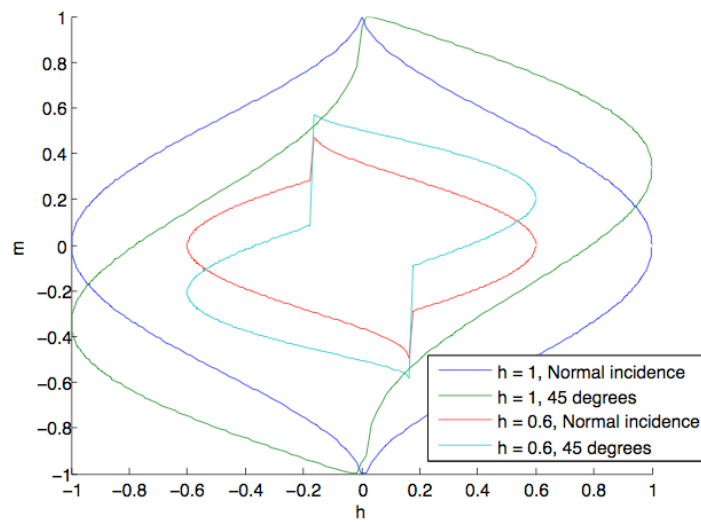


Figure 4.6: Uniaxial SW model showing the projection of magnetization along the beam direction ( $m$ ) vs. the component of the applied field in the in-plane sample direction ( $h$ ).  $h$  has a constant magnitude given in the plot legend, and varies in direction only. The sample orientation to the laser beam is given in the legend, either normal or  $45^\circ$ . The magnitude of the Faraday rotation is seen to decrease for applied fields not sufficient to fully magnetize the sample, while the sample orientation changes the projection of the magnetization onto the beam direction and so the hysteresis shape. Sudden magnetization transitions are only seen for the low applied field cases.

corresponding to the beam passing through at  $20^\circ$  off normal incidence, the plot is no longer symmetrical because of the projection of the magnetization onto the beam direction, but still does not have a sudden magnetization transition or hysteresis. When  $h$  is reduced to 0.6 a sudden magnetization transition and hysteresis effect appears for both the normal and  $45^\circ$  incidence plots. This is the expected effect of the applied field being too weak to force the magnetization to closely follow it through the hard axis. The projection effect of the laser beam at  $45^\circ$  to the sample surface is to shift the plot and increase the apparent magnetization transition size.

### 4.3.2 Model in Three Dimensions

The model can be extended to three dimensions by including a second anisotropy easy axis and using spherical coordinates. The applied field is defined in three dimensions as in Figure 4.7. The equilibrium position of the magnetization is found from solving for both  $dE/d\theta_m = 0$  and  $dE/d\phi_m = 0$ , where these are the two angles in spherical coordinates which specify the direction of the magnetization. In the 3D model the out-of-plane easy axis is the XY plane in Figure 4.7, which represents the sample surface. The in-plane easy axis lies along the y axis, which forms the ZY plane. The intersection of these planes, the y axis, is the direction of lowest anisotropy energy for the magnetization.

In spherical coordinates the energy is

$$E = K_o \cos^2(\theta_m) + K_p \cos^2(\theta_m) \quad (4.6)$$

$$- M_s H [\sin(\theta_m) \cos(\phi_m) \sin(\theta_h) \cos(\phi_h)] \quad (4.7)$$

$$+ \sin(\theta_m) \sin(\phi_m) + \sin(\theta_h) \sin(\phi_h) \quad (4.8)$$

$$+ \cos(\theta_m) \cos(\theta_h)] \quad (4.9)$$

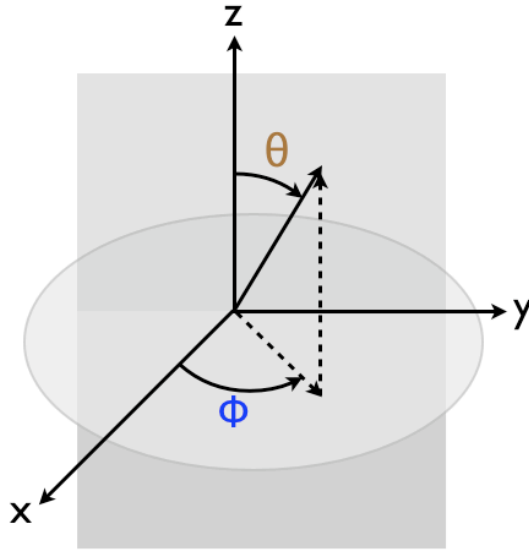


Figure 4.7: The spherical coordinates used for the three dimensional SW model. The sample lies in the XY plane, with the magnet rotating in the ZY plane.  $\theta$  and  $\phi$  are defined from the hard axis directions (the Z and X axes,) and are different than in the uniaxial model case.

Here  $K_o$  is the out-of-plane anisotropy constant,  $K_p$  the in-plane anisotropy constant,  $\theta_m$  and  $\phi_m$  the magnetization angles, and  $\theta_h$  and  $\phi_h$  the applied field angles.

The magnet is defined to rotate in the ZY plane. The magnetic field does not emerge normal to the magnet surface, so a misalignment angle is built into the model. This is the angle off normal from the magnet surface at which the field emerges. When the magnet rotates in a circle in the ZY plane the applied field traces out a cone shape. In this model we can vary the applied field strength, two anisotropy strengths, the rotation of the sample relative to the rotation plane of the magnet, the angle of opening of the applied field cone that is swept out, and the direction of the beam which measures the magnetization.

## Initial Guess Complications

While the model math itself is simple, the large number of variables in the model make it difficult to implement. The general process is to solve the system of equations  $dE/d\theta_m = 0$  and  $dE/d\phi_m = 0$  for the magnetization position. As in the single anisotropy axis case, an initial guess of the solution is used by the `fsolve` function in Matlab to find a solution to the equations. The energy landscape is even more complicated, and a method must be found for giving the correct initial guess. Like in the 1D case, solving for where the first and second energy derivatives are zero to find the location of magnetization transitions was attempted, but was not successful. I believe it was not because of the complicated landscape of possible solutions to the system of equations of energy derivatives. The  $dE/d\theta_m$  and  $dE/d\phi_m$  and their second derivatives cannot be solved separately as they are not independent of each other. Solving a system of four equations,  $dE/d\theta_m$ ,  $dE/d\phi_m$ ,  $d^2E/d\theta_m^2$ , and  $d^2E/d\phi_m^2$  leaves out  $d^2E/(d\theta_m d\phi_m)$  which may be necessary. The magnetization may flip if either pair of derivatives is zero, but again each pair cannot be determined independently. Regardless, finding the solution of the four equations to determine the initial guess for the first derivatives, which in turn requires a correct initial guess, was not successful. Although solving using the pairs of derivatives independently was successful, the results do not accurately reflect real hysteresis loops.

A second method was tried that starts with a known initial applied field and magnetization direction which is correct, such as along both easy axes, and advances the initial guess of  $\theta_m$  and  $\phi_m$  when needed until a new stable solution is found. The system  $dE/d\theta_m = 0$  and  $dE/d\phi_m = 0$  is solved given the current applied field direction. The absolute values of  $dE/d\theta_m$  and  $dE/d\phi_m$  are checked to ensure they remain approximately zero. If so, the next applied field step is used, the system solved to find the equilibrium position, and the first energy derivatives

checked again. At a point where the initial guess is no longer valid as there is no equilibrium magnetization direction and a sudden switch must happen, at least one of the first energy derivatives will diverge from zero. A new initial guess can be checked knowing approximately the direction which should next be stable, and the guess advanced until a stable solution is found. This method was found to work, albeit only for a limited range of variables. If the initial guess values are not those lying on a true magnetization curve, other solutions can be found for a magnetization direction which is not correct. These may appear as either non-sensical shapes, or sometimes as smooth curves mimicking some properties of a real hysteresis loop. How to advance the guess in  $\theta$  and  $\phi$  requires some knowledge of where the correct solution will be, and the size of the advance step was found to affect the plot, apparently by skipping over correct and incorrect possible solutions. If the advancement in initial guess is not along the direction of the magnetization then an incorrect solution may be found. The best solution would be to evaluate all the first and second derivatives to determine where the magnetization will rotate to, given an energetically unstable point. This was tried unsuccessfully, and time constraints meant it wasn't pursued further.

For the biaxial anisotropy case, there is always one correct guess for a stable position in  $\theta$ ,  $\theta = 90^\circ$ , and two in  $\phi$ ,  $\phi = 90^\circ$  and  $\phi = -90^\circ$ . This can be seen from Figure 4.7. This makes implementation relatively simple, in that the system can be started at a known equilibrium position, and when  $dE/d\theta_m$  or  $dE/d\phi_m$  are no longer zero, the next initial guess can be tried. This method was found to work, with a few problems. Care must be taken in checking when the energy derivatives are no longer zero. The `fsolve` function can return a value when it no longer converges to solution; however, it was found that `fsolve` continued to report a correct solution while  $dE/d\theta_m$  or  $dE/d\phi_m$  were no longer zero but still small. Depending on the sample orientation and other effects this produced some correct

plots, some with subtle differences around magnetization transitions, and some with completely non-physical results. Instead the first derivatives are manually checked to see that their absolute values are below some arbitrary limit, and if not the new initial guess is tried. Too small a limit and the hysteresis effect is not seen as the new initial guess is tried too early in the magnet's rotation, while too large a limit can cause the next initial guess to be tried after several new applied field directions during which the magnetization is diverging and which causes the magnetization to jump to a new equilibrium location, producing a hysteresis loop that does not correspond to any kind of magnetization change. By using approximately one order magnitude larger than the usual numerical error in solving the system of equations with `fsolve` (e.g.  $10^{-7}$  as the limit when errors are on the order of  $10^{-8}$ ) produces valid hysteresis curves. Once a record of magnetization positions has been recorded, the projection onto the laser direction is recorded along with the applied field in the same manner as the 1D anisotropy case, to produce a hysteresis loop. This method of advancing the initial guess to the solution of the energy derivatives was checked by rotating the magnetization multiple times to insure the results remain consistent, and starting the initial guess at strange magnetization directions to make sure it converged to a logical direction.

A large variety of hysteresis loops can be produced by the biaxial model, but none of them have the second transition seen in the experimental data. Changing the field strength causes a transition to appear, as in Figure 4.8. Changing the relative strength of  $K_p$  and  $K_o$  has little effect at high applied fields which dominate the magnetization rotation direction compared to the anisotropy. At low fields this ratio is more important, as in Figure 4.9. The angle of rotation of the applied field and the beam direction through the sample can produce a variety of different plot shapes, Figure 4.10.

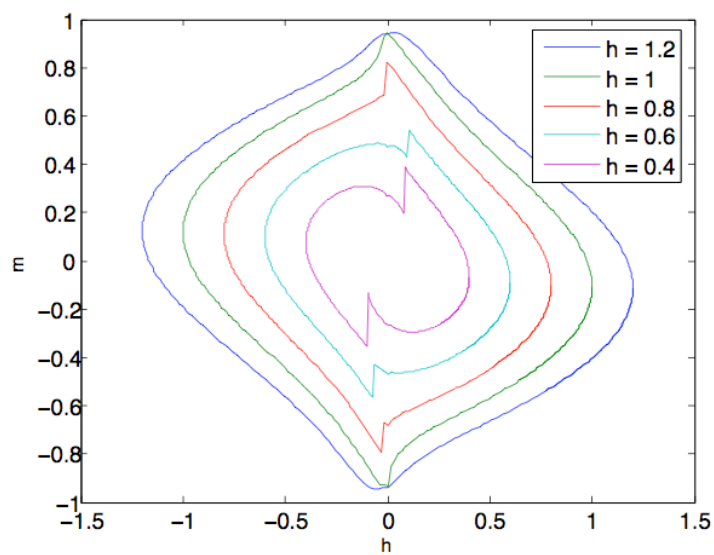


Figure 4.8: Biaxial model hysteresis loops at a  $45^\circ$  sample tilt and  $20^\circ$  sample rotation in the plane of the beam. Out-of-plane anisotropy  $K_o = 0.5$ , in-plane anisotropy  $K_p = 0.1$ . Changing the applied field magnitude changes the hysteresis loop shape. Lower magnitude applied fields create smaller hysteresis loops with a larger magnetization transition. At fields large enough to fully magnetize the sample in the hard axis direction the sudden vertical magnetization transition turns to a smooth transition.

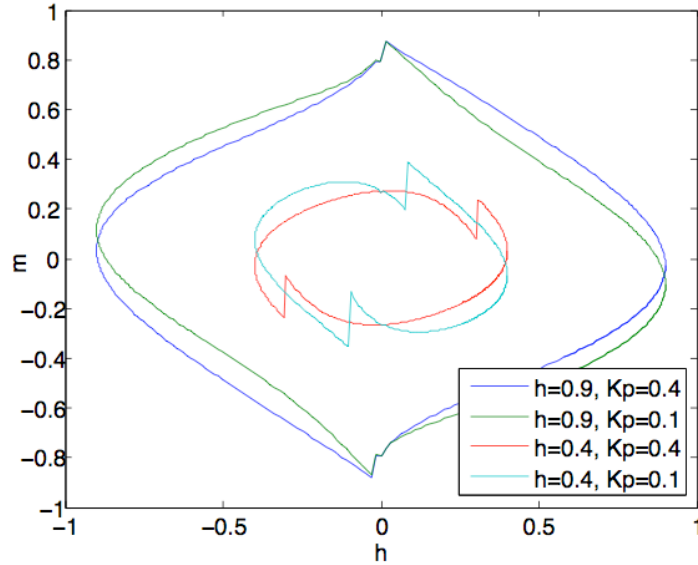


Figure 4.9: Biaxial model hysteresis loops at a  $45^\circ$  sample tilt and  $20^\circ$  sample rotation in the plane of the beam. Out-of-plane anisotropy  $K_o = 0.5$ , in-plane anisotropy  $K_p = 0.1$ . At high applied fields relative to the anisotropy strength ( $h=0.9$ ) the applied field dominates the anisotropy in determining the magnetization direction. No magnetization transitions are visible and changes to the anisotropy strength from  $K_p=0.4$  to  $0.1$  only slightly affects the plot shape. At low fields, ( $h=0.4$ ), the magnetization transitions are visible and their location depends on the anisotropy strength.

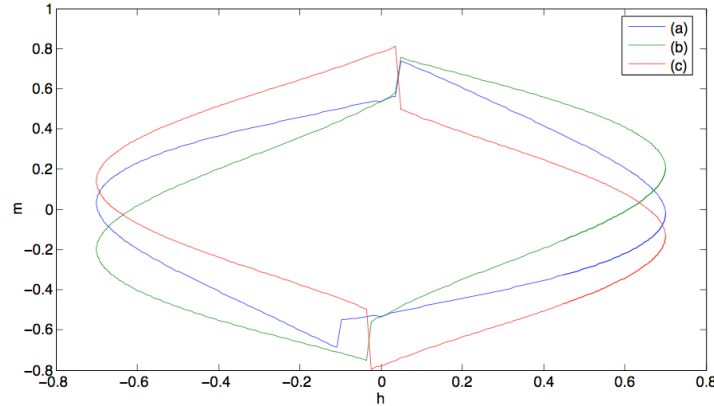


Figure 4.10: A variety of the curves that can be obtained by changing orientation of the laser beam and applied field relative to a sample with biaxial anisotropy. (a) shows a hysteresis loop with a field magnitude  $h=0.7$ , out-of-plane anisotropy  $0.5$ , and in-plane anisotropy of  $0.2$ . The beam is incident at  $45^\circ$ , and the applied field rotates in a plane rotated  $50^\circ$  from the in-plane easy axis. In (b) the plane into the sample at which the magnet rotates has been rotated by  $60^\circ$  from (a). In (c) the angle between the sample in-plane easy axis and the direction in-plane at which the beam passes through the sample has been rotated by  $30^\circ$ .

### 4.3.3 Cubic Anisotropy

Cubic anisotropy can be introduced by changing the in-plane anisotropy term to  $2\theta$  from  $\theta$ . The anisotropy can be made symmetric around only one in-plane axis, not both, by adding a second anisotropy term with only  $\theta$ ,

$$E = K_o \cos^2(\theta) + K_{1p} \cos^2(2\theta) + K_{2p} \cos^2(\theta) \quad (4.10)$$

$$- M_s H [\sin(\theta) \cos(\phi) \sin(\theta_h) \cos(\phi_h)] \quad (4.11)$$

$$+ \sin(\theta) \sin(\phi) + \sin(\theta_h) \sin(\phi_h) \quad (4.12)$$

$$+ \cos(\theta) \cos(\theta_h)] \quad (4.13)$$

Derivatives are taken as before, and the equations solved by the method of starting with a stable solution and advancing the initial guess whenever the solution becomes unstable. Advancing the initial guess was difficult as, depending on the sample orientation, field orientation, and anisotropy strengths, it isn't clear where the next correct stable solution will be. Instead, a small advancement was made, the derivatives checked for convergence, and the initial guess advanced again if necessary.

The cubic anisotropy model only produces meaningful results for a certain range of variables, and the initial guesses used can significantly affect the hysteresis loop in some specific cases. Significant work needs to be done before the model results can be fully trusted. That being said the model did reproduce several of the effects seen in experimental hysteresis curves, particularly the double transition. As for the previous models the results should only be taken qualitatively. The cubic anisotropy model produces the second transition under all conditions the model works for, and the hysteresis curves vary as expected for the range of variables that produce stable results. Figure 4.11 shows the second transition given by the cubic anisotropy, compared to a plot from the biaxial model with

the same parameters. The close alignment verifies that the different methods of finding the initial guess are at least consistent with each other.

The location and strength of the second transition varies significantly depending on the model parameters. For example rotating the angle of the beam entering the sample with respect to the in-plane easy axis has a different effect depending on the in-plane angle between the easy axis and the plane in which the applied field rotates. Figures 4.12 and 4.13 were taken at an applied field rotation of  $20^\circ$  and  $-80^\circ$ , respectively, of the plane of magnet rotation relative to the in-plane hard axis. Varying the in-plane beam angle from  $120^\circ$  to  $140^\circ$  has a significantly different effect for these applied field orientations. In the first case the amplitude of the second transition varies, while in the second case the second transition amplitude is approximately constant.

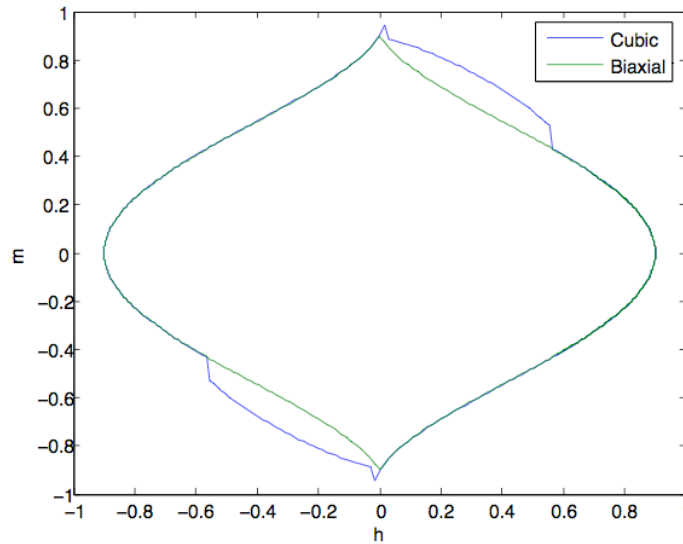


Figure 4.11: The biaxial and cubic anisotropy models produces similar hysteresis plots, with the cubic showing an additional magnetization transition. The cubic anisotropy models produce two pairs of magnetization transitions, one located near zero in-plane applied field, and a second located between  $h = 0$  and  $h = 1$ .

Changing the sample tilt changes the plot shape, and for some tilts the second transition will disappear, as in Figure 4.14. When the sample is rotated, the

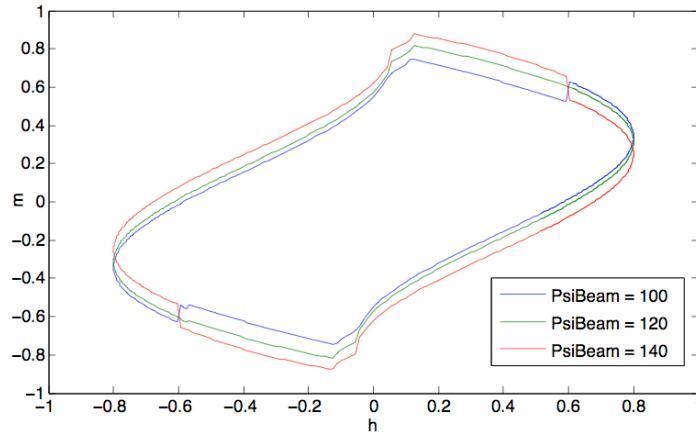


Figure 4.12: The second magnetization transition can vary with the projection effect of the beam passing through the sample at different angles. The sample has a  $20^\circ$  angle between the in-plane hard axis and applied field rotation plane, a  $45^\circ$  tilt, and  $K_p = 0.2$ ,  $K_o = 0.5$ . The angle in-plane between the beam and in-plane hard axis is rotated by the angles shown in the legend. This is equivalent to rotating the sample around the beam axis while keeping the angle between the easy axis and applied field constant.

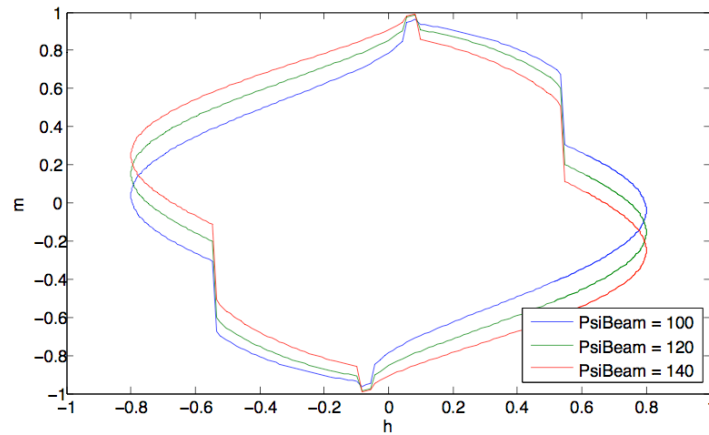


Figure 4.13: The sample has a  $-80^\circ$  angle between the in-plane hard axis and applied field rotation plane, a  $45^\circ$  tilt, and  $K_p = 0.2$ ,  $K_o = 0.5$ . Changing the angle between the in-plane hard axis and applied field rotation plane compared to 4.12 creates different hysteresis loops when the in-plane beam angle is rotated by the angles shown in the legend.

second magnetization transition position varies as is shown in Figure 4.15. The effect in the model is smaller than that seen experimentally, and only a small range of sample rotations produces stable hysteresis loops. An unstable result is shown here for a sample rotation of  $50^\circ$ .

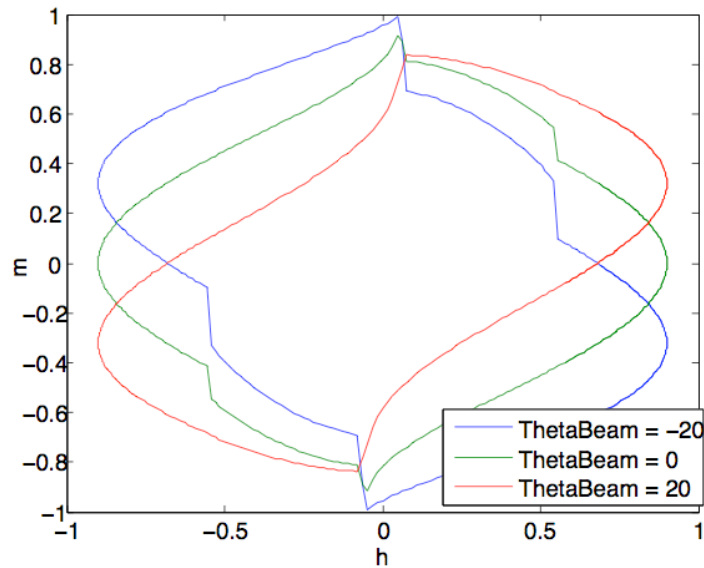


Figure 4.14: Changing the angle the beam enters the surface at from normal (ThetaBeam) changes the hysteresis loop shape. For some tilts the projection effect of the beam causes the second transition to disappear.

Changing the strength of the in-plane relative to out-of-plane anisotropy changes the location of the second transition. (Figure 4.16) This is expected and a useful check on the models results despite there being no experimental results with which it can be compared.

Figure 4.17 shows an example of some of some of the more complex curves the model can produce. These plots were each produced with two rotations of the applied field, differing in that they have a one order of magnitude difference in the numerical error of fsolve in recognizing a divergence in the solutions and triggering the next initial guess. The model typically does not show differences between multiple revolutions of the applied field, and it isn't clear why under some

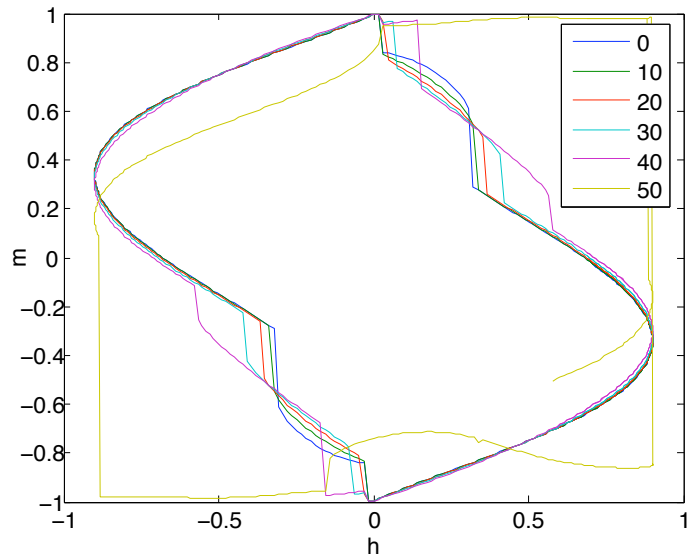


Figure 4.15: Rotating the sample relative to the applied field causes the second magnetization transition to vary in position around the hysteresis loop. Different rotations of the sample in degrees are shown. This is similar to what is seen experimentally. Rotations above  $40^\circ$  produce unstable results such as the one shown.

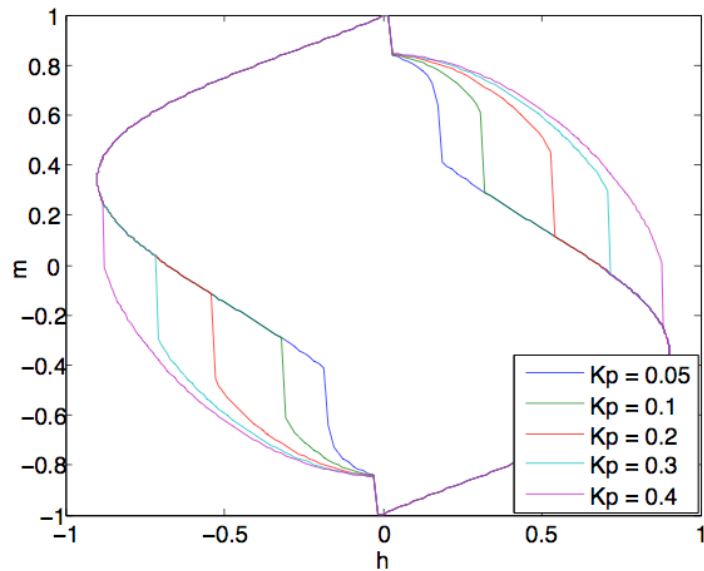


Figure 4.16: Changing the in-plane anisotropy changes the location of the second magnetization transition. This is reasonable as a change in in-plane anisotropy will change the field strength required to cause a magnetization transition across an in-plane hard axis. Changing the field at which a magnetization transition occurs will change the location it appears in the rotation of the magnet.

conditions the shape changes under multiple rotations. This difference between rotations is repeatable in multiple runs of the entire model. Changing other parameters such as the sample orientation will remove the complex transitions of the green curve, while a change in field strength will reduce the magnetization rotation but show a similarly complex shape. It may be that both solutions are possible in reality and lie energetically and physically close together, where differences in the model between successive rotations and the numerical errors cause the magnetization to switch between solutions. Similar hysteresis loops have been found experimentally, Figure 4.18, which closely follow most of the magnetization transitions of the model. This indicates the model is giving at least somewhat realistic results for the cubic anisotropy case.

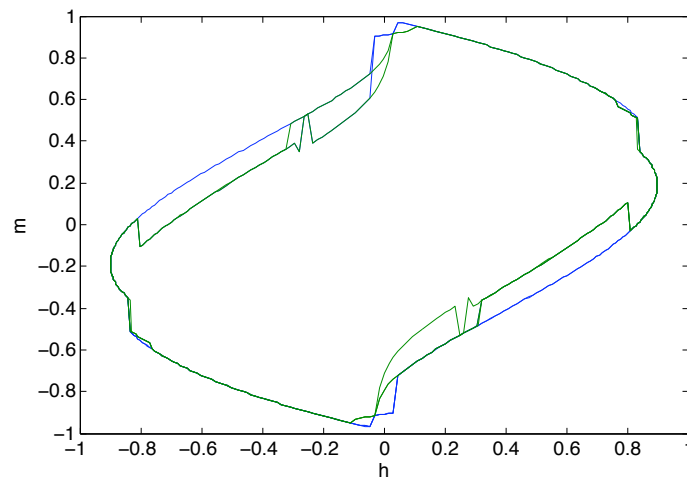


Figure 4.17: Complicated hysteresis plots can be produced under specific sample and field orientations. It's unclear if this is a numerical error by the model, or a physical result. Similar plots are found experimentally, and can a smooth change in plot shapes between this plot and other more common hysteresis loop shapes can be modeled.

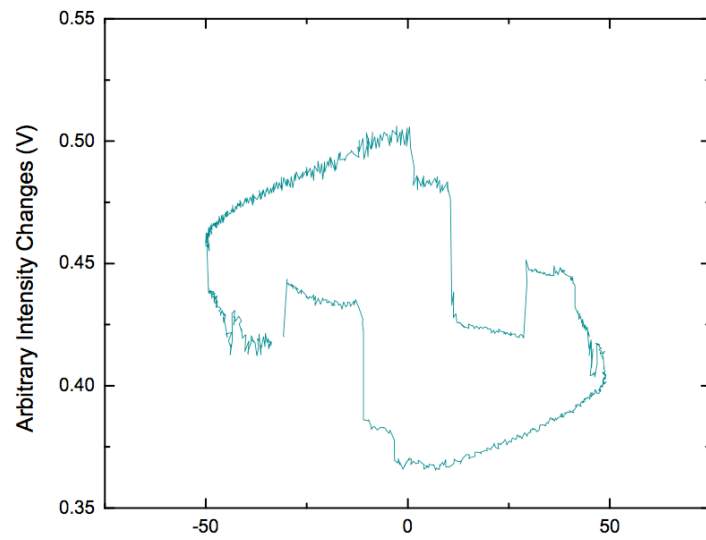


Figure 4.18: An experimental hysteresis loop through a cantilever. This pattern was reproducible but only seen in this particular cantilever.

## Chapter 5

# Hysteresis Loops

*Hysteresis plots for LuIG cantilevers are presented. A variety of effects can make interpreting hysteresis plots difficult. These effects will be investigated, so that the magnetization within LuIG structures can be understood and any changes due to ion implantation determined. Ferromagnetic resonance in the thin film sample and cantilevers will be demonstrated.*

### 5.1 Hysteresis Loop Summary

As hysteresis plots measure the static magnetization of a sample they are an efficient way to investigate how this magnetization changes within an ion milled structure. Changes in magnetization due to ion implantation and the corresponding hysteresis loop changes may be masked by a variety of effects: changes in a samples geometry, easy axis angle, sample mounting orientation, applied magnetic field direction and magnitude, incident linear polarization direction, shape anisotropies, substrate properties, Hall probe position, and beam power. Since comparisons between cantilevers are difficult, the experimental setup and the

above effects were investigated so that any differences between Faraday rotation signals would be understood.

## 5.2 Lutetium Iron Garnet Hysteresis Loops

### 5.2.1 Differences from Sample Mounting Orientations

To first understand the hysteresis plots they were taken through the LuIG thin film and substrate, referred to as the bulk. The thin film won't have large shape anisotropies compared to the cantilevers, and will also have the largest possible signal and no ion damage. The sample was mounted normal to the incoming laser beam and rotated in this position around the beam axis. The incoming laser polarization orientation was held fixed. After each rotation of the sample the beam was realigned approximately through the center of the sample, and a hysteresis loop obtained by rotating the magnet. Hysteresis loops obtained at a variety of angles are shown in Figure 5.1. We can see the angle of the easy axis relative to the applied field and polarization direction does not matter as all plots align closely. This is expected since only magnetization changes into the sample plane, and therefore along the laser propagation direction, will be detected in this orientation as there is no component of the beam in-plane. As the magnetic field vector rotates through the sample the magnetization follows it to a greater or lesser degree depending on the magnetic field strength. Any sudden flips in magnetization will result in a change in direction of this vector, but the projection onto the beam direction is the same. At strong fields the magnetization closely follows the rotating applied field and the hysteresis will be approximately circular. The slight elliptical shape here is likely due to the sample not being mounted exactly tangential to the beam so a small projection effect is visible, combined with the not completely symmetrical flip of magnetization

through a hard axis. This effect is demonstrated in the Modeling chapter.

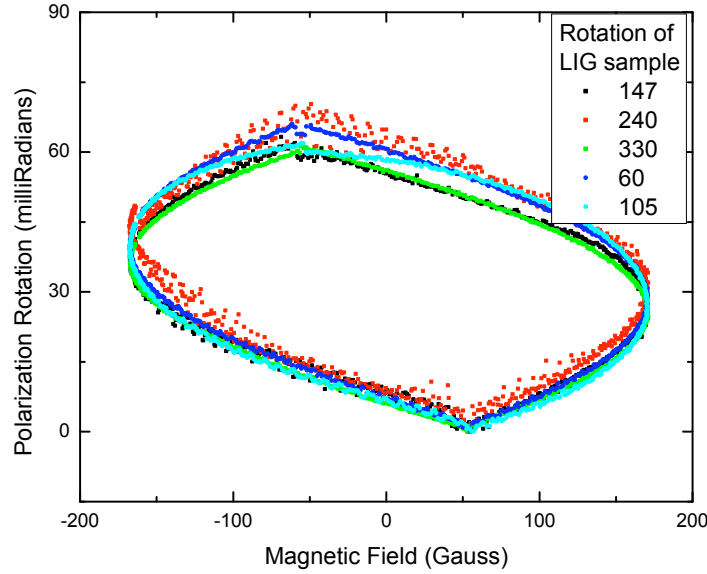


Figure 5.1: Thin film unmilled LuIG mounted nearly tangential to the beam ( $\theta = 90^\circ$ ) and the Faraday rotation shown for various rotations  $\phi$  in degrees, listed in the legend.

### 45° Sample Tilt

The results are different when the same sample is mounted at  $45^\circ$  to the beam. This angle was chosen as a convenient angle at which the beam can pass through a structure on the edge of the sample, without hitting the substrate underneath. The plots in Figure 5.2 can be seen to change as the sample is rotated in  $\phi$ , unlike those with the sample mounted normal to the beam. The incoming polarization direction is kept fixed, so the angle between the in-plane easy axis and polarization as well as the in-plane easy axis and magnetic field, changes. Two magnetization transitions are visible in these plots. Each plot has four sudden jumps in the data, corresponding to sudden changes in magnetization. These come in two pairs of transitions, anti-symmetric around zero in-plane magnetic field. As the sample is rotated one pair of transitions remains fixed relative to

the field strength, while the other moves. This shift in the location of the second flip proceeds regularly around the hysteresis curve as the sample is rotated.

### **Incoming Polarization Angle**

To determine whether this depends on the angle of incoming polarized light or angle of the magnetic field, the polarization was varied with a fixed sample while keeping the beam power constant, and a variety of plots compared as in Figure 5.3. The amplitude does change, but these plots are not calibrated for rotations and so small variations in intensity are expected as the power varies slightly. The shape and especially the location of the double magnetization flip can be seen to be consistent, indicating that changes in polarization relative to an easy axis are not the cause of the plot shape changes. The change in the location of this second magnetization transition is due to variations in the in-plane easy axis relative to the applied field, and modeling indicates that the transition is a flip in magnetization across one of the cubic anisotropy axes.

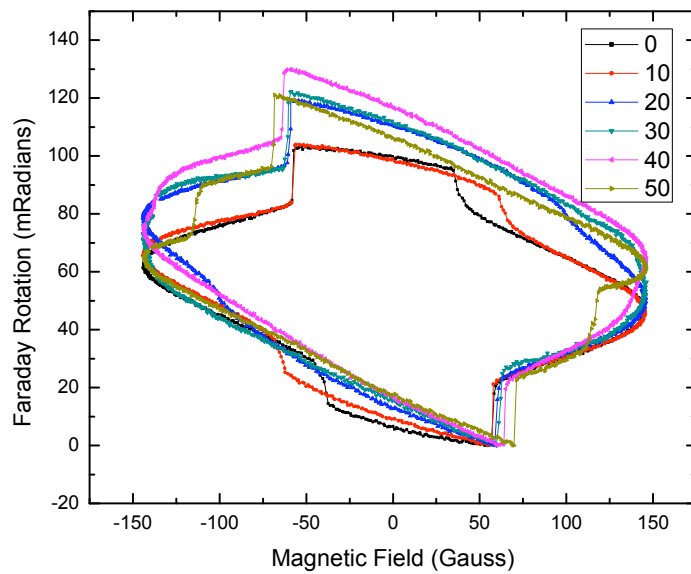


Figure 5.2: Hysteresis plots measured through the sample bulk, mounted at  $45^\circ$  to the incoming beam. The sample is rotated in degrees by the angles shown in the legend. The two pairs of magnetization transitions are visible.

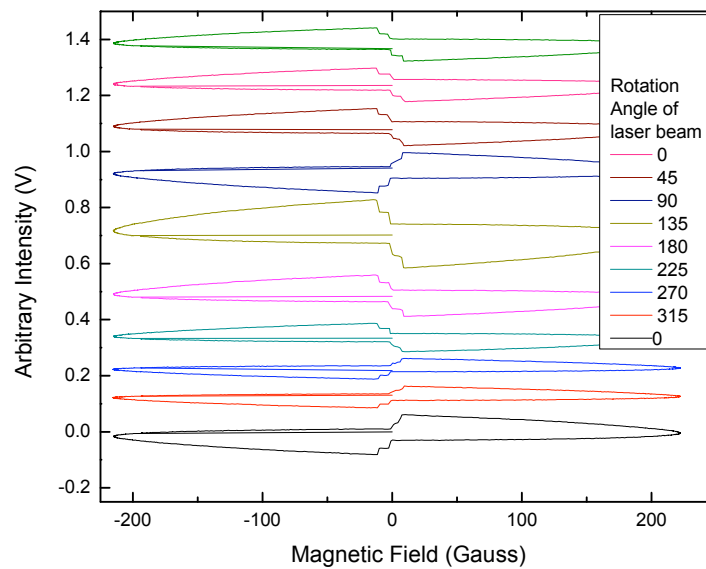


Figure 5.3: Plots showing that the angle of incoming polarization does not affect the hysteresis loop. The sample is mounted normal to the beam and the incoming polarization direction varied by the angles shown in the legend. The power incident on the sample is kept constant.

### 5.2.2 Hall Probe Position Effect

The Hall probe position varies relative to the sample depending on how the sample was mounted and also due to it not being possible, even with the same sample, to precisely duplicate its position. The magnetic field is not uniform, so all magnetic field values are approximate owing to the gap between the Hall probe and sample. This can change the shape of the plot enough to make quantitative comparisons difficult, as shown in Figure 5.4. Each plot was taken under identical conditions except for the movement of the Hall probe. This movement changes the general shape of the plot and apparent location in magnetic field of the important magnetization transitions, so comparisons between hysteresis loops are done with the Hall probe in as consistent a position as possible.

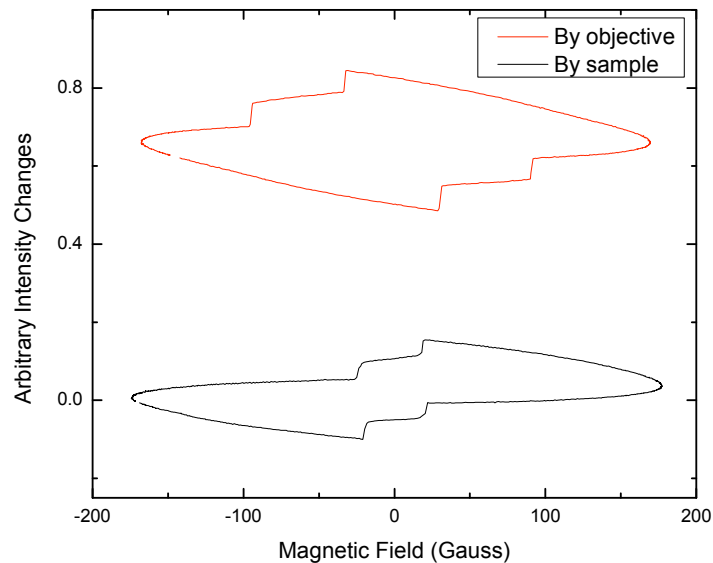


Figure 5.4: The position of the Hall probe can significantly affect the hysteresis plot shape. Moving the Hall probe from beside the sample  $\sim 2$  cm away places it in a different fringe field of the magnet. The field strength is roughly the same but the angle at which the field passes through the Hall probe has changed. This changes where in the magnets rotation the magnetization transition appears to occur.

Figure 5.5(a) shows the magnetic field in two directions and how its direction traces a circle. The magnitude of this field is shown in Figure 5.5(b).

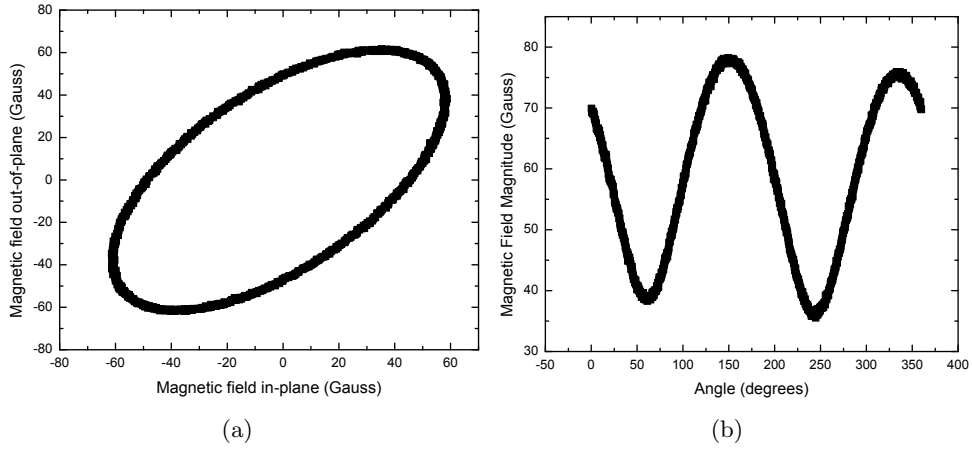


Figure 5.5: Plots showing the magnetic field at the sample. The field traces out a circle as the magnet rotates (a), and while the magnitude does not go through zero it varies significantly (b.) The second in-plane field is not measured here, but was found to remain small during magnet rotations and does not account for the full variation in applied field magnitude.

The hysteresis plots measured are very repeatable through a cantilever even after realignment of the beam. The beam is aligned to the maximum power through the cantilever, and so the position at which a curve is taken is usually similar. The cantilevers almost always show only two pairs of magnetization transitions which do not vary other than in intensity depending on precise alignment in the cantilever.

### 5.2.3 Differences Due to Laser Power

In the bulk sample of the sample the laser power has no noticeable effect on the Faraday rotation amplitude measured. (Figure 5.6.) The plot differences here are probably due to random errors in calibrating the Faraday rotation as there is no correlation between changes in Faraday rotation amplitude and power (Figure 5.9, bulk Sample.)

In a cantilever the power has a large effect on the hysteresis loop. The signal to noise ratio (SNR) and signal amplitude in volts of the un-calibrated hysteresis

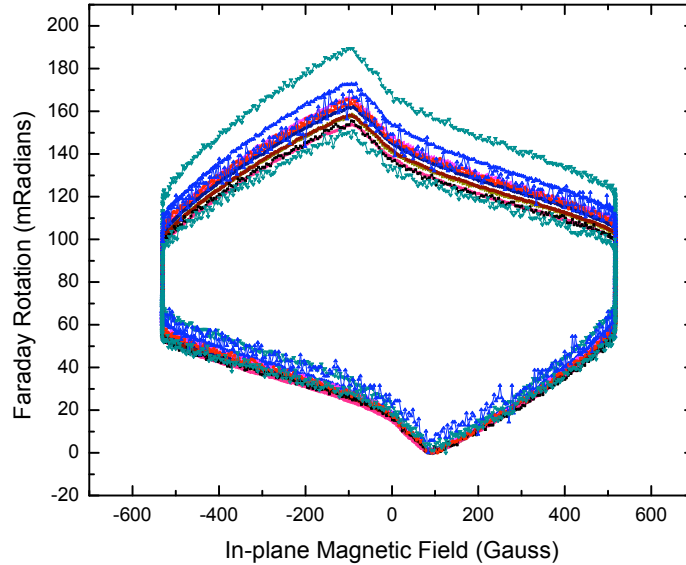


Figure 5.6: Hysteresis loops through the bulk sample at various laser powers measured before the focusing objective. The sample is mounted at  $45^\circ$ . The powers are: 3.12 mW, 2.48 mW, 2.28 mW, 1.96 mW, 1.95 mW, 1.40 mW, 0.94 mW, 0.80 mW, 0.38 mW, 0.36 mW, 0.078 mW, and 0.016 mW

loop increase with laser power, making it appear that higher power results in a larger Faraday rotation. However, after calibration the Faraday rotation is seen to decrease with increasing power, even as the SNL increases (Figures 5.7 and 5.8.) Plotting the maximum Faraday rotation amplitude vs power in Figure 5.9 shows how the rotation decreases with power for both cantilevers but faster for the thinner cantilever and stays constant for the bulk. We believe that heating of the sample causes it to be demagnetized. This would explain Figure 5.9 as the thicker cantilever has better thermal conductivity to the surrounding sample and does not get as hot as the thin cantilever. Below about  $400 \mu\text{Watts}$  into the focusing objective the Faraday signal was found to saturate and not increase with decreasing power even for the thinnest cantilever measured and so this power was used for subsequent measurements, allowing comparisons of the Faraday rotation between cantilevers of different thicknesses.

Low laser power and thin cantilevers both give signals with a poor SNR, so

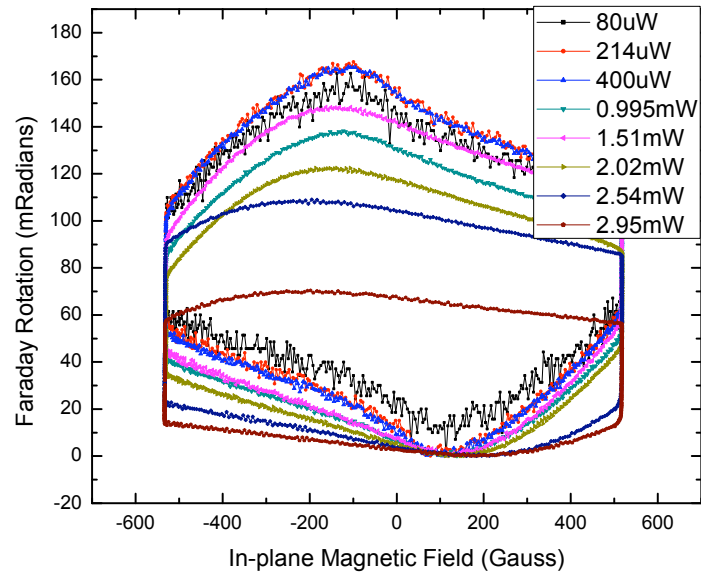


Figure 5.7: The Faraday rotation consistently decreases with increasing laser power through a  $4 \mu\text{m}$  thick cantilever.

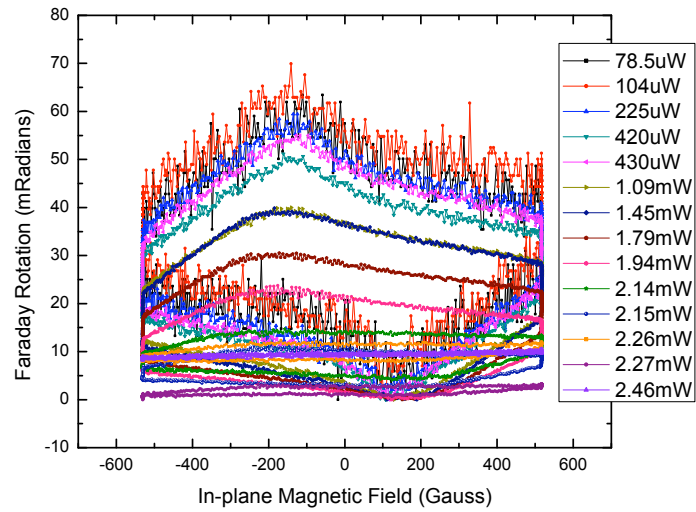


Figure 5.8: Hysteresis loops at different laser power into the focusing objective for a  $1.7 \mu\text{m}$  thick cantilever.

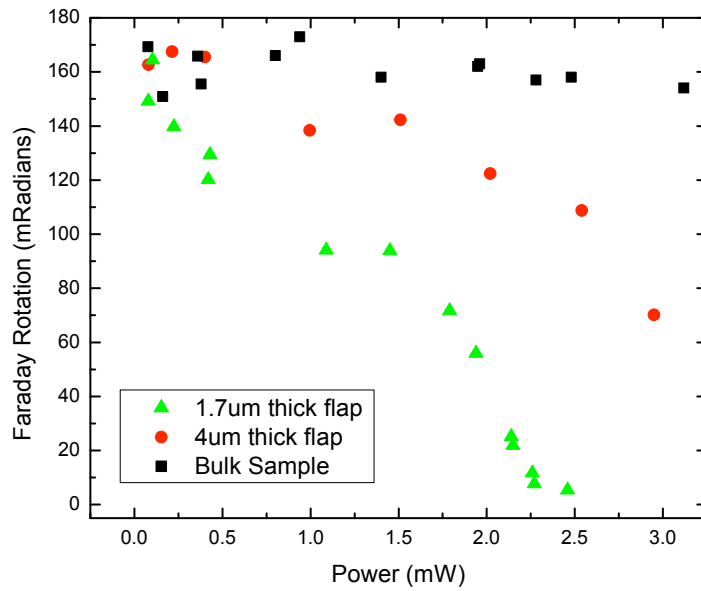


Figure 5.9: The maximum Faraday rotation amplitude as a function of power for the bulk sample and two cantilevers.

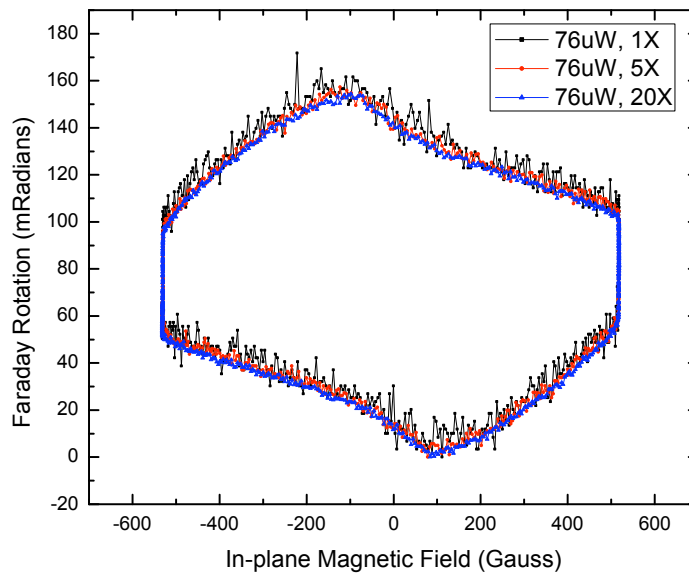


Figure 5.10: Averaging multiple hysteresis loops reduces the signal to noise ratio. A single rotation, 5 rotations, and 20 magnet rotation averages are shown. Typically 15 rotations were averaged.

averaging is sometimes needed to obtain a clear signal. As described in the characterization section this averaging is not simple to implement and was performed within the Labview program. Figure 5.10 shows that this averaging is working correctly by comparing a single hysteresis loop with averages of 5 and 20 loops. Some averaged plots of low SNR data show a double hysteresis loop that appears as plots are averaged together. This may be an artifact of the averaging method; however, as it does not always appear or stay the same shape this is doubtful. The noise in the Faraday signal is not uniform throughout a magnets rotation. The noise also changes depending on how fast the magnet is rotated, and is likely caused by mechanical vibrations in the experiment caused by the magnets rotation. If the magnet is exciting vibrations in either the cantilever or another component the beam may be shifting in a repeatable way giving the double pattern.

The strength of the magnetic field strongly affects a hysteresis plot's shape. While the in-plane magnetic field component against which these hysteresis loops are plotted shows a zero field, the magnitude of the field is always non-zero, and changes depending on the rotating magnets distance away from the sample. Figure 5.11 shows four hysteresis loops at high field, while Figure 5.12 shows the plots from the sample sample position at low fields. At the highest field there is almost no sudden magnetization switch. This corresponds to the field being strong enough to push the magnetization fully out-of-plane, preventing a flip. As the magnitude of the field is reduced by moving the magnet away from the sample, the magnetization is forced less into the sample plane leading to larger sudden magnetization flips. As the field magnitude is reduced close to zero, the magnetization flips completely in-plane, which was probably the cause of those hysteresis loops with no curved component.

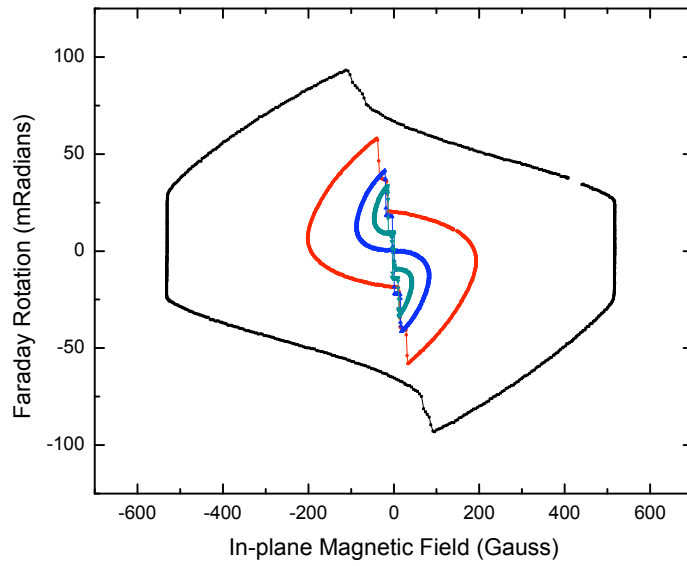


Figure 5.11: Multiple hysteresis loops taken at different heights of the magnet above the sample to give different magnitudes of the applied field. The beam is the bulk of the sample, mounted at  $45^\circ$ .

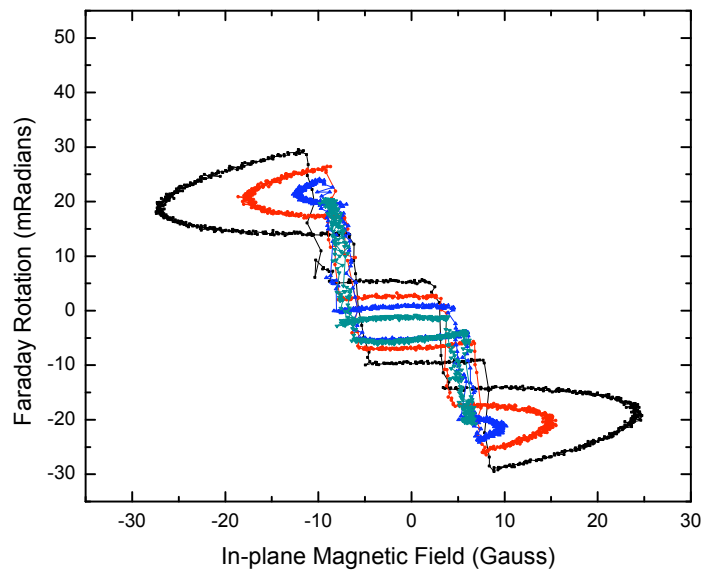


Figure 5.12: A continuation of Figure 5.11 at low field.

### 5.3 Evidence of Ion Damage

Any ion damage of the magnetization in the cantilevers is expected to manifest itself in either a reduction in the Faraday effect or a change in the shape of the hysteresis loops. Some of the  $\text{Ga}^+$  ions implant themselves a distance into the sample during milling that is dependent on their energy. If this changes the magnetization, it will manifest itself more as the cantilever gets thinner and the implanted region takes up a larger proportion of the cantilever. Hysteresis loops from a variety of cantilevers of different thicknesses are taken and compared to look for a reduction or change in the hysteresis shape. To do this, changes in beam energy are taken into account by calibrating the signal for rotation, and the plots are scaled to an equivalent cantilever thickness to account for the different Faraday rotation that will occur from cantilevers with different thicknesses. This equivalent scaled thickness is usually chosen as the thickness of the thickest cantilever measured, in this case  $4 \mu\text{m}$ .

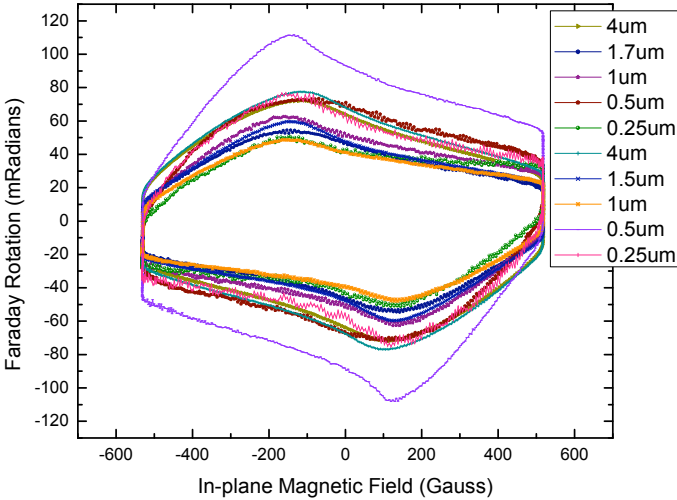


Figure 5.13: A variety of hysteresis loops through various thickness cantilevers shown in the legend. All Faraday rotations are scaled from the nominal thickness given to an equivalent thickness of  $4 \mu\text{m}$ . The differences in Faraday rotation amplitude do not correlate with cantilever thickness and are expected to be due to errors in the cantilever thickness measurements that were used to scale the data.

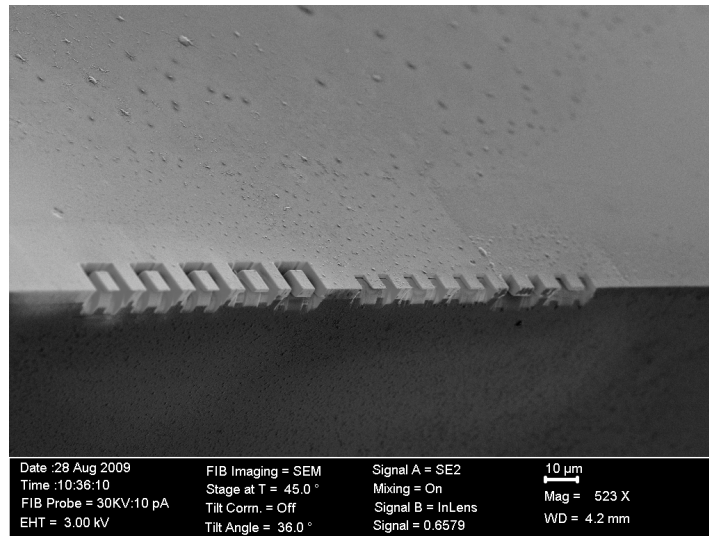


Figure 5.14: 10 LuIG cantilevers in two sets with thicknesses from 4  $\mu$ m to 250 nm. The set on the right are attached to the surrounding material through the LuIG film. The set on the left have had the LuIG film milled away around them to magnetically isolate them from the surrounding film. No change in the Faraday rotation was found between the cantilever sets.

Figure 5.13 shows the Faraday rotation through 10 cantilevers. All ten cantilevers here were milled from the same sample, in two sets of different thicknesses and geometries, and are shown in Figure 5.14. The right hand set looks like nine cantilevers, but this is five cantilevers with four sections between them with no undercuts. Both sets have similar thicknesses, ranging from 4  $\mu$ m to 250 nm. The left hand set have a milled trench at the back of them that is thicker than the LuIG layer. This is to try and magnetically isolate the cantilever from the surrounding LuIG to see if this affects the magnetization in any significant way, which was not seen. The sample was mounted at  $45^\circ$  to the beam, and the power was kept at 400 uW to prevent a reduction of the Faraday rotation from heating of the cantilevers.

No significant change in the magnetization with cantilever thickness can be seen in Figure 5.13. The flat edges on the left and right of the plots are from the Hall probe saturating. There are two peaks in the data, occurring at approx-

imately -139 gauss and 117 gauss. These are not symmetric about 0, possibly because the Hall probe is not at the same position as the sample. These peaks correspond to the locations where the magnetization vector is maximally forced into the sample plane. The lack of sudden transitions and the smooth rise and fall to the maximum and minimum rotation indicates that the applied field is strong enough to hold the magnetization aligned with it. All rotations have a similar shape, but there is a significant difference in the maximum Faraday rotation measured for different cantilevers. As this data is scaled to a 4  $\mu\text{m}$  equivalent thickness, we expect the differences to be at least partly due to inaccuracies in the thickness measurements. Half of the thicknesses of the cantilevers shown were measured from the end-on profile. This was later found to be a very inaccurate method of measurement as it is impossible to tell if the cantilever undercut has a significant slope to it or not. The FIB beam also rounds the cantilever end making the thickness of the cantilever unclear. The exact position where the beam passes through the cantilever is unknown, increasing the error in a sloped cantilever. Later cantilevers had their thickness measured from the side, giving a more accurate thickness measurement. Fig 5.15 shows the same set of cantilevers measured at a lower magnitude applied field. This field is not strong enough to hold the magnetization in alignment, and we see the sudden magnetization flips resulting at the same in-plane field strength as the maximum Faraday rotation found above. This corresponds to the transition of the magnetization vector through the hard axis in the into-plane direction. Other than the transition sharpness the curve is broadly similar to that in Figure 5.13 and to the bulk LuIG thin film signal at some angles. The order of the cantilevers by maximum Faraday rotation is the same as that in the high field case, as may be expected if this is due to thickness errors since the same cantilever thicknesses are measured. There is no noticeable change in the Faraday effect between those

cantilevers isolated from the surrounding LuIG plane, and those attached to it. A large number of different cantilevers were measured, consisting of the two above and also cantilevers parallel to the sample edge. Thicknesses from 150 nm to 4  $\mu\text{m}$  are plotted together in Figure 5.16. No reduction in the Faraday rotation with cantilever thickness could be seen in the corresponding Figure 5.17.

### Estimate of Ion Damaged Layer Thickness

If the ion implantation destroys the magnetization in a layer of thickness  $d$  in a cantilever of thickness  $t$ , this  $d$  could be found. The Faraday rotation  $\theta$  is proportional to the cantilever thickness minus the damaged layer thickness,

$$\theta = c(t - d) \quad (5.1)$$

$$\frac{\theta}{t} = c\left(1 - \frac{d}{t}\right) \quad (5.2)$$

Plotting  $\theta/t$  vs  $1/t$  the plot should be linear, and any slope corresponding to the damaged layer thickness. Figure 5.18 shows this relation, with a linear fit given. We can find  $c$  from the intercept to be  $19.2 \pm 2.2$  mRadians/micrometres. The slope is  $0.048 \pm 0.7$  mRadians =  $-c * d$ . From this we can estimate the upper bound of the damaged LuIG layer at 40 nm thick. The large error on the slope makes this result inaccurate, however the procedure will work for the next generation of cantilevers with well known thicknesses.

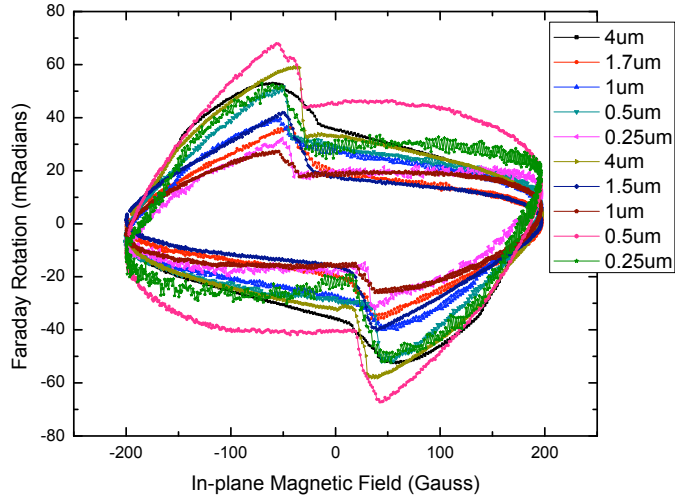


Figure 5.15: Scaled hysteresis loops at a lower field showing the abrupt magnetization transition. In addition to a decrease in Faraday rotation, any ion damage may change the shape of a hysteresis loop which may be most visible at the magnetization switches. Here some plots have a vertical transition, some a gradual slope, but there does not appear to be a correlation between cantilever thickness and the shape of the magnetization switch.

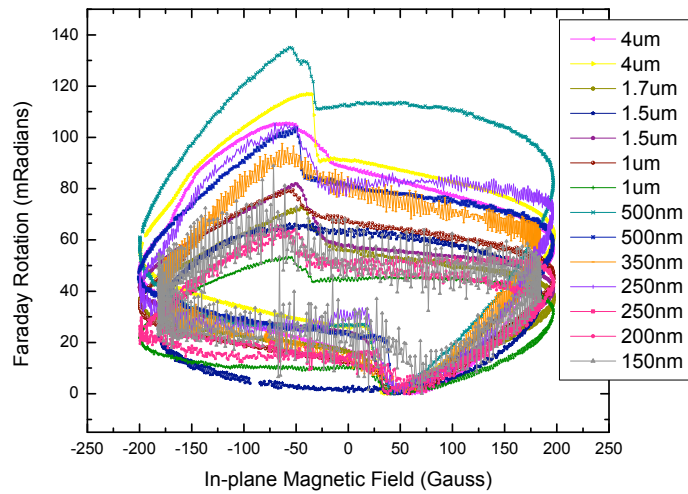


Figure 5.16: Scaled hysteresis loops for cantilevers ranging from 4  $\mu\text{m}$  to 150 nm, showing no obvious effect of ion damage.

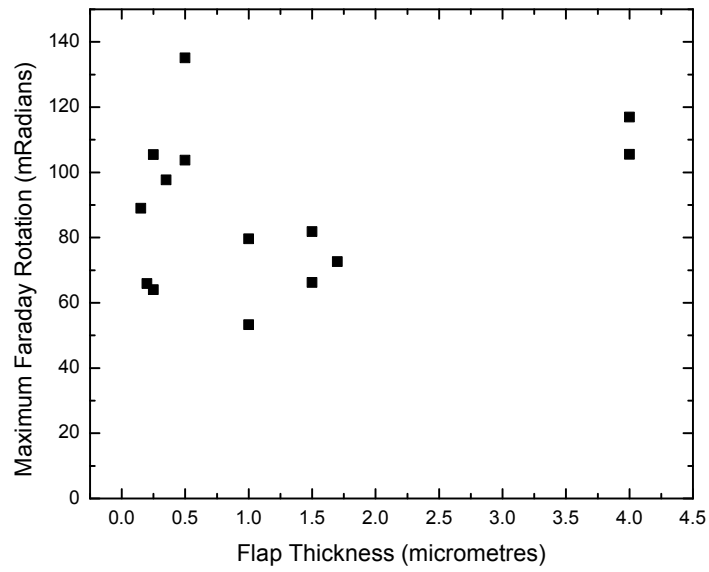


Figure 5.17: The maximum Faraday rotation of each hysteresis plot is scaled to the equivalent 4  $\mu\text{m}$  thickness and plotted vs the flap thickness. Any ion damage should be apparent as a reduction in the Faraday rotation with flap thickness.

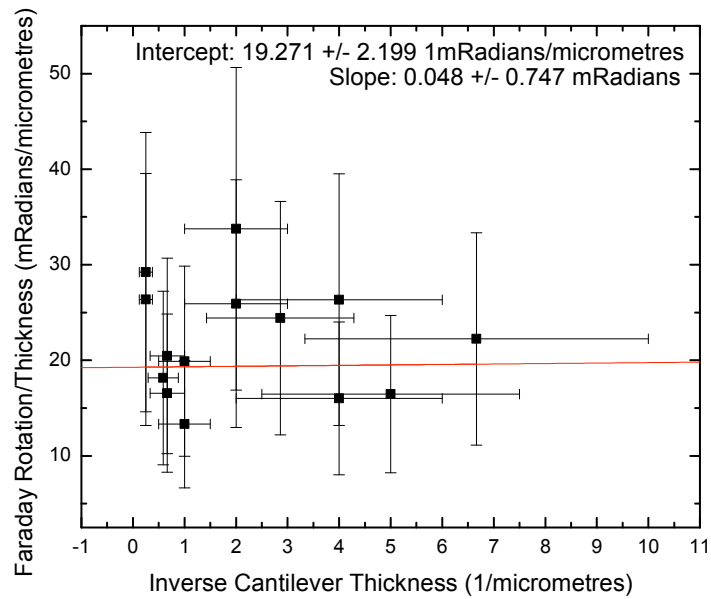


Figure 5.18: A plot of the unscaled Faraday rotation per thickness of LuIG vs the inverse cantilever thickness. The slope and intercept give an upper bound to the damaged thickness of 40nm. Error bars assume a maximum 50% flap thickness measurement error.

## Chapter 6

# Ferromagnetic Resonance

*Ferromagnetic resonances in lutetium iron garnet cantilevers and bulk material are demonstrated. Differences in the FMR resulting from the applied magnetic field, pulse generator, coil type, and orientation are discussed so that further investigations of the details of FMR in cantilevers can be investigated. Fast Fourier transforms of the FMR were used to compare the resonance frequencies.*

### 6.1 Ferromagnetic Resonance Overview

Studying magnetomechanical coupling in the method we have proposed will require an understanding of the magnetic and mechanical properties of NEMS cantilevers. Ferromagnetic resonance in these cantilevers is key to magnetomechanical coupling, and must be well understood. Towards this goal the experimental infrastructure for measuring pulsed FMR in cantilevers was set up, basic problems solved, and ferromagnetic resonance in cantilevers demonstrated. FMR was described in Chapter 1, and the pump-probe experimental technique for measuring it in Chapter 3.

## 6.2 Dither Field Generation

The strength of the FMR signal results directly from the quality of the dither field pulsed excitation. A small amplitude excitation will cause a small FMR amplitude, while a narrow bandwidth excitation may degrade the frequency response especially at high FMR frequencies, or add a linear offset such that the FMR ringing is not symmetric around zero. The dither field quality is determined by the pulse generator, connections between the pulse generator and coil, and by the dither coil design itself. The pulse shape was not found to differ significantly between using the 50 V and 10 V pulse generators when tested in LuIG. The pulse shape was measured with a CT6 current probe, and the FMR ring downs recorded in bulk LuIG at a bias field of 151 gauss are shown in Figure 6.1. The FMR amplitude is different between the pulse generators, but after scaling the 10 V signal such that its initial excitation amplitude matches that of the 50 V signal we see that both pulse generators produce similar FMR ring downs. The 50 V and 10 V FMR signals were not as similar when measured in a bias field of 2000 gauss, shown in Figure 6.2. Here the 10 V pulse generator produced a signal with higher time resolution, shown in the greater difference between the initial peak and trough after excitation and in the ringing continuing for longer. The FMR ring down is not purely a function of the dither field excitation amplitude, but is expected to depend on the bandwidth of the current pulse. High frequency components of the current pulse will be required to excite the highest frequency FMR ring downs which occur at high bias fields. The 10 V pulse generator has a higher bandwidth and this may be causing the superior time resolution compared to the 50 V pulse generator, allowing us to resolve the trough between initial peaks. The 50 V pulse generator generates the current pulse internally which then propagates through around 3 feet of 50  $\Omega$  coaxial cable to the dither coil. The 10 V pulse generator generates the current pulse in a small attach-

ment at the end of the 3 feet of coaxial cable which can be connected directly to the dither coil. Reducing the cable length and thus dispersion within it may help increase the bandwidth and FMR resolution. For most FMR measurements made the bias fields were low enough that the bandwidth did not appear to be a problem, and the SNR was also low, causing us to use the 50 V pulse generator.

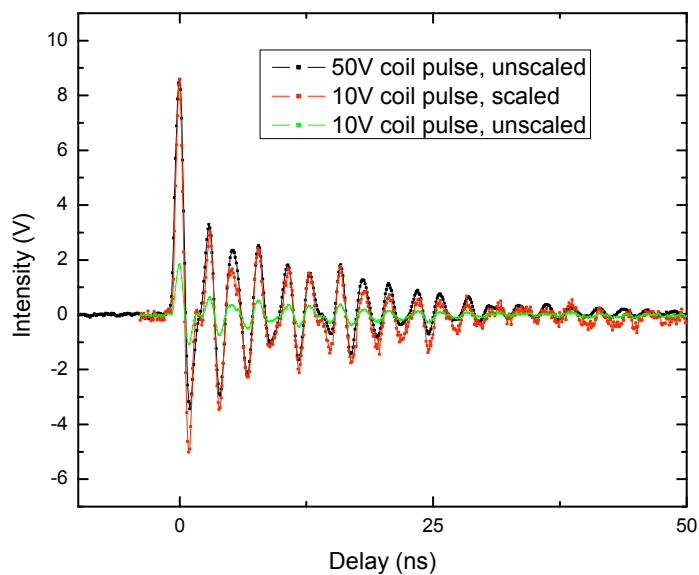


Figure 6.1: FMR ring downs in LuIG mounted normal to the beam. The 50 V and 10 V pulse generators are used with the 30 gauge (thick) dither coil at a bias field of 151 gauss. In the “scaled” plot the excitation is scaled such that the initial excitation between the 50 V and 10 V coil is the same.

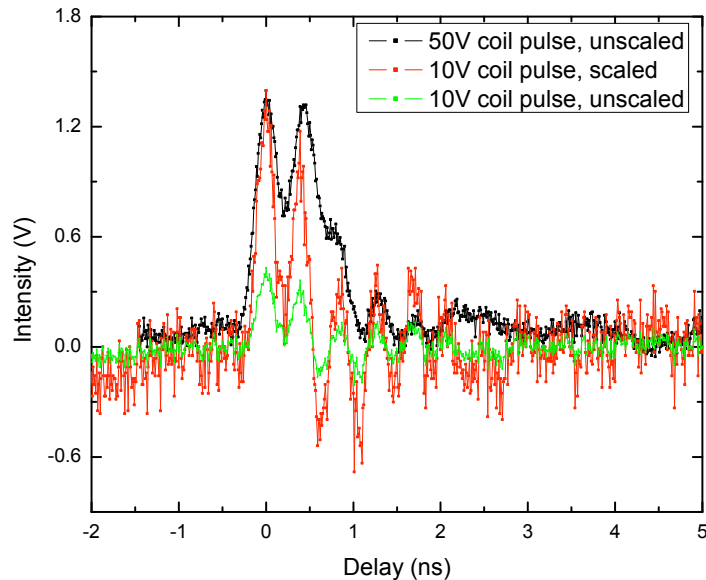


Figure 6.2: FMR ring downs in LuIG mounted normal to the beam. The 50 V and 10 V pulse generators are used with the 30 gauge dither coil at a bias field of 2000 gauss. In the “scaled” plot the excitation is scaled such that the initial excitation between the 50 V and 10 V coil is the same. The higher time resolution of the 10 V pulse generator is apparent in the larger drop in intensity after the initial peak.

### Current Pulse Reflections

Reflections in the current pulse have been observed with the CT6 current probe, and as a second smaller excitation in the FMR ring down. With the first dither coil made this reflection occurred  $\sim 30$  ns after the primary excitation. This significantly disturbed the FMR ring down. Changing the coaxial cable lengths and removing the CT6 current probe and attenuator only shifted the location of the secondary excitation, and from the cable lengths tried it appeared that the secondary excitation was reflecting back along the coaxial cable, off the pulse generator, and back along the coaxial cable into the dither coil. Long lengths of coaxial cable can delay the secondary FMR excitation’s arrival far enough away from the primary FMR excitation that it is not not relevant; however the extra dispersion from the long cable is expected to cause problems with exciting

high frequency FMR. In the end a second dither coil was made after which the secondary excitation and a linear offset in the ring down disappeared, so any extra excitations are likely due to a poorly terminated coil rather than reflections off other components before the dither coil itself. The attenuator and CT6 current probe were not used for the final FMR measurements.

### **6.2.1 In-plane and out-of-plane field FMR measurements**

The next generation of pulsed FMR and hysteresis loop measurements should incorporate a Hall probe built into the sample holder so that the field can be directly measured as close to the sample as possible. In this experiment the field was measured at the position of the sample with the sample removed, and the field strength calibrated to the magnet height. All measurements here were made in this way, from the calibrated magnet height, rather than measured directly. The in-plane and out-of-plane fields were found from rotating the magnet  $45^\circ$  clock-wise and counter-clock-wise to change the field direction at the sample. This was most accurate at high field, and the in-plane and out-of-plane field measurements are only approximate as a result.

### **6.2.2 Dither Coil Construction**

Several dither coils were made. An ideal dither coil has a large core to allow the beam through, a small coil core to give a high field normal to the surface, low inductance and capacitance to give a high bandwidth, and excellent impedance matching with the coaxial cable to reduce reflections. Initially the coaxial cable from the pulse generator was connected to a small transmission line on a circuit board. A  $50\ \Omega$  surface mount resistor connected one of the SMA connector pins to the transmission line, and a small loop of wire at the end of the transmission line formed the coil itself. This geometry easily generated a high SNR FMR ring

down; however the secondary reflection and linear offset in the ring down caused problems. The relatively large distance between the 50  $\Omega$  terminator and coil, as well as the unnecessary extra pair of connections and the silver paint used instead of soldering, may all have caused problems.

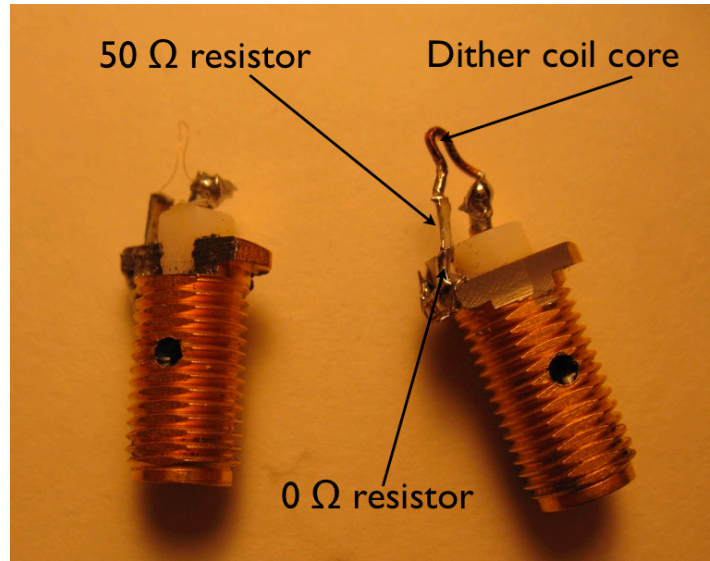


Figure 6.3: Two of the dither coils used. These are the thick and thin wire coils referred to in this chapter, made from 30 gauge (0.010" wire) and 0.001" magnet wire. The core is the gap in the loop of wire through which the laser passes.

A second coil was made with a small loop of 30 gauge wire soldered directly onto a SMA connector with a solder pin. (Figure 6.3). A 0  $\Omega$  and 50  $\Omega$  surface mount resistor were stacked and soldered together to produce two solder points close to each other that the wire loop could be soldered onto. The SMA connector was milled away on one side to allow it to closely approach the sample while missing the objective lens. This geometry worked well but the thick wire prevented the beam from completely passing through the center of the coil when tilted at 45°.

A third coil was made with 0.001" diameter magnet wire soldered on a SMA connector with a surface mount 50  $\Omega$  terminating resistor. This dither coil pro-

duced a much larger FMR signal, Figure 6.4. Some of this larger signal is because the small wire was able to be brought closer to the sample surface. The low coil profile also allowed the beam to completely pass through when the sample was tilted to  $45^\circ$ . The FMR ring down produced by this thin coil shows more complexity to the ringing than from the thick coil. It is unclear why, perhaps the small coil has a higher bandwidth or the larger excitation allows subtleties of the FMR to be observed.

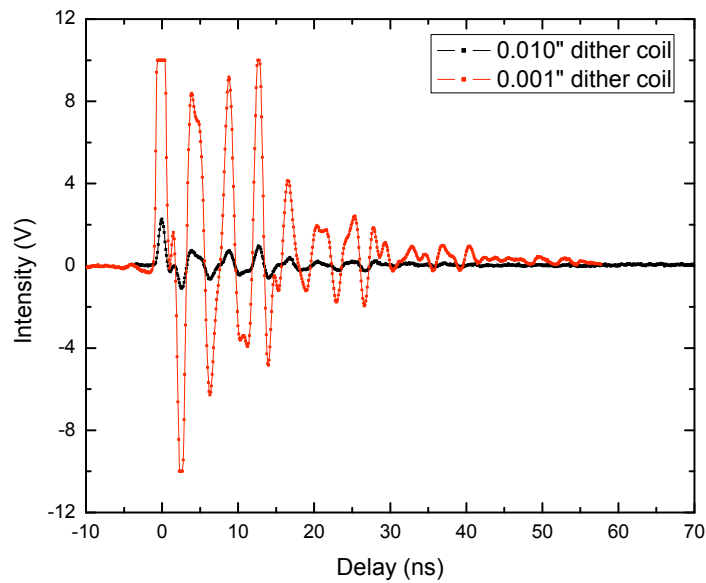


Figure 6.4: The difference in excitation between the thick, 0.010", 30 gauge dither coil and the thin 0.001" dither coil with the 10V pulse generator. The bias field is 30 gauss. Note that the thin coil has saturated the detector setup and the initial excitation is clipped.

### 6.3 Ferromagnetic Resonance in bulk LuIG

In bulk LuIG the FMR ring down changes as the sample is rotated at normal incidence to the beam, around the beam axis, Figure 6.5. Changes in hysteresis loop shape were not seen as the sample was rotated in the same way in Figure 5.1. Changes in the FMR shape may be due to the FMR precession where the mag-

netization vector may rotate through the anisotropy axes, and the shape effected by the angle between the precession direction (applied field) and anisotropy axis. This will not happen in the hysteresis loop case where the magnetization rotation is closer to lying in a plane.

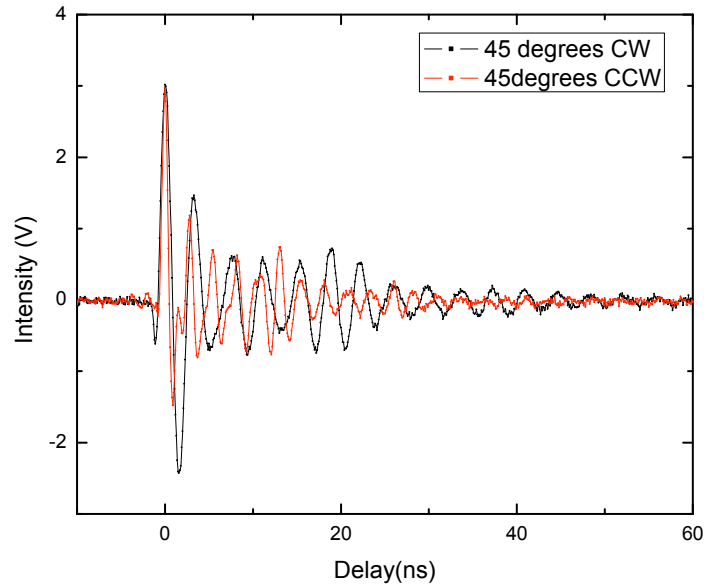


Figure 6.5: FMR plots taken with the sample mounted normal to the beam and rotated by the given angles around the beam axis. The FMR shape changes depending on the angle, an effect that was seen at other rotation angles and field strengths. 10V pulse generator, thick dither coil, 151 gauss field.

## 6.4 Fast Fourier Transforms of FMR

The frequencies of FMR were found from fast Fourier transforms (FFT's) of the ring downs. A typical FFT and FMR curve of thin film LuIG is shown in Figure 6.6. Here there is a primary frequency of the ring down with various other modes contributing. The entire FFT spectrum shifts with applied field, as in Figure 6.8. Plotting the frequency of the primary and 5th mode for this we have Figure 6.9. The theoretical FMR frequencies for a material with saturation magnetization  $M_s = 0$ , and  $4\pi M_s = 1760$  gauss for YIG at room temperature, are shown. No

value of saturation magnetization will fit the measured FMR frequencies, and Kittel formula will have to be modified to apply to LuIG. Similar results are found with a different sample and dither coil, where the primary FMR mode produces Figure 6.10. The FMR frequency is linear with applied field until close to zero field where the frequency reaches a minimum of around 240MHz. If we assume that the anisotropy is small then the Kittel formula (1.6) should apply. Plotting  $f^2/H$  vs  $1/H$  we can find  $M_s$  from the slope and intercept.

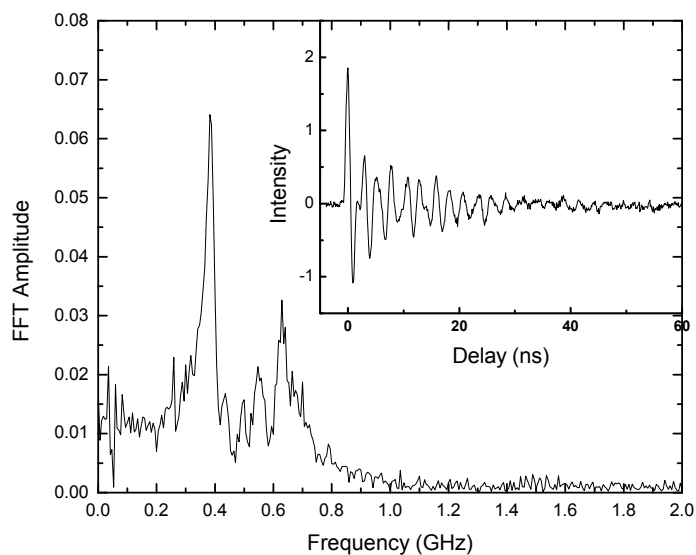


Figure 6.6: A FFT of a typical FMR curve in a bulk LuIG film mounted normal to the beam, taken at a 151 gauss in-plane bias field with the 10V pulse generator. The FMR curve is shown in the inset.

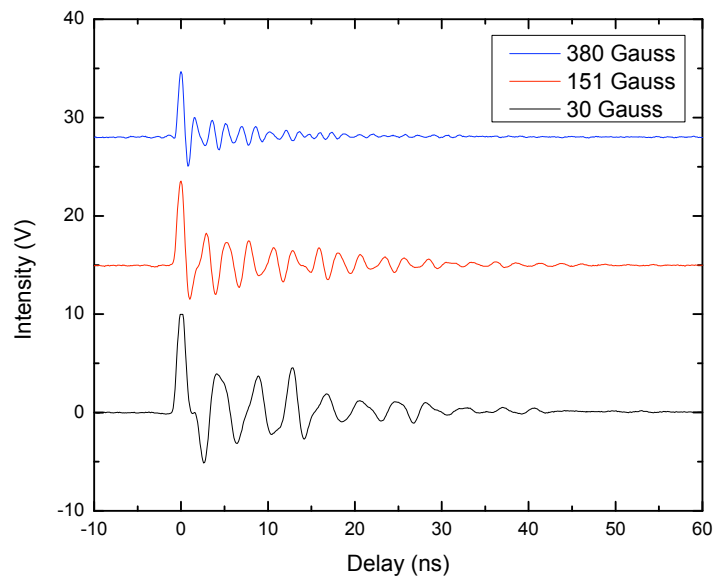


Figure 6.7: The FMR of a bulk LuIG film mounted normal to the beam. The applied fields are calculated from a calibration of the magnet position, not measured directly. The corresponding FFT's are shown in Figure 6.8.

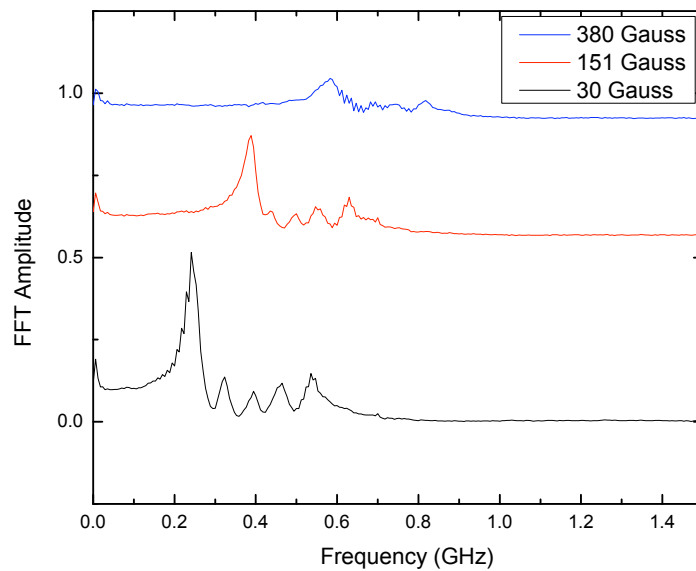


Figure 6.8: FFT spectrums of a bulk LuIG film mounted normal to the beam. The applied fields are calculated from a calibration of the magnet position, not measured directly.

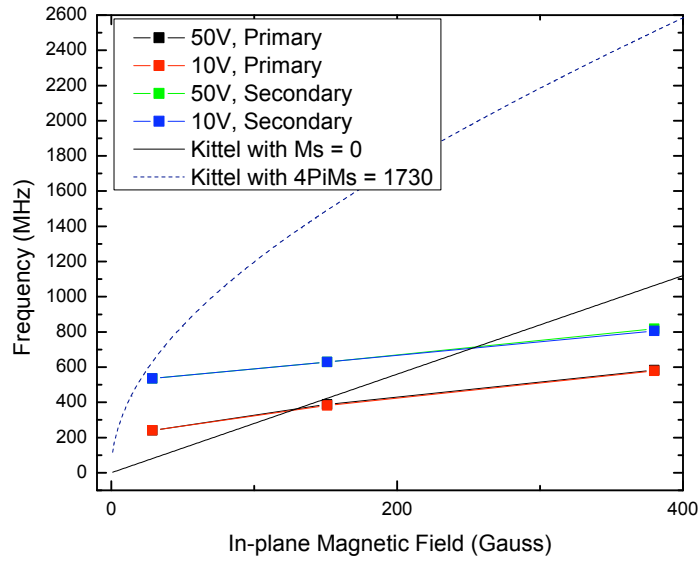


Figure 6.9: The primary FMR frequency and the that of the 5th mode (5th FMR peak, labeled secondary in this figure) plotted vs field strength for two different pulse generators. The field is calculated from a calibration of the magnet position, not measured directly. The solid line is a calculated from the Kittel FMR equation 1.6 with a saturation magnetization  $M_s = 0$ , and the dashed line with  $4\pi M_s = 1760$  gauss, the value for YIG at room temperature.

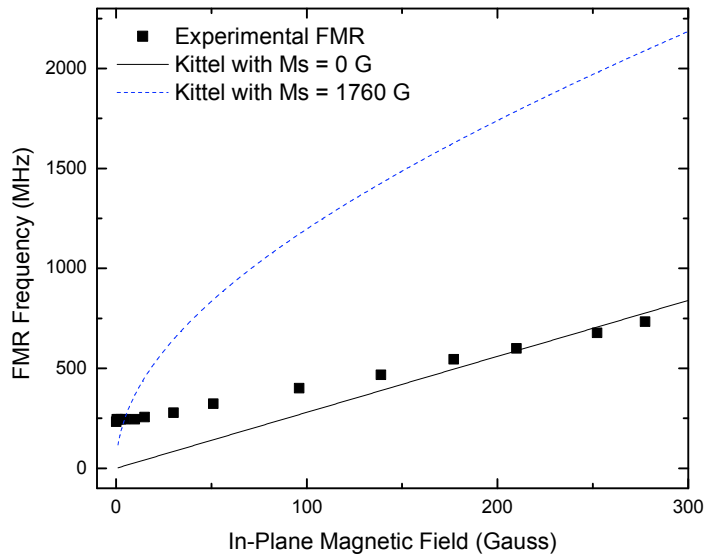


Figure 6.10: The primary FFT frequencies of a bulk LuIG film at various measured field strengths. The sample is mounted normal to the beam. In the bulk material this frequency increases close to linearly with the applied field, and reaches a minimum in zero applied field of approximately 240MHz. The expected FMR frequencies from the Kittel FMR formula 1.6 are shown with the saturation magnetizations  $M_s$  used.

## 6.5 FMR of 45° Mounted LuIG

Tilting the LuIG sample to 45°, as is required for analyzing the cantilevers, changes the FMR ring down. Figure 6.11 shows that the FMR shape changes as the sample is tilted, and that this change remains even after the applied field has been realigned in the sample plane. The dither coil has been tilted to continue to apply the dither field normal to the sample surface. The FFT of these FMR ring downs (Figure 6.12) show that the contribution of the first mode is significantly reduced so that the all five primary modes contribute approximately equally.

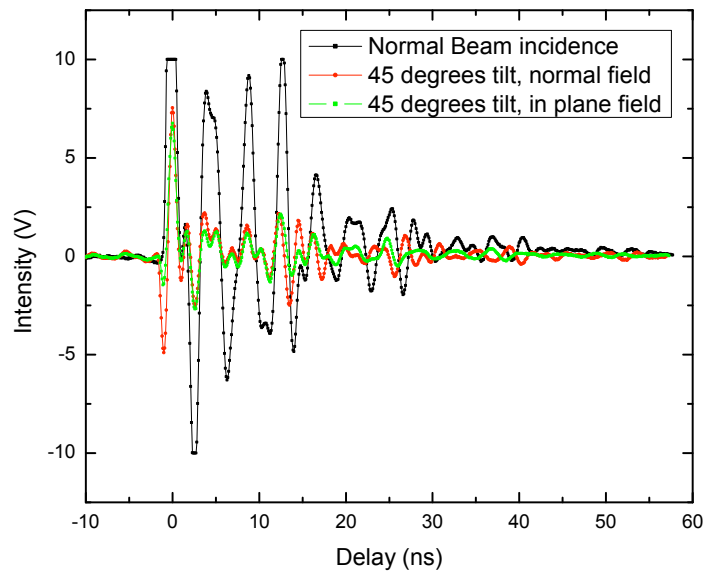


Figure 6.11: FMR through bulk mounted normal to the beam and tilted at 45°, with a bias field of 30 gauss. When at normal incidence the applied field is in-plane, and after tilting the sample the FMR was measured both with the field in-plane and out-of-plane (normal field.)

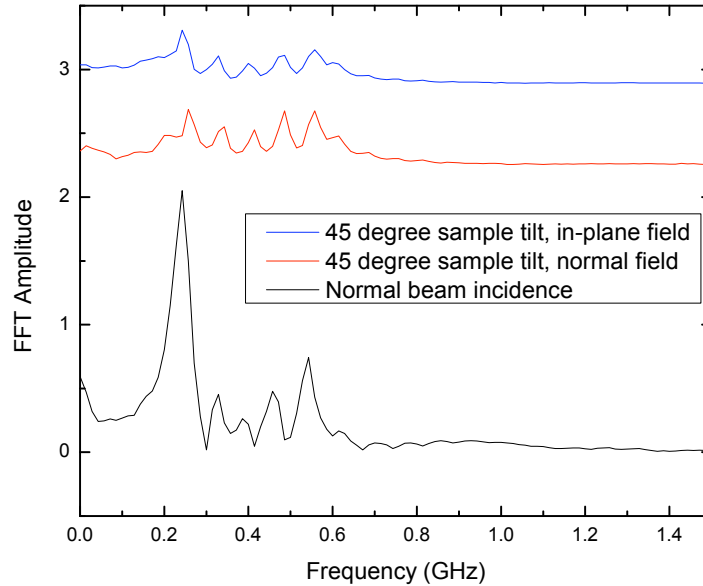


Figure 6.12: FFT's of bulk LuIG at normal beam incidence and tilted to  $45^\circ$ . The FMR curves for these plots are shown in Figure 6.11.

## 6.6 FMR in LuIG Cantilevers

In Figure 6.13 the beam is focused through a  $1.7\mu\text{m}$  thick cantilever. After obtaining the first FMR plot the sample was moved and the beam was refocused through the cantilever to obtain the second FMR plot, showing the repeatability of the FMR. The FMR ring down is complex like that of bulk LuIG mounted at  $45^\circ$ , but unlike in the bulk material Figure 6.14 shows the FMR shape can be seen to vary significantly depending on the direction of the applied field. The variation in FMR with applied field direction is also apparent in other cantilevers and at different field strengths, as in Figure 6.15.

Figures 6.16 and 6.17 show the FMR through four cantilevers at 28.7 gauss and 151 gauss, respectively. FMR in cantilevers below 500 nm thick was too small to measure. The FMR pattern changes with cantilever thickness, and in particular the damping appears to change in addition to the signal amplitude. The FFT of these plots are shown in Figures 6.18 and 6.19. Like the  $45^\circ$  tilted

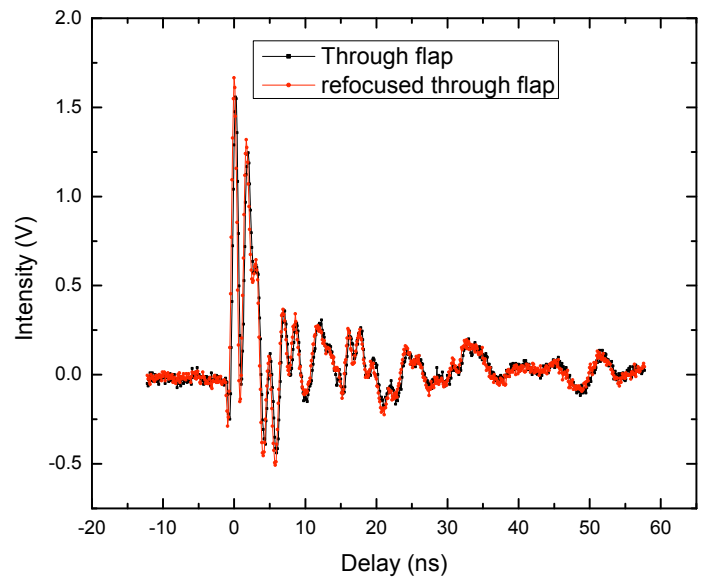


Figure 6.13: Typical FMR curve taken through a  $1.7\mu\text{m}$  thick cantilever at a bias field of 30 gauss. FMR is repeatable in cantilevers with the same orientation and field.

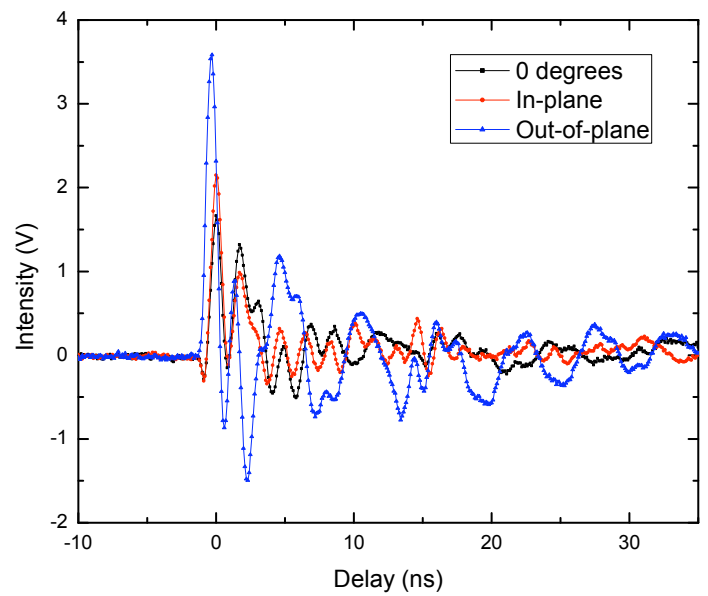


Figure 6.14: FMR taken through a  $1.7\mu\text{m}$  thick cantilever at 30 gauss bias field. FMR varies significantly depending on the bias field's direction.  $0^\circ$  here is the field applied half way between in-plane and out-of-plane.

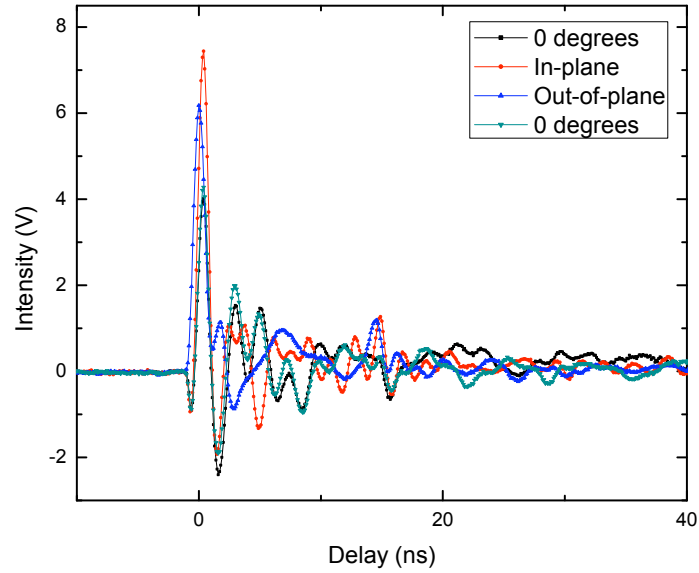


Figure 6.15: FMR in a  $4\mu\text{m}$  thick cantilever at a 151 gauss bias field.

bulk film sample there is no single primary mode, although unlike the tilted bulk it is difficult to identify clear modes. There is some similarity between the FFT's of individual cantilevers at different fields strengths, indicating that the FMR ring down is strongly dependent on cantilever shape and thickness as opposed to primarily the bias field strength. The lack of a clear resonant frequency makes it difficult to see trends in the FMR with field strength in cantilevers.

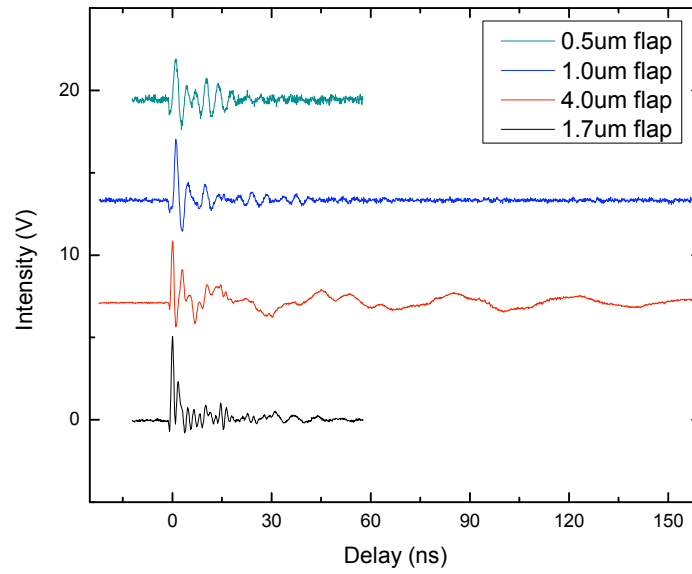


Figure 6.16: FMR at 30 gauss bias field through various cantilever thicknesses. These cantilevers are milled from the sample and are spaced  $\sim 15 \mu\text{m}$  apart.

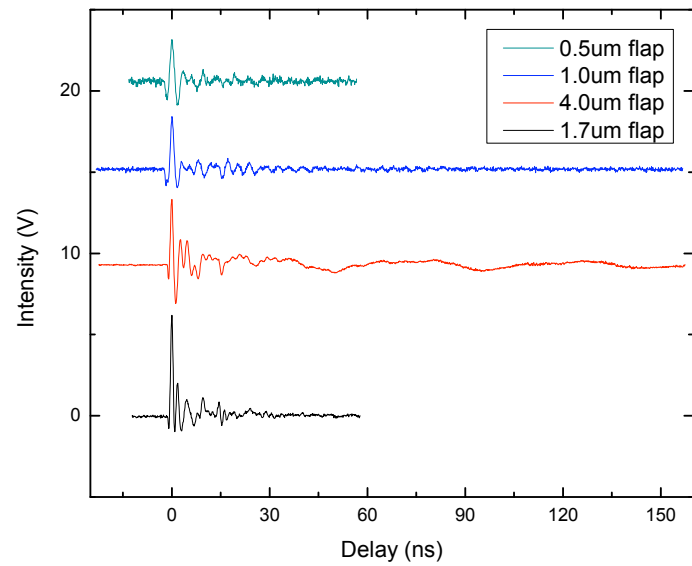


Figure 6.17: FMR at 151 gauss bias field through various cantilever thicknesses.

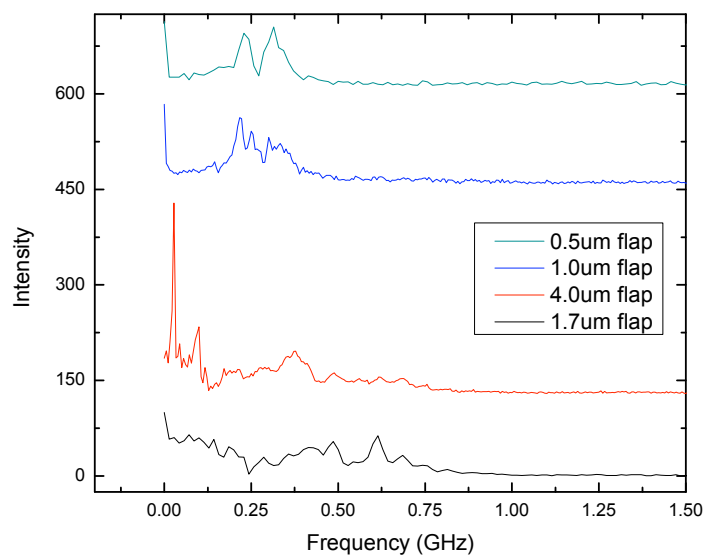


Figure 6.18: FFT's of the FMR in Figure 6.16, 30 gauss field.

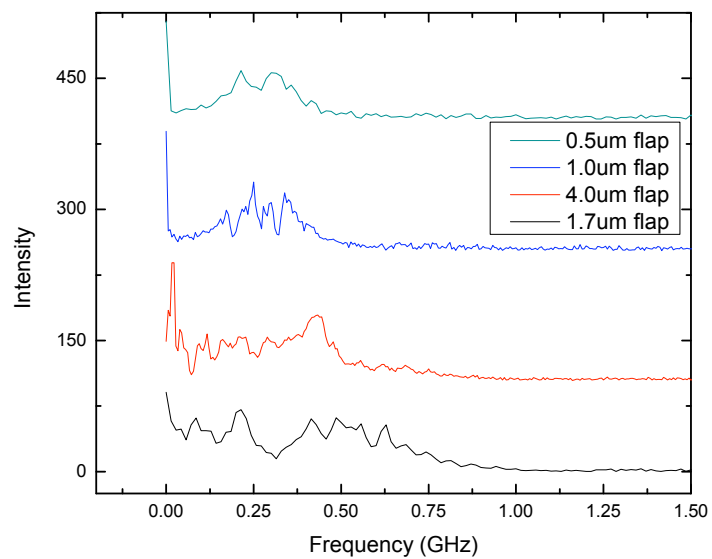


Figure 6.19: FFT's of the FMR in Figure 6.17, 151 gauss field.

## Chapter 7

# Conclusion

A procedure for milling lutetium iron garnet cantilevers, double clamped beams, and paddle structures with a focused ion beam microscope was developed. Making these structures suitable for measuring hysteresis loops and ferromagnetic resonance is discussed, along with the considerations for eventual mechanical measurements and magnetomechanical coupling.

The experimental setup for rotational hysteresis loops was designed and used to demonstrate that LuIG cantilevers are magnetic without any significant ion damage from FIB milling. Modeling of the hysteresis loops was used to show the origin of their shape from the sample's anisotropy and orientation and thus opens up a possible method for eventually characterizing a samples anisotropy. Ferromagnetic resonance in LuIG cantilevers was demonstrated. Subsequent efforts towards studying magnetomechanical coupling can build on this research.

The procedures used to mill and analyze LuIG cantilevers are applicable to other materials, including other magnetic garnets. The behaviour of ferromagnetic resonance in LuIG thin films needs to be investigated, and the role of the anisotropy understood so that a form of the Kittel FMR frequency formula can be found that applies to LuIG. This can be done initially by recording how the

FMR frequency varies with applied field, for different rotations of the sample around the beam axis. The rotational hysteresis loop method can also be developed further and, with an improved method of modeling the cubic anisotropy, can be used to obtain the specific orientation and strengths of the anisotropy axes. Accurately measuring the applied field at the sample will be necessary for this, either with a careful calibration of the field before the sample is mounted or with a 3-axis Hall probe integrated into the sample holder. Ideally this sample holder will allow easy rotation of the sample around the beam axis.

The ferromagnetic resonance measurements are currently limited to thicker flaps than we can measure hysteresis loops in. These FMR measurements can be improved by upgrading the focusing and collimating optics. A pair of longer focal length and high numerical aperture objectives will be especially useful for resolving small cantilevers and insuring that all the beam power passes through the flap and is re-collimated.

Studying magnetomechanical coupling in cantilevers would ideally require a way of making sequential mechanical and ferromagnetic resonance measurements in the same sample so that the results can be directly compared. The experimental setup used in this thesis was designed with that in mind, and would require few modifications. The principle change is to take hysteresis loop and FMR measurements in reflection instead of the current transmission through the sample, (Figure 7.1.) This may be possible by milling a cantilever and then using a directional deposition to coat the cantilever undercut with a mirror as in Figure 7.1. A second milling could be used to remove the mirror layer from the cantilever top/bottom as required, and we have demonstrated reflection measurements of thin film LuIG before. Hysteresis loops and FMR can be taken as before using the rotational magnet and dither coil. Mechanical measurements would use the undercut mirrored bottom and cantilever top face to form an interferometric cav-

ity to measure mechanical displacements of the cantilever, a procedure our group has used before. [16] This requires an actuation method, several of which, such as piezoelectric and magnetic, our group has demonstrated. It may be possible to use the dither coil for both FMR and mechanical actuation.

If we are able to characterize the effect of mechanical actuation on the FMR, or are able to take FMR without mechanically actuating the sample, then magnetomechanical coupling may be detectable at a frequency overlap. For example a splitting or change in the FMR frequencies, or an increase or decrease in FMR damping that occurs only at a frequency overlap, may indicate magnetomechanical coupling.

It may also be possible to detect mechanical coupling by first characterizing the mechanical response of the cantilever, and then measuring FMR in transmission at various applied bias fields, and thus FMR frequencies. Changes in the FMR, such as increased damping, that occur only at mechanically resonant frequencies may indicate a magnetomechanical coupling if the mechanical effects can be accounted for.

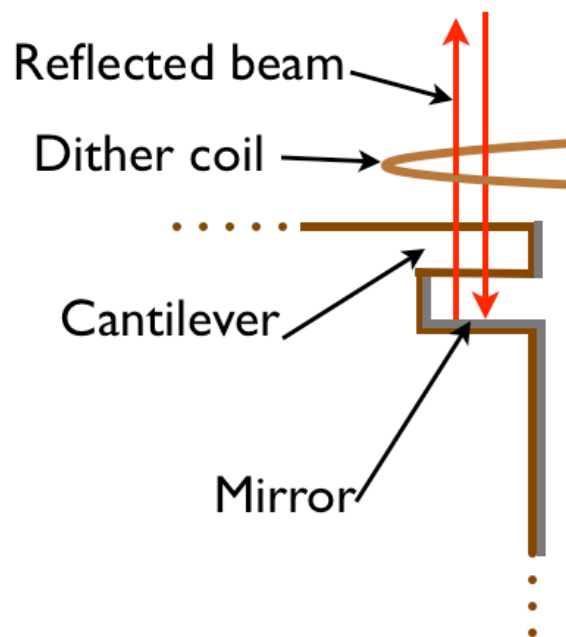


Figure 7.1: Proposed setup for combined hysteresis loop, FMR, and mechanical measurements. The Faraday effect and mechanical actuation is measured through the flap in reflection off a mirror deposited on the bottom of the undercut, which forms an interferometric cavity with the top face of the cantilever.

# Bibliography

- [1] R. P. Cowburn. The attractions of magnetism for nanoscale data storage. *Philosophical Transactions: Mathematical, Physical and Engineering Sciences*, 358(1765):281–301, 2000.
- [2] G. W Qin, Y. P Ren, N Xiao, B Yang, L Zuo, and K Oikawa. Development of high density magnetic recording media for hard disk drives: materials science issues and challenges. *International Materials Reviews*, 54(3):157, 2009.
- [3] Y. T. Yang, C. Callegari, X. L. Feng, K. L. Ekinici, and M. L. Roukes. Zeptogram-scale nanomechanical mass sensing. *Nano Letters*, 6(4), 2006.
- [4] Yuan Ma. Microelectromechanical systems (mems) based wavelength-selective building block in a transparent network architecture. *Communication Networks and Services Research Conference*, pages 326–330, 2008.
- [5] I-Ta Tseng Chia-Ling Wei, Chien-Fu Lin. A novel mems respiratory flow sensor. *IEEE Sensors*, 10(1):16–18, 2010.
- [6] D. Rugar, R. Budaklan, H. J. Mamin, and B. W. Chul. Single spin detection by magnetic resonance force microscopy. *Nature*, 430, 2004.

- [7] A.A. Kovalev, G.E.W. Bauer, and A. Brataas. Magnetomechanical torques in small magnetic cantilevers. *Japanese Journal of Applied Physics*, 45:3878–3888, 2006.
- [8] A.A. Kovalev, G.E.W. Bauer, and A. Brataas. Nanomechanical magnetization reversal. *Physical Review Letters*, 94:167201, 2005.
- [9] A.N. Cleland. *Foundations of Nanomechanics: from Solid-State Theory to Device Applications*. Springer/Verlag, 2003.
- [10] J. Prescott. *Applied Elasticity*. Dover Publications, 1946.
- [11] W. Hiebert. *Ferromagnetic Resonance in a Permalloy Microstructure Using Time Resolved Scanning Kerr Effect Microscopy*. M.Sc. Thesis, University of Alberta, 1998.
- [12] Zhigang Liu. *Micromagnetic simulations on Ni80Fe20 thin film microstructures*. M.Sc. Thesis, University of Alberta, 2003.
- [13] A. Paoletti. *Physics of magnetic garnets*. North-Holland Publishing Company, 1978.
- [14] S. Blundell. *Magnetism in Condensed Matter*. Oxford university press, 2001.
- [15] R. C. Hibbeler. *Mechanics of Materials, Seventh Edition*. Prentice Hall, 2008.
- [16] N. Liu, F. Giesen, M. Belov, J. Losby, J. Moroz, A. E. Fraser, G. McKinnon, T. J. Clement, V. Sauer and W.K. Hiebert, and M.R. Freeman. Time-domain control of ultrahigh-frequency nanomechanical systems. *Nature Nanotechnology*, 3:715, 2008.

- [17] Oleksiy Svitelskiy, Vince Sauer, Ning Liu, Kar-Mun Cheng, Eric Finley, Mark R. Freeman, and Wayne K. Hiebert. Pressurized fluid damping of nanoelectromechanical systems. *Physical Review Letters*, 103:244501, 2009.
- [18] Lali Kalandadze. Influence of implantation on the magneto-optical properties of garnet surface. *IEEE Transactions on Magnetics*, 44(11):3293–3295, 2008.
- [19] D. Ozkaya L, R. M. Langford, W. L. Chan, and A. K. Petford-Long. Effect of ga implantation on the magnetic properties of permalloy thin films. *Journal of Applied Physics*, 91(12):9937–9942, 2002.
- [20] P. Gerard. Ion implantation in magnetic garnet. *Nuclear Instruments and Methods in Physics Research*, 19:843, 1987.
- [21] C.-M. Park, J. A. Bain, T. W. Clinton, P. A. A. van der Heijden, and T. J. Klemmer. Measurement of ga implantation profiles in the sidewall and bottom of focused-ion-beam-etched structures. *Applied Physics Letters*, 84(17):3331–3333, 2004.
- [22] I. D. Mayergoyz Lulian Nistor. Magneto-optic studies of garnets subject to rotating magnetic fields. *Journal of Applied Physics*, 97(10R302), 2005.
- [23] C. Kittel. On the theory of ferromagnetic resonance absorption. *Phys. Rev.*, 73(155), 1948.
- [24] M. R. Freeman, M. J. Brady, and J. Smyth. Extremely high frequency pulse magnetic resonance by picosecond magneto-optic sampling. *Appl. Phys. Lett.*, 60(20), 1992.
- [25] Joy Systems. Lig data sheet from joy systems. 1993.

- [26] T. Izuhara, M. Levy, and Jr R. M. Osgood. Direct wafer bonding and transfer of 10um-thick magnetic garnet lms onto semiconductor surfaces. *Applied Physics Letters*, 76(10):1261–1263, 2000.
- [27] M. Levy and Jr R. M. Osgood. Crystal ion slicing of single-crystal magnetic garnet films. *Journal of Applied Physics*, 83(11):6759–6761, 1998.
- [28] T. Izuhara, I. L. Gheorma, Jr R. M. Osgood, A. N. Roy, H. Bakhru, Yiheli M. Tesfu, and M. E. Reeves. Single-crystal barium titanate thin lms by ion slicing. *Applied Physics Letters*, 82(4):616–618, 2003.
- [29] F. J. Rachford, M. Levy, Jr R. M. Osgood, A. Kumar, and H. Bakhru. Magnetization and ferromagnetic resonance studies in implanted and crystal ion sliced bismuth-substituted yttrium iron garnet films. *Journal of Applied Physics*, 85(8):5217–5219, 1999.
- [30] R. M. Roth, D. Djukic, Y. Lee, Jr R. M. Osgood, P. A. Lewis, S. Bakhru, and H Bakhru. Fabrication and material properties of submicrometer sr<sub>2</sub>Fe<sub>14</sub>O<sub>19</sub> films exfoliated using crystal ion slicing. *Applied Physics Letters*, 90:112913, 2007.
- [31] Fu Yongqi, Ngoi Kok, and Ann Bryan. Investigation of 3d microfabrication characteristics by focused ion beam technology in silicon. *Journal of Materials Processing Technology*, 104:44–47, 2000.
- [32] C Tannous and J Gieraltowski. The stoner-wohlfarth model of ferromagnetism. *European Journal of Physics*, 29:475–487, 2008.
- [33] M J Sablik and D C Jiles. A modified stoner-wohlfarth computational model for hysteretic magnetic properties in a ferromagnetic composite rod under torsion. *Journal of Physics D: Applied Physics*, 32:1971–1983, 1999.

# Appendix A

## Appendix

### A.1 SEM Image Length Projections

Thickness measurements made by the FIB software are in the 2D x-y plane normal to the imaging direction, the z axis in Figure 2.11. To get a clear view of the cantilever edge we have to rotate it in two directions by some angle, usually  $45^\circ$ . To find the true thickness and length measurements the projections of the actual thickness onto this measurement plane must be found. This can be done using the general rotation matrices,

$$R_x(\theta) = \begin{bmatrix} 1 & 0 & 0 \\ 0 & \cos \theta & -\sin \theta \\ 0 & \sin \theta & \cos \theta \end{bmatrix} \quad (\text{A.1})$$

$$R_y(\theta) = \begin{bmatrix} \cos \theta & 0 & \sin \theta \\ 0 & 1 & 0 \\ -\sin \theta & 0 & \cos \theta \end{bmatrix} \quad (\text{A.2})$$

and a vector  $D$  of the cantilever thickness  $t$  in the  $\hat{z}$  direction when the sample top surface is normal to the beam or length  $l$  in the  $\hat{y}$  direction (Figure 2.11)

$$D(\theta) = \begin{bmatrix} 0 \\ 0 \\ t \end{bmatrix} \text{ or } D(\theta) = \begin{bmatrix} 0 \\ l \\ 0 \end{bmatrix} \quad (\text{A.3})$$

where the projected dimensions  $P$  in the x-y plane are given by  $P = R_x R_y D$ . The measured cantilever thickness (or length) at the given rotation is found from  $t' = \sqrt{P_x^2 + P_y^2}$ , where

$$P(\theta) = \begin{bmatrix} P_x \\ P_y \\ P_z \end{bmatrix} \quad (\text{A.4})$$

For the cantilever in Figure A.1 the projected cantilever length  $l'$  between thickness measurements is  $2.85 \mu\text{m}$ , and the change in thickness  $t'$  is  $0.23 \mu\text{m}$ . The measurements, with no tilt correction, were taken with the cantilever rotated by  $45^\circ$  in two directions. Care must be taken when using the rotation matrixes that the measurements are rotated in the correct order, which in this case is  $R_y$  with  $\theta = -45^\circ$  before  $R_x$  with  $\theta = +45^\circ$ . For the thickness,

$$P = R_x R_y D = P(\theta) = \begin{bmatrix} t \cdot \sqrt{2}/2 \\ -t \cdot 1/2 \\ t \cdot 1/2 \end{bmatrix} \quad (\text{A.5})$$

And so the length of this thickness vector in the x-y plane is

$$t' = 0.23 \mu\text{m} = \sqrt{P_x^2 + P_y^2} = \sqrt{(t \cdot \sqrt{2}/2)^2 + (-t \cdot 1/2)^2} = \frac{\sqrt{3}}{2} t \quad (\text{A.6})$$

Working backwards the corrected thickness of the cantilever is then  $t = 0.266\mu m$ .

Similarly for the length,

$$l' = \mu m = \sqrt{P_x^2 + P_y^2} = \sqrt{(0)^2 + (l \cdot \sqrt{2}/2)^2} = \frac{\sqrt{2}}{2}l \quad (\text{A.7})$$

the corrected length of the cantilever is  $l = 4.03\mu m$ . Using the true length and thickness of the cantilever we can estimate a correction in the back tilt to improve parallel milling of the cantilever. It must be remembered that redeposition can cause a slope to a milled area and mask the effect of an inaccurate back tilt, and so these measurements are best done after repeated thinning measurements at low probe currents. The angle  $\theta$  between the top and bottom cantilever surfaces is,

$$\theta = \arctan \left[ \frac{0.266\mu m}{4.03\mu m} \right] = 3.8^\circ \quad (\text{A.8})$$

This can be used to estimate how much to increase the back tilt. Because of the beam's gaussian profile changing the back tilt by a degree will not change the milled angle by a degree, so the exact angle to increase by cannot be determined. For this cantilever an increase of  $1.5^\circ$  was used for a total back tilt of  $2.7^\circ$  which gave a parallel cantilever after additional milling (Figure A.1(c))

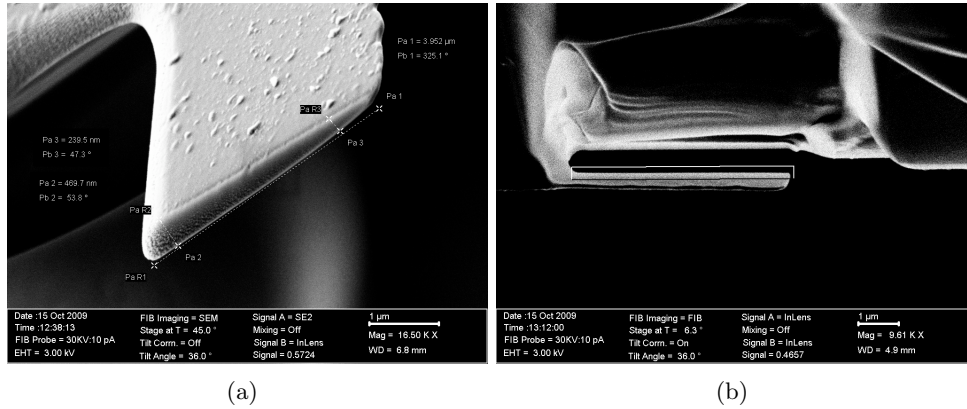


Figure A.1: A.1(a) shows a cantilever rotated at  $45^\circ$  in two axes with thickness change of  $t = 0.266\mu\text{m}$  and total length  $l = 3.95\mu\text{m}$ . A.1(b) shows the thinning process with a  $80\text{pA}$  probe, milling  $7\mu\text{m}$  depth. This is repeated several times, moving the milled box down slightly in the image each time to shave off layers from the cantilever.

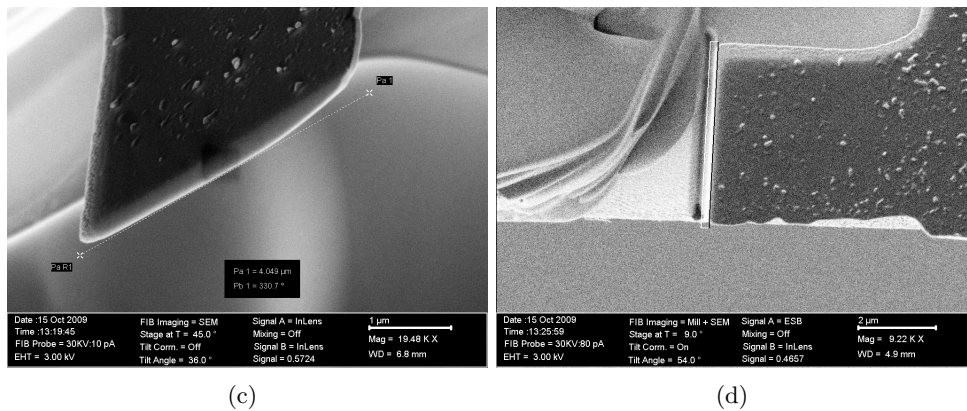


Figure A.1: A.1(c) shows the same cantilever after additional thinning. Rounding at the edges of the cantilever makes it hard to measure the thickness. A.1(d) is a FIB image from above showing trimming the cantilever edge to get an accurate profile.

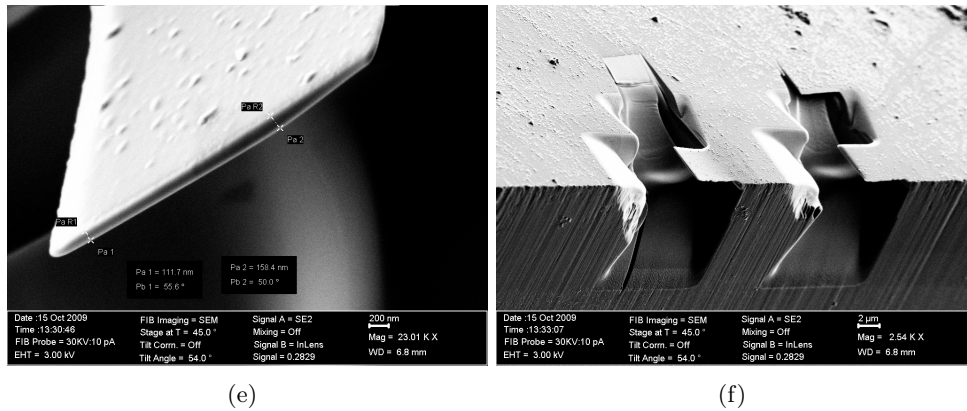


Figure A.1: A.1(e) The milled cantilever after proper thinning and trimming of the edge to  $\sim 150$  nm. This cantilever is on the left in A.1(f), which shows the cantilever beginning to flex.

## A.2 DAQ Connection Table

Moveable magnet system:

Stepper motor and controller power supply Part # 1792347ND <http://www.digikey.com/scripts/DkSearch/2347-ND> A linear power supply should be used.

Stepper motor and controller, CSK264-AT <http://catalog.orientalmotor.com/item/all-categories/ck2-series-stepping-motors/ck264-at?&plpver=11&origin=keyword&by=prod&filter=0>  
This contains both the motor (PK264-02A) and the driver (CSD2120-T)

Unislide rail, part number MB2527CJ-S2.5 This is a motorized rail, WITHOUT the motor. It contains internal limit switches and a 0.025" lead screw. It is made by <http://www.velmex.com/>

Multiplexer chip series #4051

Table A.1: USB 6221 Connection Diagram For Motor Control

DAQ Output or Input	Connected to:
D GND	Hall Probe Green
D GND	Translate Control Black
D GND	Rotate Control Black
D GND	AI 7 Ground
P0.0	Translate Control White
P0.1	Rotate Control White
P0.2	Rotate Control Red
PFI 10/P2.2	MUX 11
PFI 10/P2.4	AI 7 Positive
PFI 10/P2.4	MUX Ctr 0
+5V	Hall Probe Orange
+5V	MUX +5V
+5V	Translate Control Red
AO0	X Axis Piezo Amplifier Input
AO1	Y Axis Piezo Amplifier Input
AI0	Hall Probe Blue
AI1	Hall Probe Black
AI3	PreAmp 50 $\Omega$ Output
MUX output	Rotate Control Green
MUX output	Translate Control Green